

©2018

Manjari Bhamidipati

ALL RIGHTS RESERVED

SERS-BASED DETECTION AND QUANTIFICATION OF CANCER BIOMARKERS
IN CELLS AND TISSUE MICROARRAYS

By

MANJARI BHAMIDIPATI

A dissertation submitted to the

School of Graduate Studies

Rutgers, The State University of New Jersey

In partial fulfillment of the requirements

For the degree of

Doctor of Philosophy

Graduate Program in Biomedical Engineering

Written under the direction of

Laura Fabris

And approved by

New Brunswick, New Jersey

October 2018

ABSTRACT OF THE DISSERTATION
SERS-BASED DETECTION AND QUANTIFICATION OF CANCER BIOMARKERS
IN CELLS AND TISSUE MICROARRAYS

By MANJARI BHAMIDIPATI

Dissertation Director:

Laura Fabris

The need for early detection of cancer has resulted in the development of a number of molecular identification techniques that can screen for cancer biomarkers or cellular components indicative of a cancerous state. Biomarkers play a crucial role in cancer diagnosis and their identification and quantification can help monitor disease progression and therefore significantly contribute to clinical prognosis and to individualization and optimization of systemic therapy. Nanomaterial-based imaging systems provide the sensitivity, selectivity, and high multiplexing capability needed for molecular detection when leveraging the optical phenomenon of surface-enhanced Raman scattering (SERS). SERS is a vibrational spectroscopic technique that can be used to detect molecules present on or near the surface of plasmonic nanomaterials such as gold nanoparticles. The objective of this dissertation was to develop a SERS-based imaging tool for phenotype assessment of cancer cells and tissues by utilizing the optical properties of gold nanostars (i.e. gold nanoparticles (AuNPs) with a spherical core and sharp protruding spikes) together with the effective targeting ability of aptamers. It was hypothesized that gold

nanostars would be able to provide excellent SERS enhancement factors that would enable the quantification of biomarker expression at the single cell level. However, toxicity of the nanoparticles is a critical issue that needs to be taken into consideration before their implementation *in vitro*. For this purpose, detailed multi-parametric assessment of gold nanoparticle toxicity was carried out in cancerous (glioblastoma cells, U-87) and healthy cells (human fibroblasts) where the effects of nanoparticle shape, surface chemistry, and size on cell toxicity and cellular uptake were assessed. The study demonstrated that gold nanostars can be effectively taken up by both cell types without inducing significant toxicity when capped by a suitable ligand. They were therefore considered to be less toxic when compared to other nanoparticle shapes with the same surface coating and at the same dosage. Gold nanostars were then implemented in the development of a SERS based sensing platform for the recognition of soluble and cell-membrane embedded epithelial cell adhesion molecule (EpCAM) protein with high sensitivity and selectivity. EpCAM is a key epithelial biomarker that is overexpressed in several types of cancer and changes in its expression have been associated with the onset of metastasis. The developed biosensor enabled the detection and quantification of EpCAM at the single cell level in two cancer cells with varying expression levels, MCF-7 and PC-3. The highly sensitive cellular targeting with a detection limit of 10 pM was achieved by using EpCAM aptamers. The results demonstrated potential in using this approach for detecting cells that undergo phenotype variations during cancer metastasis. Finally, the gold nanostar aptamer-based SERS tags were implemented to distinguish between early and late stage prostate cancer based on the expression of the prostate-specific membrane antigen (PSMA) biomarker. The SERS tags enabled sensitive

detection of the PSMA biomarker in the prostate cancer cell LNCaP and in a tissue microarray containing samples from prostate cancer patients. Results showed elevated PSMA expression with progression of the disease and was found to outperform immunofluorescence. Overall, the dissertation established the importance of cancer diagnosis and staging based on biomarker expression and demonstrated the potential of SERS based diagnostic tools for molecular detection.

ACKNOWLEDGEMENTS

My graduate school experience has been really memorable and I would like to thank all the people who played a role. First, I would like to thank my advisor, Dr. Laura Fabris for providing me the opportunity to pursue this work under her guidance. She has been a tremendous support during these five years and I would like to thank her for all her support, guidance and constant encouragement.

I would like to thank my committee members, Dr. Prabhas Moghe, Dr. Mark Pierce and my external advisor, Dr. Isaac Kim for their guidance and feedback throughout these years. I would also like to thank Dr. Moghe and Dr. Kim for giving me access to their cell culture facility and resources. I'm particularly grateful to the lab manager at the Cancer Institute of New Jersey, Dr. Geuntaek Lee for giving me timely access to cells and TMAs and for his guidance on my experiments.

Thank you to all my lab members, especially Riyanka Pai, Kholud Dardir, Ted Tsoulos, Matina Kallontzi, Supriya Atta, and Sakshi Sardar for all their help, suggestions, exchange of ideas and all the fun times in the lab. I would also like to thank my friends in BME for making my experience at Rutgers enjoyable. I would also like to extend my gratitude to the BME department and staff members, especially Lawrence Stromberg.

My family has been my biggest strength throughout my graduate school and I would like to thank them for their love, patience, and support during this journey.

DEDICATION

This dissertation is dedicated to my family.

TABLE OF CONTENTS

ABSTRACT	ii
ACKNOWLEDGEMENTS	v
DEDICATION	vi
TABLE OF CONTENTS	vii
LIST OF FIGURES	xi
LIST OF TABLES	xvii
LIST OF SCHEMES	xviii
CHAPTER 1 INTRODUCTION	1
1.1 Background	2
1.2 Surface Enhanced Raman Spectroscopy (SERS).....	4
1.3 SERS Tags.....	5
1.4 Nanoparticles.....	6
1.5 Raman Reporter.....	7
1.6 Surface Coating	7
1.7 Targeting Molecules.....	8
1.8 Applications of SERS in Cancer Biomarker Detection	9
1.9 Application of SERS in Tissue Imaging	11
1.10 Dissertation Hypothesis and Overview	13
1.11 References	16
CHAPTER 2 MULTIPARAMETRIC ASSESSMENT OF GOLD NANOPARTICLE CYTOTOXICITY IN CANCEROUS AND HEALTHY CELLS: THE ROLE OF SIZE, SHAPE AND SURFACE CHEMISTRY	19
2.1 Abstract	20
2.2 Introduction	21
2.3 Experimental Section	24
2.3.1 Synthesis of AuNPs	24
2.3.2 Surface Functionalization of AuNPs	25
2.3.3 Characterization of AuNPs	26

2.3.4	Estimation of Ligand Concentrations on AuNPs.....	27
2.3.5	Cell Culture Maintenance	28
2.3.6	<i>In vitro</i> Cell Toxicity Studies.....	28
2.3.7	Cellular Uptake Studies	30
2.3.8	Statistical Analyses	31
2.4	Results and Discussion.....	31
2.4.1	Synthesis and Characterization of Functionalized AuNPs	31
2.4.2	Estimation of Ligand Concentrations on AuNPs.....	37
2.4.3	<i>In vitro</i> toxicity study.....	40
2.4.4	Cellular uptake of AuNPs	47
2.5	Conclusion.....	53
2.6	Acknowledgments.....	55
2.7	References	56
CHAPTER 3 SERS-BASED QUANTIFICATION OF BIOMARKER EXPRESSION AT THE SINGLE CELL LEVEL ENABLED BY GOLD NANOSTARS AND TRUNCATED APTAMERS		58
3.1	Abstract	59
3.2	Introduction	60
3.3	Experimental Methods	64
3.3.1	Nanoparticle Synthesis.....	64
3.3.2	Preparation of SERS tags.....	64
3.3.3	Substrate Preparation	65
3.3.4	Surface Functionalization	65
3.3.5	Characterization of NPs and SERS tags	66
3.3.6	Substrate Characterization	66
3.3.7	Cell Culture.....	67
3.3.8	Flow Cytometry	67
3.4	Results and Discussion.....	68
3.4.1	NP and SERS tags synthesis.....	68
3.4.2	Substrate Preparation	73

3.4.3	AFM measurements	74
3.5	SERS measurements	77
3.6	Conclusion.....	87
3.7	References	89
CHAPTER 4 SERS-BASED QUANTIFICATION OF PSMA IN TISSUE MICROARRAYS ALLOWS EFFECTIVE STRATIFICATION OF PATIENTS WITH PROSTATE CANCER.....		91
4.1	Abstract	92
4.2	Introduction	93
4.3	Materials and Methods	97
4.3.1	Nanoparticle Synthesis.....	97
4.3.2	Preparation of SERS tags.....	97
4.3.3	Characterization of NPs and SERS tags	98
4.3.4	SERS Measurements.....	98
4.3.5	Substrate Preparation for Protein Functionalization	99
4.3.6	Cell Culture.....	99
4.3.7	Semi-Quantitative RT-PCR	100
4.3.8	Western Blot Analysis	101
4.3.9	Tissue Microarray Staining.....	101
4.4	Results and Discussion.....	102
4.4.1	Preparation of SERS Tags	102
4.4.2	Correlating SERS Intensity with Protein Concentration	107
4.4.3	Expression of PSMA in Prostate Cancer Cells.....	108
4.4.4	SERS Analysis of Cells	113
4.4.5	Analysis of PSMA expression in Prostate TMA	114
4.5	Conclusion.....	117
4.6	References	119
CHAPTER 5 CONCLUSION AND FUTURE DIRECTION.....		121
5.1	Conclusion.....	121
5.2	Future Directions.....	121

5.3 References 124

LIST OF FIGURES

- Figure 1.1** Illustration of the oscillations of surface plasmons in a spherical nanoparticle. Figure reproduced with permission.²⁴ 5
- Figure 2.1** UV-Vis absorption spectra (normalized) of as synthesized gold nanospheres (LSPR: 521 nm), gold nanorods (LSPR: 517 nm, 645 nm) and gold nanostars (LSPR: 774 nm). 32
- Figure 2.2** Representative transmission electron microscopy (TEM) images of CTAB coated (A) nanospheres (B) nanorods and (C) nanostars. Scale bar = 50 nm for nanospheres and 100 nm for nanorods and nanostars..... 33
- Figure 2.3** Characterization of the functionalized AuNPs. Panels (A) to (C) show the UV-vis spectra of CTAB-, PEG-, and HSA-coated nanospheres, nanostars, and nanorods respectively. 34
- Figure 2.4** Plots A and B show dynamic light scattering (DLS) data that give the size distributions of CTAB, PEG, and HSA coated spheres and stars in Milli-Q water at room temperature. 36
- Figure 2.5** Figure shows ¹H NMR spectra of CTAB coated AuNPs. Panels show the spectra corresponding to A) CTAB nanospheres, B) CTAB nanorods, C) CTAB nanostars and D) a CTAB stock solution. ¹H NMR chemical shifts are reported in ppm downfield from tetramethylsilane and were referenced to deuterated water solvent. 38
- Figure 2.6** Figure shows TGA of PEG coated AuNPs. Panel A shows the weight loss profile of PEG coated nanospheres, nanorods and nanostars. Panel B shows the weight loss observed in as-received PEG between 35° C and 800° C..... 39
- Figure 2.7** Cell viability results via MTT proliferation assay results have been shown here. Panels A and B show results after exposure to PEG nanostars at various concentrations after 4 hours and 24 hours in U87 cells and fibroblasts respectively. Statistically significant difference * = from the previous lower concentration at that time point (p < 0.05). Panels C and D show the cell viability results after exposure to CTAB, PEG and HSA at different concentrations in U87 cells and fibroblasts respectively. Legends represent concentrations of CTAB, PEG and HSA observed in 100 µg/mL of 1: nanospheres, 2: nanorods and 3: nanostars. Viability values in all panels have been normalized to control (without nanoparticles). Error bars represent standard deviation with n = 3. Statistically significant difference * = from nanospheres within the same surface coating at that time point (p < 0.05). 41
- Figure 2.8** Viability data from the MTT cell proliferation assay after exposure to different AuNPs have been shown here. Plots show relative cell viabilities observed in A) U87 cells after 4 hours, B) U87 cells after 24 hours, C) fibroblasts after 4 hours and D)

fibroblasts after 24 hours when exposed to different AuNPs. Percentage of viability was determined with respect to control. Error bars represent standard deviation with $n = 3$. Statistically significant difference * = from nanospheres within the same surface coating at that time point ($p < 0.05$), and ! = from nanorods within the same surface coating at that time point ($p < 0.05$). 43

Figure 2.9 MTT assay data without normalization against controls show effective cell viability at 4 and 24 hours for U87 cells (A) and human dermal fibroblasts (B). Also reported are the viabilities at 4 and 24 hours for the control U87 cells and fibroblasts. This figure has been included in support of Figure 2.8, to explain the apparent higher cell viability at 24 than 4 hours of incubation. In reality, by observing the viability of the control cells at 24 hours, especially for fibroblasts, one can determine that the control cells have low viabilities leading to the difference between sample and controls to be higher, leading to an apparent viability increase over time. In reality, the actual values are slightly lower at 24 hours when compared to 4 hours. Error bars represent standard deviation with $n = 3$. Statistically significant difference * = from nanospheres within the same surface coating at that time point ($p < 0.05$), and ! = from nanorods within the same surface coating at that time point ($p < 0.05$). 43

Figure 2.10 Cytotoxicity data from LDH (lactate dehydrogenate) assay have been shown here. Panels A and B show the toxicity observed after exposure to AuNPs for 4 and 24 hours in U87 cells and fibroblasts respectively. Control group represents untreated cells. Error bars represent standard deviation with $n = 3$. Statistically significant difference * = from nanospheres within the same surface coating at that time point ($p < 0.05$), and ! = from nanorods within the same surface coating at that time point ($p < 0.05$). 45

Figure 2.11 ROS production and caspase 3/7 activity observed in cells. Panels A and B show ROS production in U87 cells and fibroblasts respectively. Panels C and D show the caspase 3/7 activity seen in U87 and fibroblasts after exposure to different NP. Control represents untreated cells. Error bars represent standard deviation with $n=3$. Statistically significant difference * = from nanospheres within the same surface coating at that time point ($p < 0.05$), and ! = from nanorods within the same surface coating at that time point ($p < 0.05$). 46

Figure 2.12 Transmission electron micrographs aid in the localization of nanoparticles inside cells. In both U87 cells (top) and fibroblasts (bottom), the NPs were primarily found inside membrane-bound vesicles, suggesting an uptake mechanism mediated by endocytosis..... 49

Figure 2.13 Figures show damage observed in U87 cells after exposure to HSA nanostars. Panels show A) formation of apoptotic bodies and damage to cell membrane, B) and C) presence of large number of vacuoles indicating autophagy of cell organelles

and, D) condensation of chromatin at the periphery of the nucleus. All these changes in the U87 cells indicate possible death via apoptosis. Scale bars in all panels are 500 nm. 50

Figure 2.14 Figures show damage observed in fibroblasts after exposure to PEG and HSA nanostars. Panels show A) damage to cell membrane, B), C) and D) show mitochondrial damage and changes to the cell membrane. All these changes in fibroblasts indicate possible death via necrosis. Scale bars in all panels are 500 nm. 51

Figure 2.15 AuNP uptake (ng of gold per cell) measured using ICP-MS. Figure panels show uptake after A) 4 hours in U87 cells, B) 24 hours in U87 cells, C) 4 hours in fibroblasts, and D) 24 hours in fibroblasts. Error bars represent standard deviation, with n=3. 52

Figure 2.16 Relationship between cell viability and AuNP uptake. Cell viabilities have been measured with respect to the controls. Figure panels show viabilities seen in A) U87 cells, and B) fibroblasts. Error bars represent standard deviation with n=3 samples. 53

Figure 3.1 Assessment of nanostar properties and functionalization was carried out with multiple techniques. Figures 3.1 (A) and 1 (B) show transmission electron (TEM) micrographs of (A) as synthesized gold nanostars, and (B) nanostars functionalized with 4-aminothiophenol and EpCAM aptamer. Scale bars are 100 nm. Figure 3.1(C) shows the UV-visible spectra of as-synthesized gold nanostars, 4-ATP-coated nanostars, and 4-ATP- and EpCAM aptamer-coated nanostars. Figure 3.1(D) shows the relative dynamic light scattering (DLS) data, which provide size distributions in Milli-Q water at room temperature of as-synthesized nanostars, nanostars functionalized with 4-ATP, and with 4-ATP and EpCAM aptamer. 69

Figure 3.2 SERS spectra of 4-ATP coated nanostars and 4-ATP and EpCAM aptamer coated nanostars. Despite introduction of additional peak after functionalization with the thiolated aptamer, the peak at 1076 cm^{-1} is still dominant. 72

Figure 3.3 Scanning electron micrographs (SEM) of the substrate show uniform distribution of gold nanostars on its surface (A), with retained nanoparticle morphology (B). Slight reshaping is often induced by the electron beam. Scale bars are $1\text{ }\mu\text{m}$ in (A) and 200 nm in (B). 74

Figure 3.4 Topography and height profiles of the substrate at various functionalization steps collected via atomic force microscopy (AFM). (a) Substrate with nanostars only (h=126 nm), (b) substrate with nanostars functionalized with EpCAM aptamer (h=134 nm), (c) substrate with EpCAM-functionalized nanostars after addition of 6-mercaptophexanol (MCH) (h=168 nm), (d) substrate with EpCAM- and MCH-functionalized nanostars after addition of EpCAM protein (h=182 nm), and (e) after addition of SERS tags (h=208 nm). A clear increase in the height profile can be observed at each stage. Between steps C and D there is no net height increase, as a consequence of

aptamer folding from its extended conformation in the self assembled monolayer after recognition of the target protein..... 76

Figure 3.5 SERS spectra collected on the substrates after exposure to increasing concentrations of EpCAM. Figures 5(A) and 5(C) show the SERS spectra for protein capture carried out with the 48-bp and the 17-bp EpCAM aptamers, respectively. Figures 3.5(B) and 3.5(D) shows the intensity variation of the 1076 cm^{-1} peak with respect to the EpCAM protein concentration ($\log(\text{nM})$), for the 48-bp and 17-bp aptamer respectively. Inset figures show the linear dynamic range regime. 78

Figure 3.6 Assessment of assay selectivity. SERS spectra collected in the presence of 500 nM EpCAM and two control proteins, BSA and fibrinogen, in addition to the control without protein. The peak at ca. 1400 cm^{-1} is due to the interference of the glass substrate. 79

Figure 3.7 Different stem loop conformations at 25°C for A) the 48-bp and B) the truncated 17-bp EpCAM DNA aptamer. A significantly higher number of almost degenerate conformations can be observed for the longer aptamer, compared to its truncated counterpart. The secondary structures of the aptamer were generated using the OligoAnalyzer 3.1 software from Integrated DNA Technologies, Inc..... 80

Figure 3.8 SERS spectra of FITC taken using 633 nm and 785 nm laser excitation..... 81

Figure 3.9 Flow cytometry results showing that MCF-7 and PC-3 cells are EpCAM positive cells while HeLa are EpCAM negative cells. 83

Figure 3.10 Cell capture efficiency (%) of the cancer cells, MCF-7 and PC-3, on the SERS substrates. 84

Figure 3.11 Quantification of MCF-7 (A, B) and PC3 (C, D) cells using the described assay. By monitoring the intensity of the 1076 cm^{-1} peak (A), it can be observed how the SERS response linearly increases with increasing number of MCF-7 cells between the wavenumbers 500 and 2000 cm^{-1} (B). Similarly, dependence between the intensity of the 1076 cm^{-1} peak and the number of MCF-7 cells is also linear (C and D)..... 85

Figure 3.12 Assessment of assay selectivity on cells with different membrane expression of EpCAM (MCF-7 and PC3) or with no expressed EpCAM. A control spectrum without cells is also shown..... 86

Figure 3.13 Quantification of EpCAM density in individual cells. Figure 3.11(A) shows the linear correlation ($R^2 = 0.99677$) between \log of the number of EpCAM molecules found per μm^2 area at different protein concentrations and their SERS response at 1076 cm^{-1} . Using this equation, the number of EpCAM molecules present per μm^2 area on MCF-7 and PC-3 cells was calculated and shown in Figure 3.11(B). Higher expression levels are observed in MCF-7 cells, as expected. 87

Figure 4.1 Characterization of the synthesized SERS tags was carried out via multiple techniques. Figures 4.1(A) and (B) show the transmission electron (TEM) micrographs of (A) as synthesized nanostars, and (B) nanostars functionalized with 4-ATP and PSMA aptamer. Figure 4.1(C) shows the UV-Vis spectra of nanostars before and after functionalization. Figure 4.1(D) shows the dynamic light scattering (DLS) data, that shows the size distribution of the nanoparticles. Figure 4.1(E) shows the zeta potential (mV) values of the functionalized nanostars with 4-ATP and PSMA aptamer. Results are shown as mean \pm standard deviation with n = 3 readings for each sample. Figure 4.1(F) shows the SERS spectra of 4-ATP coated nanostars and nanostars coated with 4-ATP and PSMA aptamer.....	106
Figure 4.2 SERS signal dependence on concentration of soluble PSMA protein. Figure 4.2(A) shows the SERS peaks observed between 700 and 1800 cm^{-1} for protein concentrations between 100 pM and 100 nM. A sample lacking the protein was used as a control. Figure 4.2(B) shows the intensity variation of the peak 1438 cm^{-1} with respect to log of the PSMA protein concentration in nM.....	108
Figure 4.3 Figure shows SERS peaks that result from the addition of PSMA aptamer and soluble PSMA protein.....	108
Figure 4.4 Figure shows the confirmation of the expression of PSMA in LNCaP cells. Figure 4.4(A) shows the RT-PCR results observed in the prostate cancer cells, LNCaP and PC3 while Figure 4.4(B) shows the Western Blot analysis of LNCaP and PC3 cells. Both experiments confirm the expression of PSMA in LNCaP cells while PC3 cells show no expression of PSMA. β -actin was used as a loading control in both experiments. ...	109
Figure 4.5 Fluorescent staining of LNCaP cells with PSMA antibody and PSMA aptamer that were conjugated to the fluorophore Alexa Fluor 488. Cell nuclei were stained with DAPI. Control represents cells that weren't stained with both PSMA aptamer and antibody. Scale bars represent 30 μm	111
Figure 4.6 Figure shows the fluorescent staining of PC3 cells with PSMA antibody and PSMA aptamer that were conjugated to the fluorophore, Alexa Fluor 488. Cell nuclei were stained with DAPI. Control represents cells that weren't stained with both PSMA aptamer and antibody. Scale bars represent 50 μm	112
Figure 4.7 Cell viability results via MTT proliferation assay show the relative cell viability observed in LNCaP cells after exposure to different concentrations of gold nanostars functionalized with 4-ATP and PSMA aptamer for 24 hours. Viability results have been normalized to the control (without nanoparticles). Error bars represent standard deviation with n = 3.	113
Figure 4.8 SERS spectra seen in LNCaP cells incubated with nanostars functionalized with 4-ATP and PSMA aptamer. Figure 4.6(A) shows the variation in SERS intensity	

seen at the single cell level in five different LNCaP cells. Further assessment of assay selectivity was carried out by incubating PC3 cells that have no surface expression of PSMA. Results from this are shown in Figure 4.6(B). 114

Figure 4.9 Representative immunofluorescence staining results of a prostate tissue microarray stained with a primary PSMA antibody and a secondary antibody conjugated with TRITC. Cell nuclei have been stained with DAPI. Fluorescence intensity (background subtracted) obtained from immunofluorescence staining of the prostate TMA. The prostate tissue sections have a pathological status ranging from Grade Groups 1-5 and show increasing PSMA expression in going from Group 1 to Group 2, while no clear differentiation was possible between Group 2 and Group 3. Scale bars represent 200 μm 115

Figure 4.10 SERS spectra of the prostate tissue microarrays that were incubated with SERS tags. a) SERS intensity of the 1438 cm^{-1} peak of the spectra obtained from the prostate TMA at different disease stages compounded in groups 1, 2, and 3 depending on recommended therapy. SERS data points become substantially more spread with increasing disease severity, consistent with tissue heterogeneity. B) Averaged SERS spectra for the three groups show clear increase in the intensity of the 1483 cm^{-1} peak between groups 2 and 3, consistent with higher PSMA expression in advanced stage disease. 117

LIST OF TABLES

Table 2.1 Zeta potential values (mV) of AuNPs in water observed after synthesis and functionalization with different surface coatings. Results shown as mean \pm standard deviation with $n = 3$ readings for each sample.	37
Table 3.1 Zeta potential values (mV) of gold nanostars observed after functionalization with 4-ATP and EpCAM aptamer. Results are shown as mean \pm standard deviation with $n = 3$ readings for each sample.	71
Table 3.2 SERS peak assignments for 4-aminothiophenol between 500 and 2000 cm^{-1} . The symbols δ , ν , and π correspond to bending, stretching, and wagging modes, respectively.	72
Table 4.1 Explanation of the Gleason scoring system. Score 1 and Score 2 are assigned based on histopathology. Higher values for Score 1 than Score 2 indicate higher disease severity.	95
Table 4.2 Table shows the capture efficiency of PSMA RNA aptamer on the nanoparticles detected using the Quant-iT™ OliGreen® ssDNA kit. Two different concentrations of gold nanostars (1.5 nM and 3 nM) were functionalized with varying ratios of the Raman reporter, 4ATP and PSMA aptamer. Results are shown as mean \pm standard deviation with $n = 3$ readings for each sample.	104

LIST OF SCHEMES

Scheme 3.1 Schematic representation of the sequence of steps followed to carry out the assay. Glass substrates, gold nanostars, EpCAM aptamer, mercaptohexanol, EpCAM protein, and 4-aminothiophenol not drawn to scale..... 63

CHAPTER 1 INTRODUCTION

Note: Portions of this chapter have been reprinted (adapted) with permission from **Manjari Bhamidipati** and Laura Fabris. “Multiparametric Assessment of Gold Nanoparticle Cytotoxicity in Cancerous and Healthy Cells: The Role of Size, Shape, and Surface Chemistry”. *Bioconjugate Chemistry*, 28(2), 449–460, 2017. Copyright (2017) American Chemical Society.

1.1 Background

Cancer is one of the leading causes of death worldwide; among the total number of cancer-related deaths, 90% are due to metastasis. The American Cancer Society estimates that in year 2018, the number of new cancer cases will reach 1,735,350, with 609,640 cancer related deaths in the United States alone.¹ The survival rates of patients with metastatic cancer are usually low because of late diagnosis and possibly limited access to timely and standardized treatment options. Studies have shown that early detection is highly crucial for clinical diagnosis and successful treatment of the disease.

Cancer biomarkers comprise a wide range of biochemical entities. They can consist of proteins, DNA, mRNA, enzymes, metabolites, and even cell surface receptors. They can be present in biological fluids such as blood and serum as well as in tumor tissues.² They are defined as a substance that can be measured in a patient which would allow us to distinguish between a normal biological response and a diseased state.³ Biomarker research would allow diagnosis and classification of the tumor, and be useful in monitoring treatment response, toxicity, and recurrence of the disease.⁴

There are several biological challenges involved in the detection of cancer biomarkers. The complexity of the disease makes it challenging to identify a single biomarker able to detect with sensitivity and high specificity all cancers of a specific organ. So far there are no biomarkers that meet the diagnostic and prognostic requirements of a cancer screening tool. There is therefore a need to establish the clinical relevance and applicability of new biomarkers and integrate them into clinical practices. In addition, techniques for biomarker detection tend to have high sensitivity but low specificity, leading to a higher

incidence of false-positive results, which may translate into unnecessary diagnostic tests for patients and overtreatment. Longitudinal and cross-sectional studies on a panel of cancer biomarkers would therefore help avoid false positives in cancer diagnosis.⁴ Lately, techniques are being implemented to analyze biomarkers from a variety of biological fluids (i.e. liquid biopsy), including molecules present in blood, serum, or urine, that reflect the presence of a tumor in the body. These biomarkers include screening for circulating tumor cells (CTCs) and other macromolecules such as mRNA, DNA, and proteins originating from the tumor cells in circulation. Studies indicate that identification and quantification of these tumor markers can help monitor disease progression and therefore contribute to clinical prognosis.⁵ Current techniques focus on detection based on tumor cell morphology and their immune and cell-surface properties.⁶⁻⁷ However, there is a broad morphological heterogeneity observed among CTCs derived from the same tissue, in part as an effect of the epithelial-to-mesenchymal transition. Thus, a CTC population may comprise cells expressing several surface markers with self-renewal and tumor initiating capabilities. Therefore, techniques relying on the identification on CTCs of epithelial markers alone may prove to be insufficient in disease prognosis.⁷

Several promising detection methods for the identification of cell surface and intracellular biomarkers have been developed. These include enzyme-linked immunosorbent assays (ELISA),⁸ surface plasmon resonance (SPR),⁹ electrochemical assays,¹⁰ colorimetric assays,¹¹ and fluorescence methods.¹² Optical detection techniques have remained the most commonly used methods; among them fluorescence detection is the most prevalent. While these techniques are highly efficient and provide good sensitivity, there are still challenges that need to be addressed.^{4, 13} Fluorescence detection

suffers from the disadvantages of quenching, photobleaching, and tissue autofluorescence. In addition to this, a large spectral overlap is observed in fluorescent molecules making it difficult to interpret multiple targets simultaneously, i.e. carry out multiplexing.¹⁴ As a result, the use of multi-functional nanomaterial-based systems for cancer detection and targeted therapy has significantly increased over the past decade.¹⁵ Since early diagnosis of cancer improves survival rates, recently there has been a lot of interest in developing detection techniques that screen for molecular and cellular biomarkers that are indicative of a cancer state.¹⁶ Gold nanoparticles (AuNPs) in particular have been preferred over other nanomaterials due to their stability and biocompatibility.¹⁷⁻¹⁸

1.2 Surface Enhanced Raman Spectroscopy (SERS)

Surface enhanced Raman spectroscopy (SERS) is a vibrational spectroscopic technique where extremely intense Raman signals can be achieved when a Raman molecule is placed in close proximity to the surface of a nanostructured noble metal.¹⁹ Raman spectroscopy is based on the inelastic scattering of monochromatic light originating from a laser source. This technique is helpful in obtaining useful information related to the vibrational energy of the molecules being monitored.²⁰ However, the efficiency of Raman scattering is very low. Raman molecules exhibit cross sections of the order of $10^{-29} \text{ cm}^2 \text{ molecule}^{-1} \text{ sr}^{-1}$ while in comparison a fluorescent cross-section is of the order of $10^{-16} \text{ cm}^2 \text{ molecule}^{-1} \text{ sr}^{-1}$.²¹ This limitation can be overcome by taking advantage of the SERS effect.

The signal enhancements observed in SERS are made possible by the use of plasmonic nanoparticles like gold nanoparticles (AuNPs) as signal enhancing substrates. When AuNPs interact with the electromagnetic radiation of a laser source, the conduction electrons begin to oscillate coherently. The collective oscillation of the electrons, known as surface plasmon, takes place at the interface between the metal surface and the surrounding dielectric medium, and when in resonance with an incoming radiation, displaces the electron cloud from its equilibrium position. This equilibrium position is then reinstated by coulombic restoring forces which form an oscillating dipole that resonates at a specific frequency called localized surface plasmon resonance (LSPR). The surface plasmon resonance is dependent on the size and shape of the AuNPs along with the local dielectric properties and this phenomenon (shown in Figure 1.1) forms the basis of SERS.²²⁻²³

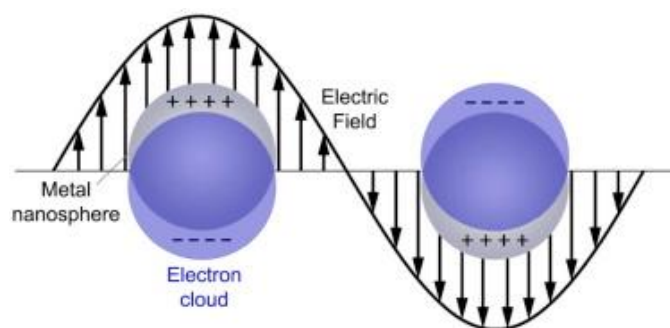


Figure 1.1 Illustration of the oscillations of surface plasmons in a spherical nanoparticle. Figure reproduced with permission.²⁴

1.3 SERS Tags

SERS tags are AuNP-based labeling systems that can indirectly identify and localize selected targets, thereby demonstrating optical labeling similar to fluorescent dyes in fluorescence microscopy. SERS tags are composed of a gold nanoparticle core which

provides near field enhancements necessary for SERS, Raman reporter molecules for labeling, a passivating coating layer to ensure stability and biocompatibility, and targeting moieties to enable selective targeting of the biological target (e.g. proteins, cells, etc.). The highly specific recognition enabled by SERS tags is provided via the use of aptamers or antibodies.

1.4 Nanoparticles

AuNPs of different morphologies such as nanospheres, nanorods, and nanostars can be synthesized and functionalized with various targeting ligands, therapeutic drugs, and imaging labels.²⁵ The surface plasmon resonance varies based on the morphology and size of the particles. It ranges from 520-550 nm for nanospheres; it exhibits two resonance peaks for nanorods, one at 520-550 nm (corresponding to the transverse axis of rods) and one at $\lambda > 630$ nm, whose position depends on the aspect ratio of the rods, and is defined as the longitudinal mode; it is broad and located in the near infrared (NIR) region for nanostars. In the NIR range, water, blood, and biological tissues are semi-transparent to the electromagnetic radiation thus rendering rods and stars more suitable for use in biological applications.²⁶

In SERS-based experiments, the presence of a probe molecule near the plasmonic nanoparticle enhances its Raman signal by at least 5-6 orders of magnitude, with values up to 10^{10} at the *hot spots*.²⁷ These *hot spots* are generally found at the edges and vertices of isolated NPs that have sharp features like nanostars. Gold nanostars are excellent sensing platforms that can produce SERS enhancement factors of 10^9 ,²⁸ a value that is only two orders of magnitude lower than that necessary for single molecule detection,

due to the presence of multiple sharp tips that can generate multiple hot spots. Hot spots can also be found at the junction between electromagnetically coupled NPs like dimers of nanospheres with inter-particle gaps of 1-2 nm.²⁹

1.5 Raman Reporter

Raman reporter molecules are Raman active molecules with intrinsically high cross-sections that play an important role in the development of a SERS tag. Each Raman molecule possesses a unique and narrow spectral fingerprint, which allows multiple tags to simultaneously detect several target molecules. Selection of the appropriate Raman reporter for an application is dependent on several factors. Typically, molecules with large Raman scattering cross sections are chosen since they help produce strong SERS signals. It is also necessary for the reporters to have a strong affinity with the metallic colloid in order to provide stability to it and prevent desorption when being functionalized further. Hence, the most commonly used reporters for gold and silver nanoparticles include sulfur- and nitrogen- containing molecules. In addition to these factors, it is necessary to choose molecules that have simple spectra characterized by few peaks so as to reduce peak overlap; limited peak overlap enables the implementation of multiplexed assays for the detection of target molecules.³⁰

1.6 Surface Coating

Surface coating of SERS tags for biological applications is fundamental in ensuring biocompatibility and stability of the tags. Tags that are not coated often encounter adverse effects under physiological conditions like opsonization and aggregation.³¹ In addition, the surfactants used for particle synthesis often induce toxicity. Several

methodologies have been developed to surface coat materials that will help overcome these challenges. They are usually coated with a biomolecule, polymers, liposomal coating, or glasses such as silica. The most commonly used biomolecule is bovine serum albumin (BSA). It can be easily adsorbed onto the surface of a nanoparticle via weak interactions with the metal surface and forms a protective shell.³²⁻³³ However, such molecules do not always resist enzymatic cleavage when introduced in a host organism and lose their activity in a short time.³¹ Among polymeric coatings, polyethylene glycol (PEG) is considered an ideal polymer as it ensures biocompatibility and excellent biodistribution *in vivo*.³⁴ The use of PEG allows modification with different chemical end groups which enable it to bind strongly to targeting moieties on the SERS tag. Liposomes are a new class of coatings for nanoparticles. They are being used for applications since they provide stability to the tags and enable targeting moieties like antibodies to be attached to them directly.³⁵ Another method for the functionalization of SERS tags is by silica coating them. It provides the advantages of having low nonspecific binding, high stability, and finely tunable control over the shell thickness.³⁶

1.7 Targeting Molecules

Targeting molecules such as antibodies, aptamers, or small molecule ligands allow the SERS tags to specifically recognize and bind the target of interest. It is necessary to link them covalently to the tags to avoid dissociation when suspended in solution. The targeting molecules are typically attached to the coating layer on NPs by taking advantage of synthetically added or already present pendant groups. For instance, stable covalent bonds can be formed by using sulfhydryl containing groups to bind to metallic

NPs surface; stable amide bonds can be formed with amine groups using the linker molecule N-succinimide; and biotin-modified tags can be linked to streptavidin-tagged nanoparticles. Along with these, reagents such as 1-ethyl-3-(3-dimethylaminopropyl) carbodiimide (EDC) and N-hydroxysuccinimide (NHS) can be used to react the carboxylic acid groups of the antibodies with reactive moieties available on molecules to form an amide bond.³¹

Antibodies have found a wide range of applications in the detection of biomarkers; however, they suffer from the limitations of being expensive and sensitive to manipulation.³⁷ To overcome these issues, a new class of targeting molecules known as aptamers has demonstrated potential as an alternative identification tool. They are easy to synthesize and have the ability to target a wide range of molecules with high affinity and specificity.³⁸⁻³⁹ Aptamers are single-stranded DNA or RNA molecules with small molecular weight between 8 to 15 kDa. They are extremely stable and have negligible toxicity and immunogenicity. They are synthesized using a method called Systematic Evolution of Ligands by Exponential Enrichment (SELEX)³⁸ and can be developed to target molecules ranging from small compounds to large cell membrane and transmembrane proteins.

1.8 Applications of SERS in Cancer Biomarker Detection

One of the fundamental applications of SERS tags has been in the multiplexed detection of cell-surface cancer biomarkers, which has enabled screening of cancer cells.⁴⁰ Circulating tumor cells present in the blood stream or the lymphatic system play a crucial role in the onset and evolution of metastasis, by forming secondary tumors at a distant

site.⁴¹ Studies have shown that identification and quantification of biomarkers present on these cells can help monitor disease progression and therefore significantly contribute to clinical prognosis and to individualization and optimization of systemic therapy.

SERS tags have been used successfully to identify and isolate cancer cells in biological samples based on the expression of biomarkers in *in vivo* imaging and *ex vivo* diagnostic sensors.⁴² In *ex vivo* applications, they have been shown to directly bind and separate cancer cells from blood samples or isolate the cells using functionalized substrates. For instance, Zhang *et al.*⁴³ used 60 nm gold nanospheres functionalized with a Raman molecule (pMBA) and anti-EpCAM antibody with specificity against non-small-cell lung cancer cells. They spiked 1 mL of whole human blood with 100 cancer cells among which they were able to capture 34 cells on a nitrocellulose membrane based on the detection of EpCAM. Nima *et al.*⁴⁴ used silver coated-gold nanorods for the multiplexed identification of circulating tumor cells originating from breast cancer. They used four different Raman reporter molecules that were targeted four biomarkers: Keratin 18, Insulin-like growth factor antigen (IGF-1), CD44, and EpCAM that are specific to breast cancer cells. They observed that by coating gold nanorods with silver, a two-fold SERS signal enhancement could be seen. In addition to that, they were able to detect and isolate MCF-7 cells with high specificity in whole human blood. Wang *et al.* were able to detect cancer cells in the presence of white blood cells using nanoparticles. They targeted the biomarker, epidermal growth factor (EGF), which plays a key role in squamous cell carcinoma of the head and neck. Using these SERS tags, they were able to target and isolate 1-720 tumor cells per milliliter of whole blood from 19 patients.⁵ Ahirwar *et al.*⁴⁵ showed that aptamers together with nanospheres can detect and quantify estrogen

receptor alpha ($ER\alpha$), a key biomarker protein in breast cancer. They found that this “aptasensor” could efficiently detect and quantify $ER\alpha$ in the range 10 ng/mL-5 μ g/mL protein.

In addition to isolating tumor cells, it is also necessary to understand the heterogeneity in biomarker expression to study their behavior. Hanif *et al.*⁴⁶ carried out single cell analysis in a variety of tumor cells including MCF-7A, HeLa and MCF-10A cells where they looked at variation in the expression of the protein nucleolin, which is an overexpressed marker in most cancer cells. They specifically looked at the variation of expression in different subcellular regions of the tumor cells since it influences cancer proliferation and treatments. They designed a portable gold coated nanopipette which was functionalized with an aptamer specific to nucleolin. Complementary DNA-modified Ag nanoparticles with the Raman reporter p-mercaptobenzonitrile were used to produce the SERS signal. In the absence of the target nucleolin, the DNA on the AgNPs formed a hybrid with the aptamer on the nanopipette and resulted in an increase in the SERS signal. The probe was then inserted into the nucleus, cytoplasm, and cell surface of the tumor cells to understand the spatial distribution and subcellular localization of nucleolin. This study shows potential in the detection of proteins at a single cell level that could perhaps have implications in cancer diagnosis and treatment.

1.9 Application of SERS in Tissue Imaging

SERS-based imaging using gold nanoparticle-based tags have been employed for protein localization in tissues although detection of cellular and tissue antigens is typically carried out using immunohistochemistry and immunofluorescence. One of the first uses

of SERS in tissue imaging was carried out by Schlücker *et al.*⁴⁷ in prostate tissue specimens to demonstrate the localization of prostate specific antigen (PSA), which is a protein expressed abundantly in the prostate tissue. They conjugated an anti-PSA antibody to a gold-silver nanoshell to detect the presence of PSA. They observed detectable Raman signals in the epithelium of the prostate tissue while no signal was observed in the stroma and the lumen. The sensitivity of the assay was later improved by using a silica coating on the gold-silver nanoshells.⁴⁸ Other studies include the work carried out by Lutz *et al.*⁴⁹ where they developed composite organic-inorganic nanoparticles (COINs) conjugated with a PSA antibody to look at their detection sensitivity in prostate tissue sections. The sensitivity of SERS detection was compared to immunofluorescence staining with an Alexafluor conjugated antibody. A slightly higher occurrence of false positive staining was observed with SERS, although overall the detection sensitivity and signal intensity observed were comparable with that seen with immunofluorescence staining. Most importantly, the SERS signal could be distinguished from the background autofluorescence of the tissue which is beneficial in analyzing proteins with low expression levels.

These studies show that gold nanoparticle-based SERS tags possess the specificity and ability to identify several targets simultaneously without spectral overlap. They further attest to the benefits of using gold nanoparticles based SERS for cancer and tissue biomarker identification.

1.10 Dissertation Hypothesis and Overview

The overall objective of this dissertation was to develop a SERS-based imaging tool for the phenotype identification of cancer cells and tissues by utilizing the optical properties of gold nanostars (i.e. gold nanoparticles with a spherical core and sharp protruding spikes) together with the effective targeting ability of aptamers. SERS tags are one of the promising techniques for the ultrasensitive and multiplexed detection of target molecules. It was hypothesized that gold nanostars would be able to provide excellent SERS enhancement factors that would enable the quantification of biomarker expression at the single cell level. Studies from our group using SERS tags developed from dimers of gold nanoparticles have shown that they are extremely sensitive and can selectively image cancerous cells.⁴⁰ These tags were therefore exploited for the molecular identification and quantification of cell surface biomarkers with extreme sensitivity and selectivity and yielded improved SERS-based detection limits for biological applications.

To achieve the overall objective of this dissertation, the following specific aims were designed: (1) To understand the cytotoxicity of gold nanoparticles with different morphologies and surface chemistries; (2) To develop aptamer-functionalized nanostars for the recognition of both soluble and cell-membrane embedded proteins that would enable the quantification of biomarker expression at the single cell level in cancer cells of different phenotype; (3) To develop SERS tags that would allow assessment of the clinical stage of prostate cancer using the prostate-specific PSMA biomarker.

The remaining chapters have been organized as below:

Chapter 2 provides information on how the shape of particles (like spheres, rods, and stars), size, and surface chemistry influences their cytotoxicity and establishes the need to understand their mechanism before implementing them in an *in vitro* or *in vivo* study. The deliverables included synthesizing and characterizing AuNPs with different morphologies (spheres, rods, and stars), followed by functionalizing them with the surfactant cetyltrimethylammonium bromide (CTAB), PEG, and human serum albumin (HSA). The performance of the nanoparticles was then studied via a multi-parametric *in vitro* study in glioblastoma cells (U-87) and fibroblasts. The biocompatibility was established with several assays such as MTT, lactate dehydrogenase (LDH), reactive oxygen species (ROS), and caspase 3/7 assays. Cellular uptake of the nanoparticles was analyzed with transmission electron microscopy (TEM) and inductively coupled plasma mass spectrometry (ICP-MS).

Chapter 3 focuses on the development of a SERS sensing platform that enabled the quantification of biomarker expression at the single cell level in cancer cells of different phenotype. For this work, the epithelial cell adhesion molecule (EpCAM) aptamer developed using cell-SELEX protocols was employed. The sensitivity of the assay was improved from 1 nM to 10 pM by using a truncated version of the EpCAM aptamer in which the number of nucleotides was drastically reduced from 48 nucleotides to 17 nucleotides. Performance of the sensing platform was assessed using atomic force microscopy (AFM), and SERS maps. The sensing platform was then used to quantify the expression of the EpCAM biomarker in two cancer cells, PC-3 and MCF-7, at the single cell level. Experiments carried out included measuring the cell capture efficiency on the

substrates and assessing their SERS signals. Population level predictions of EpCAM expression were carried out using flow cytometry.

Chapter 4 focuses on the development of gold nanostar-aptamer functionalized SERS tags that allowed the assessment of the clinical stage of prostate cancer in tissue microarrays using the prostate-specific PSMA biomarker. For this work, the prostate specific membrane antigen (PSMA) aptamer was employed. SERS maps were carried out to assess the performance of this assay. Following this initial assessment, the tags were employed to quantify the expression of the PSMA biomarker at the single cell level in the prostate cancer cells LNCaP and PC-3 using SERS maps. The PSMA expression on these cells was confirmed with Western Blot and RT-PCR analysis. Differences in the binding capability of PSMA antibody and PSMA aptamer to the prostate cancer cells were tested. The tags were then employed in a prostate tissue microarray containing samples from 38 patients with different disease stages. The difference in the expression of the PSMA biomarker observed via SERS maps at different stages of the disease was compared to that seen with immunofluorescence staining of the tissue microarray.

Chapter 5 contains the conclusion. Findings from all experiments carried out to satisfy the specific aims have been summarized and future research directions for the projects are discussed.

1.11 References

1. L., S. R.; D., M. K.; Ahmedin, J., Cancer statistics, 2018. *CA: A Cancer Journal for Clinicians* 2018, 68 (1), 7-30.
2. Sawyers, C. L., The cancer biomarker problem. *Nature* 2008, 452 (7187), 548-52.
3. Golubnitschaja, O.; Flammer, J., What are the biomarkers for glaucoma? *Surv Ophthalmol* 2007, 52 Suppl 2, S155-61.
4. Wu, L.; Qu, X., Cancer biomarker detection: recent achievements and challenges. *Chemical Society Reviews* 2015, 44 (10), 2963-2997.
5. Wang, X.; Qian, X.; Beitler, J. J.; Chen, Z. G.; Khuri, F. R.; Lewis, M. M.; Shin, H. J.; Nie, S.; Shin, D. M., Detection of circulating tumor cells in human peripheral blood using surface-enhanced Raman scattering nanoparticles. *Cancer Res* 2011, 71 (5), 1526-32.
6. Hong, B.; Zu, Y., Detecting circulating tumor cells: current challenges and new trends. *Theranostics* 2013, 3 (6), 377-94.
7. Millner, L. M.; Linder, M. W.; Valdes, R., Jr., Circulating tumor cells: a review of present methods and the need to identify heterogeneous phenotypes. *Annals of clinical and laboratory science* 2013, 43 (3), 295-304.
8. de la Rica, R.; Stevens, M. M., Plasmonic ELISA for the ultrasensitive detection of disease biomarkers with the naked eye. *Nature Nanotechnology* 2012, 7, 821.
9. Law, W. C.; Yong, K. T.; Baev, A.; Prasad, P. N., Sensitivity improved surface plasmon resonance biosensor for cancer biomarker detection based on plasmonic enhancement. *ACS Nano* 2011, 5 (6), 4858-64.
10. Labib, M.; Khan, N.; Ghobadloo, S. M.; Cheng, J.; Pezacki, J. P.; Berezovski, M. V., Three-Mode Electrochemical Sensing of Ultralow MicroRNA Levels. *Journal of the American Chemical Society* 2013, 135 (8), 3027-3038.
11. Wang, J.; Wu, L.; Ren, J.; Qu, X., Visualizing human telomerase activity with primer-modified Au nanoparticles. *Small* 2012, 8 (2), 259-64.
12. Rana, S.; Singla, A. K.; Bajaj, A.; Elci, S. G.; Miranda, O. R.; Mout, R.; Yan, B.; Jirik, F. R.; Rotello, V. M., Array-based sensing of metastatic cells and tissues using nanoparticle-fluorescent protein conjugates. *ACS Nano* 2012, 6 (9), 8233-40.
13. Petrovsky, A.; Schellenberger, E.; Josephson, L.; Weissleder, R.; Bogdanov, A., Jr., Near-infrared fluorescent imaging of tumor apoptosis. *Cancer research* 2003, 63 (8), 1936-42.
14. Keren, S.; Zavaleta, C.; Cheng, Z.; de la Zerda, A.; Gheysens, O.; Gambhir, S. S., Noninvasive molecular imaging of small living subjects using Raman spectroscopy. *Proceedings of the National Academy of Sciences of the United States of America* 2008, 105 (15), 5844-9.
15. Rosi, N. L.; Mirkin, C. A., Nanostructures in Biodiagnostics. *Chemical reviews* 2005, 105 (4), 1547-1562.
16. Huh, Y.; Chung, A.; Erickson, D., Surface enhanced Raman spectroscopy and its application to molecular and cellular analysis. *Microfluid Nanofluid* 2009, 6 (3), 285-297.
17. Paciotti, G. F.; Kingston, D. G. I.; Tamarkin, L., Colloidal gold nanoparticles: a novel nanoparticle platform for developing multifunctional tumor-targeted drug delivery vectors. *Drug Development Research* 2006, 67 (1), 47-54.

18. Thakor, A. S.; Jokerst, J.; Zavaleta, C.; Massoud, T. F.; Gambhir, S. S., Gold nanoparticles: a revival in precious metal administration to patients. *Nano letters* 2011, *11* (10), 4029-36.
19. Jeanmaire, D. L.; Van Duyne, R. P., Surface raman spectroelectrochemistry. *Journal of Electroanalytical Chemistry and Interfacial Electrochemistry* 1977, *84* (1), 1-20.
20. Hanlon, E. B.; Manoharan, R.; Koo, T. W.; Shafer, K. E.; Motz, J. T.; Fitzmaurice, M.; Kramer, J. R.; Itzkan, I.; Dasari, R. R.; Feld, M. S., Prospects for in vivo Raman spectroscopy. *Physics in medicine and biology* 2000, *45* (2), R1-59.
21. Scaffidi, J. P.; Gregas, M. K.; Seewaldt, V.; Vo-Dinh, T., SERS-based plasmonic nanobiosensing in single living cells. *Analytical and bioanalytical chemistry* 2009, *393* (4), 1135-41.
22. Willets, K. A.; Duyne, R. P. V., Localized Surface Plasmon Resonance Spectroscopy and Sensing. *Annual Review of Physical Chemistry* 2007, *58* (1), 267-297.
23. Moskovits, M., Surface-enhanced Raman spectroscopy: a brief retrospective. *Journal of Raman Spectroscopy* 2005, *36* (6-7), 485-496.
24. Cobley, C. M.; Xia, Y., Engineering the Properties of Metal Nanostructures via Galvanic Replacement Reactions. *Materials science & engineering. R, Reports : a review journal* 2010, *70* (3-6), 44-62.
25. Cai, W.; Gao, T.; Hong, H.; Sun, J., Applications of gold nanoparticles in cancer nanotechnology. *Nanotechnology, science and applications* 2008, *2008* (1).
26. Li, W.; Chen, X., Gold nanoparticles for photoacoustic imaging. *Nanomedicine (Lond)* 2015, *10* (2), 299-320.
27. Halas, N. J.; Lal, S.; Chang, W. S.; Link, S.; Nordlander, P., Plasmons in strongly coupled metallic nanostructures. *Chemical reviews* 2011, *111* (6), 3913-61.
28. Indrasekara, A. S. D. S.; Meyers, S.; Shubeita, S.; Feldman, L. C.; Gustafsson, T.; Fabris, L., Gold nanostar substrates for SERS-based chemical sensing in the femtomolar regime. *Nanoscale* 2014, *6* (15), 8891-8899.
29. Kleinman, S. L.; Frontiera, R. R.; Henry, A. I.; Dieringer, J. A.; Van Duyne, R. P., Creating, characterizing, and controlling chemistry with SERS hot spots. *Physical chemistry chemical physics : PCCP* 2013, *15* (1), 21-36.
30. Wang, Y.; Yan, B.; Chen, L., SERS Tags: Novel Optical Nanoprobes for Bioanalysis. *Chemical Reviews* 2013, *113* (3), 1391-1428.
31. Laura, F., SERS Tags: The Next Promising Tool for Personalized Cancer Detection? *ChemNanoMat* 2016, *2* (4), 249-258.
32. Pinkhasova, P.; Yang, L.; Zhang, Y.; Sukhishvili, S.; Du, H., Differential SERS Activity of Gold and Silver Nanostructures Enabled by Adsorbed Poly(vinylpyrrolidone). *Langmuir* 2012, *28* (5), 2529-2535.
33. Driskell, J. D.; Kwarta, K. M.; Lipert, R. J.; Porter, M. D.; Neill, J. D.; Ridpath, J. F., Low-Level Detection of Viral Pathogens by a Surface-Enhanced Raman Scattering Based Immunoassay. *Analytical Chemistry* 2005, *77* (19), 6147-6154.
34. Qian, X.; Peng, X. H.; Ansari, D. O.; Yin-Goen, Q.; Chen, G. Z.; Shin, D. M.; Yang, L.; Young, A. N.; Wang, M. D.; Nie, S., In vivo tumor targeting and spectroscopic detection with surface-enhanced Raman nanoparticle tags. *Nat Biotechnol* 2008, *26* (1), 83-90.

35. Weng, K. C.; Noble, C. O.; Papahadjopoulos-Sternberg, B.; Chen, F. F.; Drummond, D. C.; Kirpotin, D. B.; Wang, D.; Hom, Y. K.; Hann, B.; Park, J. W., Targeted tumor cell internalization and imaging of multifunctional quantum dot-conjugated immunoliposomes *in vitro* and *in vivo*. *Nano Lett* 2008, 8 (9), 2851-7.
36. Stöber, W.; Fink, A.; Bohn, E., Controlled growth of monodisperse silica spheres in the micron size range. *Journal of Colloid and Interface Science* 1968, 26 (1), 62-69.
37. Radom, F.; Jurek, P. M.; Mazurek, M. P.; Otlewski, J.; Jeleń, F., Aptamers: Molecules of great potential. *Biotechnology Advances* 2013, 31 (8), 1260-1274.
38. Cerchia, L.; de Franciscis, V., Targeting cancer cells with nucleic acid aptamers. *Trends in biotechnology* 2010, 28 (10), 517-25.
39. Dam, D. H.; Culver, K. S.; Odom, T. W., Grafting aptamers onto gold nanostars increases *in vitro* efficacy in a wide range of cancer cell types. *Molecular pharmaceutics* 2014, 11 (2), 580-7.
40. Indrasekara, A. S.; Paladini, B. J.; Naczynski, D. J.; Starovoytov, V.; Moghe, P. V.; Fabris, L., Dimeric gold nanoparticle assemblies as tags for SERS-based cancer detection. *Adv Healthc Mater* 2013, 2 (10), 1370-6.
41. Danila, D. C.; Fleisher, M.; Scher, H. I., Circulating tumor cells as biomarkers in prostate cancer. *Clinical cancer research : an official journal of the American Association for Cancer Research* 2011, 17 (12), 3903-12.
42. Akhter, S.; Ahmad, M. Z.; Ahmad, F. J.; Storm, G.; Kok, R. J., Gold nanoparticles in theranostic oncology: current state-of-the-art. *Expert opinion on drug delivery* 2012, 9 (10), 1225-43.
43. Zhang, P.; Zhang, R.; Gao, M.; Zhang, X., Novel nitrocellulose membrane substrate for efficient analysis of circulating tumor cells coupled with surface-enhanced Raman scattering imaging. *ACS applied materials & interfaces* 2014, 6 (1), 370-6.
44. Nima, Z. A.; Mahmood, M.; Xu, Y.; Mustafa, T.; Watanabe, F.; Nedosekin, D. A.; Juratli, M. A.; Fahmi, T.; Galanzha, E. I.; Nolan, J. P.; Basnakian, A. G.; Zharov, V. P.; Biris, A. S., Circulating tumor cell identification by functionalized silver-gold nanorods with multicolor, super-enhanced SERS and photothermal resonances. *Scientific reports* 2014, 4, 4752.
45. Ahirwar, R.; Nahar, P., Development of a label-free gold nanoparticle-based colorimetric aptasensor for detection of human estrogen receptor alpha. *Analytical and bioanalytical chemistry* 2015.
46. Hanif, S.; Liu, H.-L.; Ahmed, S. A.; Yang, J.-M.; Zhou, Y.; Pang, J.; Ji, L.-N.; Xia, X.-H.; Wang, K., Nanopipette-Based SERS Aptasensor for Subcellular Localization of Cancer Biomarker in Single Cells. *Analytical Chemistry* 2017, 89 (18), 9911-9917.
47. S., S.; B., K.; A., P.; R., B.; A., M.; P., S., Immuno-Raman microspectroscopy: In situ detection of antigens in tissue specimens by surface-enhanced Raman scattering. *Journal of Raman Spectroscopy* 2006, 37 (7), 719-721.
48. Kustner, B.; Gellner, M.; Schutz, M.; Schoppler, F.; Marx, A.; Strobel, P.; Adam, P.; Schmuck, C.; Schlucker, S., SERS labels for red laser excitation: silica-encapsulated SAMs on tunable gold/silver nanoshells. *Angew Chem Int Ed Engl* 2009, 48 (11), 1950-3.
49. Lutz, B.; Dentinger, C.; Sun, L.; Nguyen, L.; Zhang, J.; Chmura, A.; Allen, A.; Chan, S.; Knudsen, B., Raman nanoparticle probes for antibody-based protein detection in tissues. *J Histochem Cytochem* 2008, 56 (4), 371-9.

**CHAPTER 2 MULTIPARAMETRIC ASSESSMENT OF GOLD
NANOPARTICLE CYTOTOXICITY IN CANCEROUS AND HEALTHY CELLS:
THE ROLE OF SIZE, SHAPE AND SURFACE CHEMISTRY**

Note: This chapter has been reprinted (adapted) with permission from **Manjari Bhamidipati** and Laura Fabris. “Multiparametric Assessment of Gold Nanoparticle Cytotoxicity in Cancerous and Healthy Cells: The Role of Size, Shape, and Surface Chemistry”. *Bioconjugate Chemistry*, 28(2), 449–460, 2017. Copyright (2017) American Chemical Society.

2.1 Abstract

In recent years, we and others have become interested in evaluating the use of surface-enhanced Raman scattering (SERS) tags for early cancer detection and in designing new approaches to demonstrate the applicability of this spectroscopic technique in the clinic. SERS-based imaging in particular offers ultra sensitivity up to the single molecule, multiplexing capability, and increased photostability and has been shown to outperform fluorescence. However, to employ SERS tags for early cancer detection, it is important to understand their interaction with cells and determine their cytotoxicity. We have been particularly interested for quite some time in determining if and how gold nanostars, which have been demonstrated as outstanding SERS enhancing substrates, can be safely employed in living systems and translated to the clinic. In this study, we carried out a multiparametric *in vitro* study to look at the cytotoxicity and cellular uptake of gold nanoparticles on human glioblastoma and human dermal fibroblast cell lines. Cytotoxicity was evaluated by incubating cells with three different morphologies of AuNPs, namely nanospheres, nanorods, and nanostars, each having three different surface chemistries (cetyltrimethylammonium bromide (CTAB), poly(ethylene glycol) (PEG), and human serum albumin (HSA)). Our results showed that the surface chemistry of the nanoparticles had predominant effects on cytotoxicity, and the morphology and size of the nanoparticles only slightly affected cell viability. CTAB-coated particles were found to be the most toxic to cells, and PEGylated nanostars were determined to be the least toxic. Caspase-3 assay and LDH assay revealed that cell death occurs via apoptosis for cancerous cells and via necrosis for healthy ones. Cellular uptake studies carried out via TEM showed that the particles retain their shape even at long incubation times, which

may be beneficial for *in vivo* SERS-based disease detection. Overall, this study provides valuable information on gold-nanoparticle-induced cytotoxicity that can be leveraged for the development of safe and effective nanoparticle-based therapeutic and diagnostic systems.

2.2 Introduction

The use of noble metal nanoparticles (NPs) in a wide variety of biomedically relevant applications has steadily grown in recent years, raising concerns over their safety and true applicability *in vivo*. There is a common understanding that silver nanoparticles, by virtue of their redox properties, readily undergo oxidation at the surface, releasing Ag⁺ ions that can then lead to the production of reactive oxygen species (ROS) and thus be correlated with increased apoptotic and necrotic levels in various types of cell populations.¹ For this specific reason, Ag NPs are often used as antibacterials, but because of it, they are not as often encountered in *in vitro* and *in vivo* applications as much as gold NPs do. With respect to the latter, however, even though individual works generally provide basic cytotoxicity assessments, primarily carried out via MTT and trypan blue assays, there is a fundamental lack of systematic studies in which the size, shape, and surface chemistry of the Au NPs are all taken into account to provide a multiparametric evaluation of the biocompatibility of these materials. Moreover, the studies available in the literature mostly assess the toxicity of diseased cells that are being targeted in a specific application, ignoring the fact that, fundamentally, the most important cellular response to be monitored should be that of healthy cells, whose viability should not be impacted by NP administration. Importantly, certain studies,

although providing a broad cytotoxicity assessment for gold NPs of variable shape, do so by targeting HeLa cells, which are known to be extremely durable and prolific but, because of this reason, might not be the ideal cell type to use to provide accurate conclusions that can be generalized for the majority of mammalian cells. In our group, we are particularly interested in studying the cytotoxicity of gold nanostars because they are an ideal substrate for surface enhanced Raman scattering (SERS), a spectroscopic technique that is at the core of our research and can be leveraged for biomedical sensing, diagnostics, and imaging.²⁻⁴ We are primarily interested in the implementation of SERS for the indirect identification of healthy and diseased cells and for the development of multimodal contrast agents based on the concept of SERS tags.

SERS tags are composed of a plasmonic NP (in this case, gold), Raman reporter molecules, and targeting moieties such as antibodies, peptides, or aptamers and enable optical labeling functions, similar to what fluorescent dyes do in fluorescence microscopy.⁵ In SERS-based experiments, the presence of a probe molecule near the plasmonic nanoparticle enhances its Raman signal by 5–6 orders of magnitude, with values up to 10^{10} at the hot spots. These hot spots are usually found near the edges and vertices of sharp features on isolated NPs such as nanostars or at the junction between electromagnetically coupled nanoparticles such as dimers of nanospheres with interparticle gaps of 1–2 nm. The morphology of the plasmonic nanoparticles used can significantly influence its optical properties. Gold nanostars, in particular, can generate multiple hot spots and hence can be used as excellent platforms for SERS-based medical applications.⁵ They can produce SERS enhancement factors of almost 10^{10} , a value that is only 2 orders of magnitude lower than that necessary for single molecule detection.⁶

However, to use SERS tags *in vitro* or *in vivo*, it is important to understand their interaction with cells and the nature of the cytotoxic response they elicit in them. It has been shown that the shape of the nanoparticles, their size, and surface chemistry greatly influence their cytotoxicity.⁷ However, besides a recent work by Cormode and co-workers in which gold nanospheres and nanorods have been thoroughly evaluated via a multipronged toxicity assessment,⁸ no study of similar completeness has so far, to the best of our knowledge, provided a thorough, systematic comparison of the cytotoxicity of gold nanostars with respect to more well-known particles of comparable size and identical surface chemistry within an individual study covering both healthy and diseased cells and employing multiple toxicity assays and characterization tools. In this study, we carried out a detailed multiparametric *in vitro* study to look at the mechanisms of cytotoxicity and cellular uptake of gold nanoparticles on human glioblastoma (U87) and human dermal fibroblast cell lines focusing on spherical gold NPs, nanorods, and nanostars, functionalized with cetyltrimethylammonium bromide (CTAB), polyethylene glycol (PEG), and human serum albumin (HSA). We have evaluated cell viability via 3-(4, 5-dimethylthiazol-2-yl)-2,5-diphenyltetrazolium bromide (MTT), lactate dehydrogenase (LDH), ROS, and caspase 3/7 assays and studied uptake with transmission electron microscopy (TEM) and inductively coupled plasma mass spectrometry (ICP-MS). The overarching goal of this study was to determine the cytocompatibility of Au nanostars and hence facilitate their applicability as contrast agents in molecular imaging studies, particularly those carried out using SERS.

2.3 Experimental Section

2.3.1 Synthesis of AuNPs

Gold nanoparticles with three different morphologies were synthesized using established protocols from literature. ⁽⁹⁻¹¹⁾ Citrate capped gold nanospheres were synthesized according to a modified Turkevich method.⁽⁹⁾ Briefly, 8 mL of H_{AuCl}₄ salt solution (0.025 M) in milliQ water (477 mL) were heated up to boil after which citric acid trisodium salt (1% wt., 15 mL) was added under gentle stirring. After 5 minutes of boiling, the solution turned red and it was then allowed to cool to room temperature followed by centrifugation at 6000 g for 30 minutes to purify the nanospheres.

Gold nanorods were synthesized using a seed-mediated growth method developed by Nikoobakht and El Sayed.⁽¹⁰⁾ For the seed solution, 5 mL of 0.2 M CTAB solution were mixed with 5 mL of 0.822 mM H_{AuCl}₄. To the stirred solution, 600 μ L of ice cold 0.01 M NaBH₄ were added. The solution turned brownish yellow and was stirred vigorously for 2 min. For the growth solution, 243.1 mL of 0.2 M CTAB were mixed with 9.7 mL of 0.004 M AgNO₃. To this solution, 243.14 mL of 0.411 mM of H_{AuCl}₄ were added. After gentle mixing, 3.4 mL of 0.0794 M ascorbic acid were added which changed the color of the growth solution from dark yellow to colorless. This was followed by the addition of 583.5 μ L of the seed solution. The reaction was maintained in a water bath at 30 $^{\circ}$ C under mild stirring conditions. The rods were then purified by centrifugation at 3500 g for 15 minutes.

Gold nanostars were synthesized according to a modified version of the surfactant-free nanostar synthesis described by Yuan *et al.*⁽¹¹⁾ Briefly, 12 mL of H_{AuCl}₄ salt solution

(0.025 M), 1.2 mL of 1 N HCl were added to 288 mL of milliQ water. 750 μ L of 12 nm citrate capped spheres ($A=2.81$) were then added to the mixture and mixed thoroughly by stirring. Then, 6 mL of 100 mM ascorbic acid and 12 mL of 3 mM AgNO_3 were simultaneously added to the above mixture. The reaction was carried out for 7 minutes with gentle stirring and then purified by centrifugation at 3000 g for 15 minutes.

2.3.2 Surface Functionalization of AuNPs

For surface functionalization of AuNPs with CTAB, as synthesized citrate capped spheres were purified and resuspended at a concentration of 100 $\mu\text{g/mL}$. To 50 mL of nanospheres, 5 mL of a 0.5 M CTAB solution were added. The nanospheres solution was sonicated for a few seconds and placed on a shaker for one hour. It was then centrifuged twice at 6000 g for 15 minutes. For CTAB coating of surfactant-free nanostars, 58.2 mL of 0.5 M CTAB was added to the as synthesized nanostars described previously. The suspension was stirred for an hour at room temperature followed by centrifugation twice at 4000 g for 15 minutes.

All thiolated molecules used in this work were pre-treated with Cleland's reagent (Dithiothreitol, DTT) to eliminate any existing disulfide bonds.⁽²²⁾ For PEG addition, 100 $\mu\text{g/mL}$ suspensions of AuNPs were prepared. A stock solution of 1 mg/mL hetero-bi-functional PEG (HS-PEG-OCH₃, M.W. 5000 Da) was prepared in milliQ water. Citrate capped nanospheres were centrifuged once at 6000 g for 15 min followed by the addition of 420 μL of 1 mg/mL PEG solution to the nanospheres pellet. The PEG coated spheres were then sonicated for a few seconds and placed on a shaker for a few hours. Surface functionalization of CTAB nanorods and surfactant-free nanostars with HS-mPEG was

carried out according to the method described by Liu *et al.* ⁽²³⁾ Briefly, 5 μL of 2 vol % Tween 20 aqueous solution, 5 μL of 0.1 M bis(p-sulfonatophenyl)-phenylphosphine dihydrate dipotassium salt (BSPP), 12.6 μL of 1.6 mM HS-mPEG ([HS-PEG]/[AuNP] = 1.24×10^5), 50 μL of 2 M NaCl, and 30 μL of water were added in that order to 100 μL of concentrated AuNP pellet. They were then sonicated for a few seconds followed by stirring at room temperature for a few hours.

Functionalization of AuNPs with HSA was carried out in two steps. For the first step, a stock solution of 1 mg/mL hetero-bi functional PEG (HS-PEG-COOH, M.W. 5000 Da) was prepared in pH 12 milliQ water. All AuNPs were centrifuged once. To the AuNP pellet, 135 μL (for citrate capped spheres), 150 μL (for CTAB nanorods) and 155 μL (for CTAB nanostars) of 1 mg/mL PEG solution were added. They were sonicated for 30 seconds followed by stirring for a few hours. Further functionalization of AuNPs with HSA was achieved via the addition of 1-Ethyl-3-(3-dimethylaminopropyl) carbodiimide (EDC, 25 μM in 10 mM MES) and *N*-Hydroxysuccinimide (NHS-ester, 25 μM in 10 mM MES) to the solution of PEG stabilized AuNPs. This was immediately followed by the addition of HSA (0.1 μM final in milliQ water). The binding was allowed to proceed for 3 hours at 37°C with gentle stirring. The AuNP solution was then centrifuged once and resuspended in 1X PBS with 0.05 % Tween 20 solution. It was then stored at 4°C until further use.

2.3.3 Characterization of AuNPs

The UV-Vis spectra were recorded on an SI Photonics Model 440 spectrophotometer. The morphology of AuNPs was evaluated using a Topcon 002B transmission electron

microscope and the size information was extracted using the Image J software. The concentrations of spherical AuNPs were calculated using the equation developed by Liu *et al.*⁽²⁴⁾

DLS and zeta potential measurements were performed using a Malvern Zetasizer Nano-S instrument. Three sequential measurements were performed for both experiments using water diluent parameters with flow cell configuration. The zetapotential data were fit using Smoluchowski theory.

2.3.4 Estimation of Ligand Concentrations on AuNPs

For estimation of CTAB concentrations on AuNPs, 100 mL of nanospheres, nanorods and nanostars were synthesized according to the protocol described above. All AuNPs were centrifuged twice, their supernatant was removed and the pellets were then re-suspended in 1mL of deuterated water (Sigma). CTAB concentrations were estimated via ¹H NMR spectrum that was obtained on a 500 MHz Varian spectrometer. ¹H NMR chemical shifts were reported in ppm downfield from tetramethylsilane and were referenced to deuterated water solvent. The concentrations on AuNPs were determined using a CTAB standard solution (3.7 mg, 10.5 mmol) that was dissolved in deuterated water at 35°C.

PEG concentrations on AuNPs were estimated using thermo gravimetric analysis (TGA). TGA was carried out using a Simultaneous Thermal Analyzer STA 8000 (Perkin Elmer). The experiments were carried out between 35°C and 800°C at 10°C/min under a nitrogen atmosphere flowing at 30 mL/min. Each sample was prepared by drying the washed

AuNP samples (100 mL each). The amount of PEG attachment on the AuNPs was calculated as the percentage weight loss that occurs between 302°C and 450°C which corresponds to the degradation of SH-mPEG (5000 Da).

HSA concentrations on AuNPs were estimated using a Pierce BCA Protein Assay kit (Thermo Scientific). AuNPs functionalized with HSA were synthesized according to the method described above. The AuNPs were centrifuged and the amount of excess HSA present in the supernatant as well as the initial HSA added to the synthesis was estimated using the BCA assay kit according to the manufacturer's protocol.

2.3.5 Cell Culture Maintenance

Human glioblastoma cells (U87, passage 5 to 11) and primary human dermal fibroblasts (passage 20 to 28) were maintained in Dulbecco's Modified Eagle Medium (DMEM) cell culture medium that was supplemented with Fetal Bovine Serum (FBS) (10% v/v) and penicillin/streptomycin (1% v/v). Cells were incubated at 37°C in a 5 % CO₂ environment. Cells were cultured in a 96-well plate at different seeding densities. 100 µL of cell culture medium containing AuNPs at a concentration of 100 µg/mL were added to each well 24 hours after plating. The wells were incubated with AuNPs for the chosen time (4 hours and 24 hours) and then analyzed for toxicity. Each experiment had a control group (cells grown in medium without AuNPs) and was performed in triplicate.

2.3.6 *In vitro* Cell Toxicity Studies

Actively growing cells were seeded at a density of 10,000 cells/well (100 µL) in a 96-well tissue culture plate for MTT assay. After allowing cells to attach for 24 hours, the

media was replaced and nine different groups of AuNPs at a concentration of 100 $\mu\text{g}/\text{mL}$ were added to the wells. Cell viability was measured after 4 and 24 hours of exposure to AuNPs using an MTT cell proliferation assay (V13154 Vybrant MTT Cell Proliferation Assay Kit, Thermo Fisher) according to the manufacturer's protocol. Briefly, after the completion of 4 hours and 24 hours, the aged media was replaced with 100 μL of fresh one. Following this, 10 μL of 12 mM MTT (3-(4, 5-dimethylthiazol-2-yl)-2, 5-diphenyltetrazolium bromide) were added to each well and incubated at 37 $^{\circ}\text{C}$ for 4 hours. About 85 μL of media were removed from each well and replaced with 50 μL of dimethylsulfoxide (DMSO). The wells were then incubated at 37 $^{\circ}\text{C}$ for 10 minutes. The water soluble MTT was reduced to an insoluble purple formazan dye crystals by metabolically active cells, and the concentration was determined by measuring the optical density at 540 nm.

For analyzing the cellular cytotoxicity via lactate dehydrogenase (LDH) release from cells, U-87 cells were plated at a density of 3000 cells/ well while fibroblasts were plated at a density of 10,000 cells/well in a 96-well tissue culture plate. The optimum cell density for each cell type was determined according to Pierce LDH Cytotoxicity Assay Kit (Thermo Fisher) protocol. After allowing the cells to attach for 24 hours followed by incubation for the desired time with AuNPs, 50 μL of the supernatant were collected to analyze LDH release using the assay kit. The reaction was carried out according to the manufacturer's protocol and the absorption was measured at 490 nm and 680 nm.

In order to monitor the cellular reactive oxygen species (ROS) generated in the cells, a DCFDA Cellular ROS Detection Assay Kit (Abcam) was used. Both cell lines were seeded at a density of 10,000 cells/well in a 96-well tissue culture plate. The cells were

incubated with 25 μM of 2', 7'-dichlorofluorescein diacetate (DCFDA) for 45 minutes in the dark at 37°C according to the manufacturer's protocol. The cells were then washed with 100 μL of 1X PBS. The fluorescent signal was recorded at an excitation of 485 nm and emission at 535 nm. The cells were then incubated with different AuNPs for the desired time and measured to determine the ROS content.

To investigate whether exposure to AuNPs induces apoptosis in cells, we used an EnzChek Caspase-3 Assay Kit by Thermo Fisher. This kit allows the detection of apoptosis by looking for increase in the expression of caspase-3 and Asp-Glu-Val-Asp (DEVD) specific protease like caspase 7. For this assay, both cell lines were seeded at a density of 20,000 cells/well in a 96-well tissue culture plate. After allowing the cells to attach for 24 hours and incubating with AuNPs for 4 hours and 24 hours, the cells were washed with 1X PBS. The cells were then lysed with a lysis buffer and incubated with rhodamine 110 bis-(N-CBZ-L-aspartyl-L-glutamyl-L-valyl-L-aspartic acid amide) (Z-DEVD-R110) according to the manufacturer's instructions. The fluorescence was then measured at an excitation/emission of 496 nm and 520 nm respectively.

2.3.7 Cellular Uptake Studies

For the preparation of cellular samples for TEM, U87 cells and fibroblasts were seeded at a density of 40,000 cells/cm² in a T-25 tissue culture flask. The cells were allowed to attach for 24 hours after which they were exposed to 100 $\mu\text{g}/\text{mL}$ (5 mL) of PEG and HSA coated gold nanostars for 24 hours. Following incubation, the cells were washed once with 1X PBS. They were trypsinized, centrifuged at 1500 rpm for 5 minutes and washed again with 1X PBS. The cells were then fixed in 1.5 mL of fixative (2.5 % glutaraldehyde

and 4 % formaldehyde in 0.1 M cacodylate buffer at pH 7.4) and left at room temperature for 2 hours. After that, they were stored at 4 °C until further analysis by TEM.

Quantification of metal concentration inside the cells was performed by acid digestion of the cell samples followed by ICP-MS analysis. Cells were incubated at a density of 10,000 cells/well in a 96-well tissue culture plate. They were allowed to attach for 24 hours after which they were incubated with different groups of AuNPs. After 4 hours and 24 hours, the cells were washed twice with ice cold 1X PBS. The cells were then scraped from the wells and collected in 100 μ L of 1X PBS. After this, 300 μ L of concentrated nitric acid (70 %) was added to the cell suspension. They were allowed to sit for an hour at room temperature after which they were microwave digested. They were then re-suspended in 100 μ L of concentrated hydrochloric acid and diluted to 8 mL using milliQ water. Following this, they were analyzed for metal concentration using ICP-MS.

2.3.8 Statistical Analyses

Statistical analyses were performed using a single factor analysis of variance with a Tukey's post hoc test (ANOVA) in Origin 9.3 software. All quantitative results (numerical values and representative diagrams) were expressed as the average \pm standard deviation.

2.4 Results and Discussion

2.4.1 Synthesis and Characterization of Functionalized AuNPs

A monodispersed suspension of gold nanospheres (AuNSp) of 25 nm in diameter was synthesized using a modified Turkevich method,⁽⁹⁾ which involves the citrate reduction of

the gold salt, HAuCl_4 . The synthesized spheres showed the characteristic UV-Vis plasmon resonance peak at 521 nm. Gold nanorods (AuNR) were synthesized using a seed mediated growth method adapted from Nikoobakht and El Sayed.⁽¹⁰⁾ UV-Vis data (**Figure 2.1**) showed the transverse plasmon resonance peak at 517 nm and the longitudinal resonance peak at 645 nm. Finally, gold nanostars (AuNS) having a plasmon resonance maximum centered at 774 nm were synthesized according to a modified version of the surfactant-free nanostar synthesis method we previously adopted.⁽¹¹⁾ Cetyltrimethylammonium bromide (CTAB) was then employed to recap the nanostars by replacing the ascorbic acid molecules stabilizing the surface of the as-synthesized NSs.

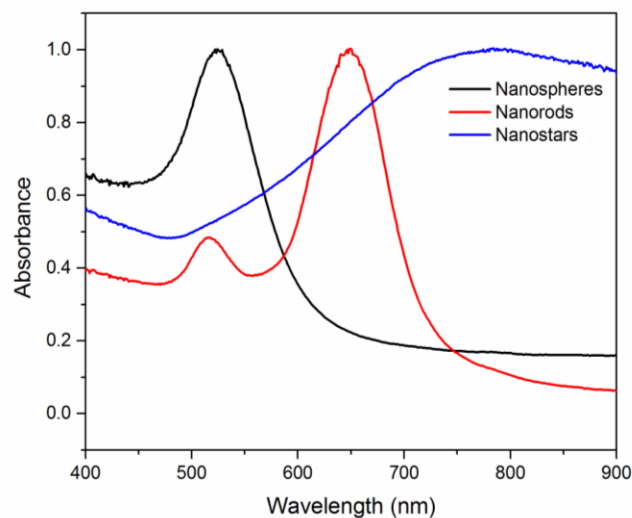


Figure 2.1 UV-Vis absorption spectra (normalized) of as synthesized gold nanospheres (LSPR: 521 nm), gold nanorods (LSPR: 517 nm, 645 nm) and gold nanostars (LSPR: 774 nm).

The morphology and size of all the particles were verified using transmission electron microscopy (TEM), as seen in **Figure 2.2**. TEM data showed that the AuNSp have a relatively narrow size distribution, with an average diameter of 18.4 ± 1.9 nm. The

AuNRs showed an average length of 52.7 ± 5.9 nm and a width of 23.0 ± 3.6 nm, thereby having an aspect ratio (length/width ratio) of 2.2 for the synthesized CTAB-coated gold nanorods. The TEM micrographs for the AuNSs showed a spherical core with a large number of tips at the surface. The average tip-to-tip distance was measured to be 62.5 ± 11.2 nm.

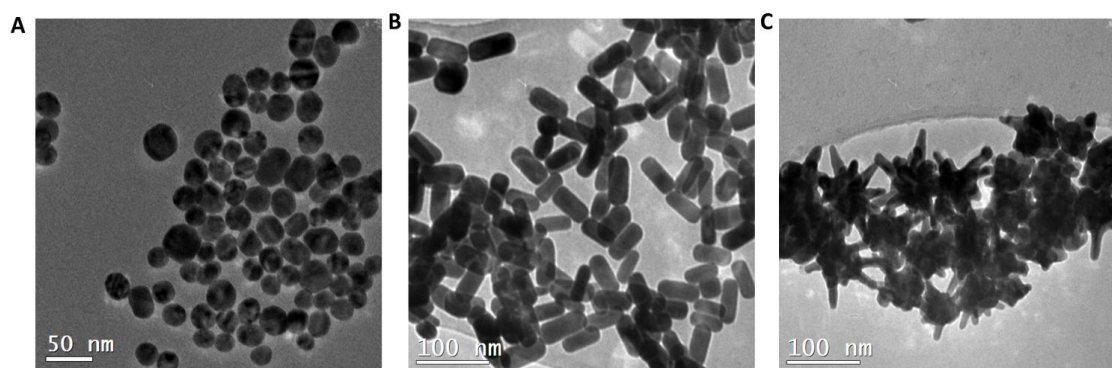


Figure 2.2 Representative transmission electron microscopy (TEM) images of CTAB coated (A) nanospheres (B) nanorods and (C) nanostars. Scale bar = 50 nm for nanospheres and 100 nm for nanorods and nanostars.

Surface functionalization of the nanoparticles was carried out following the analysis of particle size and morphology. Three different surface chemistries were utilized for the study: CTAB, PEG, and HSA. For the AuNSp group, the citrate spheres were further re-suspended in CTAB to keep the surface chemistry consistent with the other two types of AuNPs. For PEG coating of AuNPs, a thiolated PEG was employed for ligand exchange, while HSA addition was carried out in two steps. Upon the addition of thiolated PEG (SH-PEG, MW 5000) to the AuNP suspension, the high reactivity of the thiol groups toward gold causes ligand exchange of either the citrate ions (in the case of AuNSp), or CTAB (in AuNR), or ascorbic acid (in AuNS). Thiolated PEG molecules covalently bind

to the AuNP surface and provide colloidal stability. For HSA coating, hetero-bifunctional PEG (COOH-PEG-SH, MW 5000) was first added to the AuNP suspensions. This step minimizes aggregation of NPs due to the presence of proteins in the cell culture medium while the presence of the carboxylic moiety enables further functionalization of the AuNP surface by following simple amine chemistry. Formation of an amide bond with pendant *N-terminus* of HSA was achieved via coupling reactions mediated by 1-ethyl-3-(3-dimethylaminopropyl) carbodiimide (EDC) and *N*-hydroxysuccinimide (NHS-ester). After surface functionalization, all AuNPs showed an increase in size and a shift in the LSPR position (**Figure 2.3**). Since the position of LSPR is dependent on the thickness of the shell and dielectric function of the attached ligand (along with the size and shape of the NP),⁽¹²⁾ a shift indicates successful surface functionalization, with significant shifts for nanorods and nanostars and less pronounced ones for nanospheres, as expected. In UV-Vis spectroscopy experiments, a minor red shift of less than 5 nm in the plasmon peak was observed after surface functionalization of AuNSp, as typically observed for this type of particle.

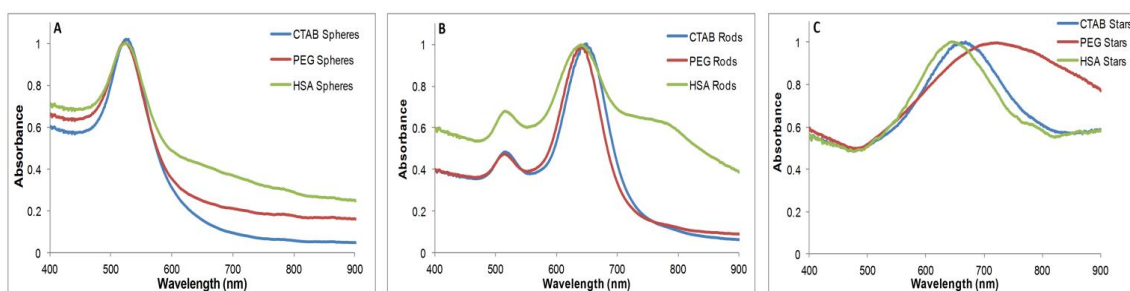


Figure 2.3 Characterization of the functionalized AuNPs. Panels (A) to (C) show the UV-vis spectra of CTAB-, PEG-, and HSA-coated nanospheres, nanostars, and nanorods respectively.

In addition to that, the dynamic light scattering (DLS) measurements shown in **Figure 2.4** revealed an increase in the average hydrodynamic diameter of spherical NP from 25.1 ± 0.2 nm (citrate NSp) to 35.2 ± 1.4 nm for CTAB coated nanospheres. PEG coated spheres showed a 5 nm increase in diameter (30.5 ± 0.7 nm) while HSA coated spheres increased by 14 nm (39.4 ± 0.4 nm), indicating successful functionalization of AuNSp with PEG and HSA. For AuNRs, the longitudinal plasmon peak position shifted from 645 nm in CTAB rods to 640 nm for both PEG and HSA coated rods. In addition to that, the broadening of the LSPR band observed for HSA-capped AuNRs suggests a sidewise pairing of nanorods, which was evidenced in TEM. For the gold nanostars, the surfactant-free stars (i.e. capped only by ascorbic acid) showed an LSPR peak at 778 nm. This coating wasn't used for the cytotoxicity experiments due to the poor colloidal stability of the resulting nanoparticles in cell culture media. To improve their stability, either thiolated PEG or CTAB were added. CTAB-coated stars were further functionalized with hetero-bifunctional PEG and later with HSA. CTAB addition caused a blue shift of over 100 nm to 668 nm while the PEG coated particles were found to have an LSPR at 721 nm, which only shifted by 57 nm. The addition of HSA resulted in a peak position at 645 nm. DLS measurements showed changes in the average hydrodynamic diameter of nanostars from 80.0 ± 0.5 nm for CTAB nanostars to 83.9 ± 3.0 nm (PEG nanostars) and 82.2 ± 2.7 nm (HSA nanostars). DLS measurements are based on an algorithm that correlates the diffusion coefficient with particle size based on the Brownian motion of spherical particles. Since AuNRs are non-spherical in shape, their DLS results would be inaccurate and hence measurements for this NP shape weren't carried out.⁽¹³⁾

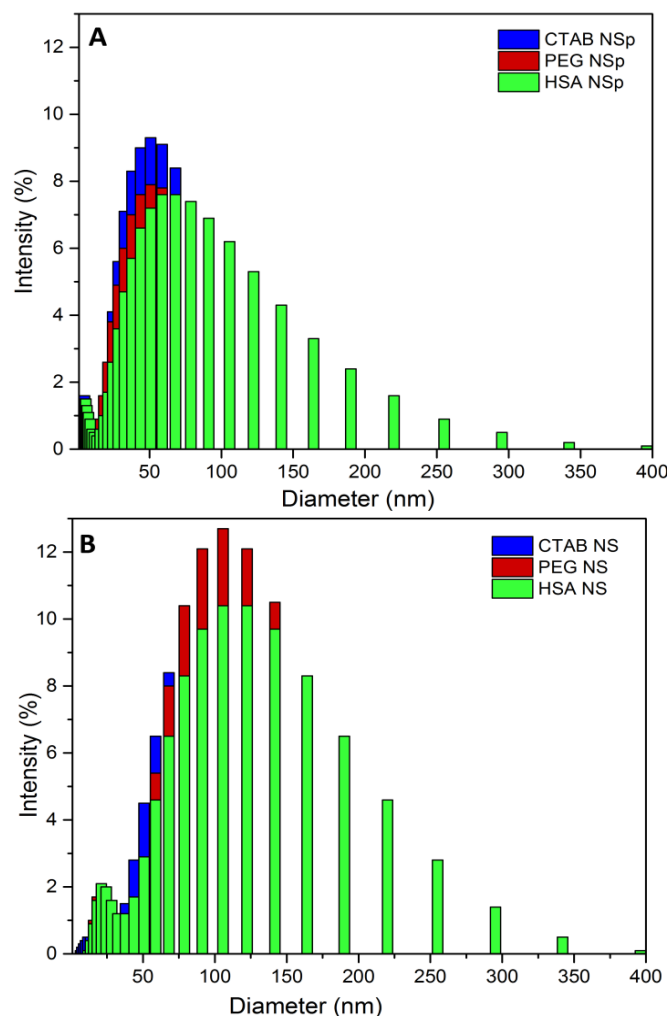


Figure 2.4 Plots A and B show dynamic light scattering (DLS) data that give the size distributions of CTAB, PEG, and HSA coated spheres and stars in Milli-Q water at room temperature.

The surface ligand exchange was further confirmed by a shift of zeta potential of the colloidal nanoparticles measured by the Zetasizer. The ζ -potential is a measure of the electrophoretic mobility or net charge of NPs. The results of the surface charges of all AuNPs have been summarized in **Table 2.1**. We observed a shift in ζ potential from -36.1 ± 0.6 mV to 25.4 ± 1.6 mV after addition of CTAB to citrate NSp. PEG and HSA coated NSp had near neutral ζ values at -14.2 ± 0.9 mV and -13.9 ± 0.1 mV. For AuNRs, the

zeta potential values shifted from 38.4 ± 1.2 mV in CTAB to 1.3 ± 0.3 mV and -7.6 ± 0.3 mV for PEG and HSA coatings respectively. In case of AuNS, the values decreased from 43.5 ± 1.5 mV of CTAB to -8.2 ± 0.8 mV in case of PEG AuNS and -7.6 ± 0.5 mV for HSA AuNS. For all three types of PEG-coated AuNPs, the surface charge was found to decrease to near neutral zeta potential values which is in agreement with values found in literature.⁽¹⁴⁾ Nanoparticle surface neutrality is known to provide colloidal stability as well as increased biocompatibility. It has also been shown to decrease non-specific binding of proteins and other bio-molecules to the AuNP surface and to help improve distribution of AuNPs in biological fluids.⁽¹⁵⁾ The zeta potential values for HSA-coated NPs were also similar to those found in literature.⁽¹⁶⁾

Table 2.1 Zeta potential values (mV) of AuNPs in water observed after synthesis and functionalization with different surface coatings. Results shown as mean \pm standard deviation with n = 3 readings for each sample.

AuNP	CTAB	HS-mPEG	HSA
Spheres	25.4 ± 1.6	-14.2 ± 0.9	-13.9 ± 0.1
Rods	38.4 ± 1.2	1.3 ± 0.3	-7.6 ± 0.3
Stars	43.5 ± 0.8	-8.2 ± 0.8	-7.6 ± 0.5

2.4.2 Estimation of Ligand Concentrations on AuNPs

The amount of ligands (CTAB, PEG and HSA) present on different AuNPs was quantified in order to understand the effect of ligands alone on cytotoxicity. CTAB concentrations on AuNPs were determined by comparing against the ^1H NMR spectrum of a CTAB standard solution. The peak areas corresponding to the terminal H of the CH_3

group present in CTAB solution were compared to each of the AuNP solutions. The following ^1H NMR peaks (500 MHz, 25°C , $\text{H}_2\text{O}-d_2$): δ 3.20 (11 H, $\text{C}(\text{CH}_3)_3$, CH_2), δ 2.24 (6 H, $(\text{CH}_2)_4$), δ 1.33 (22 H, $(\text{CH}_2)_{11}$), δ 0.91 (t, $J_{\text{HH}} = 11$ Hz, 3H, CH_3) were used to estimate CTAB concentrations in 100 mL of synthesized AuNPs. We determined that 2.168 mg of CTAB was present in nanospheres, 1.148 mg of CTAB in nanorods and 2.041 mg of CTAB was present in nanostars (**Figure 2.5**).

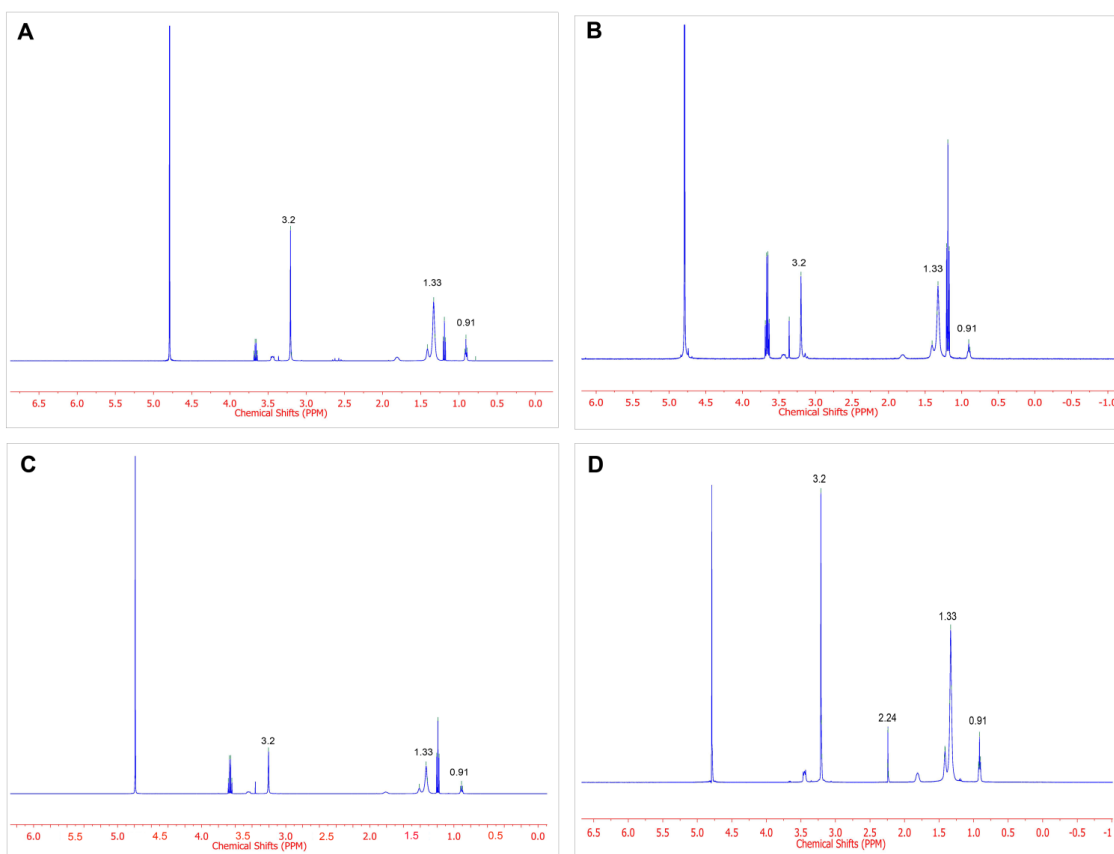


Figure 2.5 Figure shows ^1H NMR spectra of CTAB coated AuNPs. Panels show the spectra corresponding to A) CTAB nanospheres, B) CTAB nanorods, C) CTAB nanostars and D) a CTAB stock solution. ^1H NMR chemical shifts are reported in ppm downfield from tetramethylsilane and were referenced to deuterated water solvent.

PEG concentrations on AuNPs were determined using TGA (**Figure 2.6**) and compared to an as received PEG sample. The amount of PEG attachment on the AuNPs was calculated as the percentage weight loss that occurs between 302°C and 450°C which corresponds to the thermal degradation of the polymer.⁽¹⁷⁾ For the AuNP samples, additional peaks were observed. Highest weight loss percentages (6.759 wt %) were observed in spheres indicating higher PEG attachments compared to other AuNPs. This weight loss corresponded to 0.307 mg in nanospheres. For nanorods, a weight loss percent of 2.92 (0.136 mg) was observed while nanostars had 2.09 % weight loss (0.274 mg).

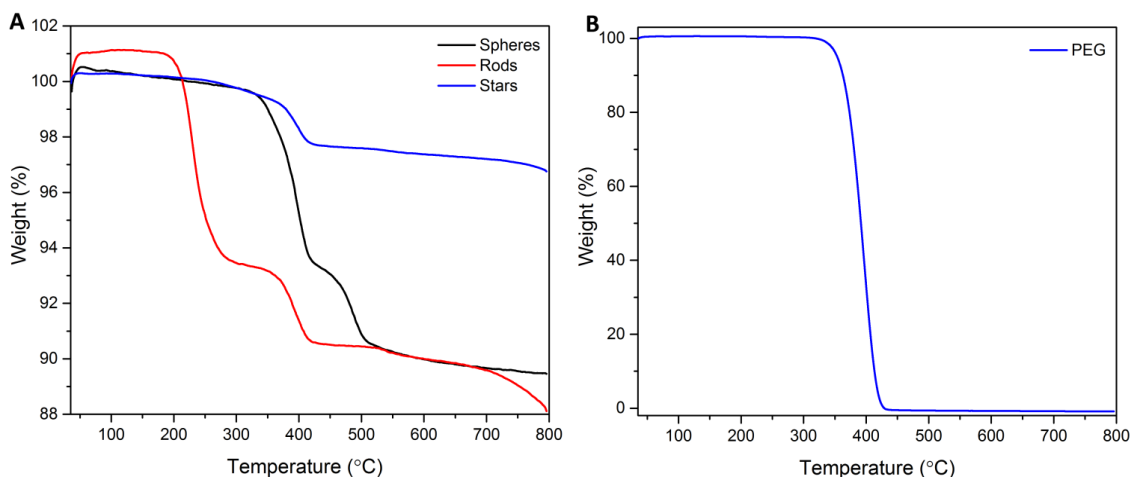


Figure 2.6 Figure shows TGA of PEG coated AuNPs. Panel A shows the weight loss profile of PEG coated nanospheres, nanorods and nanostars. Panel B shows the weight loss observed in as-received PEG between 35°C and 800°C.

HSA concentrations on AuNPs were determined using a Pierce BCA assay kit (Figure not shown). The initial amount of HSA added to each of the AuNP samples was found to be $151.5 \pm 16.2 \mu\text{g}$. The amount of HSA present in the supernatant of AuNPs were below the detection limit of the kit (less than $20 \mu\text{g/mL}$) so accurate HSA concentrations

couldn't be determined. For the cytotoxicity study, HSA concentrations of 20 μg , 100 μg and 151.5 μg (in 50 mL of as synthesized AuNPs) were used.

2.4.3 *In vitro* toxicity study

The primary objective of this study was to elucidate whether the cytotoxicity of gold nanoparticles was due to the size, the shape, or the surface chemistry of the particles, or a combination of all, and to identify whether it depended on the nature of the cell examined. For this purpose, comparisons were made between U87 and human dermal fibroblast (hfb) cells. We also investigated the amount of internalized AuNPs and the effect of different capping agents, such as PEG and HSA, on the uptake of gold nanoparticles. To determine if AuNPs exhibit cytotoxic effects on U87 and hfb, the cells were initially exposed to a broad concentration range of PEG nanostars (0 to 200 $\mu\text{g}/\text{mL}$) in order to find the optimal dosage for the study. Cell viability was measured after 4 and 24 hours of exposure to PEG nanostars using an MTT cell proliferation assay (**Figure 2.7**) which measures the enzymatic activity of cellular mitochondria. Cellular viabilities were plotted with respect to the untreated control cells. Initial treatments showed that after 24 hours there were no significant differences in cell viability at different concentrations in both cells. At the highest concentrations of 100 and 200 $\mu\text{g}/\text{mL}$, cell viability was reduced to 75.8 ± 17 and 78.3 ± 9.3 respectively in U87 cells (**Figure 2.7 A**). Since no significant reduction in cell viability was observed, AuNP concentrations at a 100 $\mu\text{g}/\text{mL}$ were chosen for the remainder of the study.

A control study looking at the effect of only ligands (CTAB, PEG and HSA) on cytotoxicity at concentrations that would be present in 100 $\mu\text{g}/\text{mL}$ of AuNPs was also

carried out (**Figure 2.7 C and D**). In U87 cells, it was observed that CTAB concentrations that correspond to nanospheres had significantly lower cell viability than that seen in nanorods ($p = 0.0002$) and nanostars ($p = 0.01802$) at 4 hours. Cell viabilities in CTAB samples dropped to under 5 % at 24 hours in both U87 cells and fibroblasts. Cell viabilities at different PEG concentrations showed no significant differences in both cell lines. However, increasing the HSA concentrations from concentrations 20 μg to 151.5 μg caused a significant decrease in U87 cells after 24 hours ($p = 0.0106$) while significant differences weren't seen in fibroblasts.

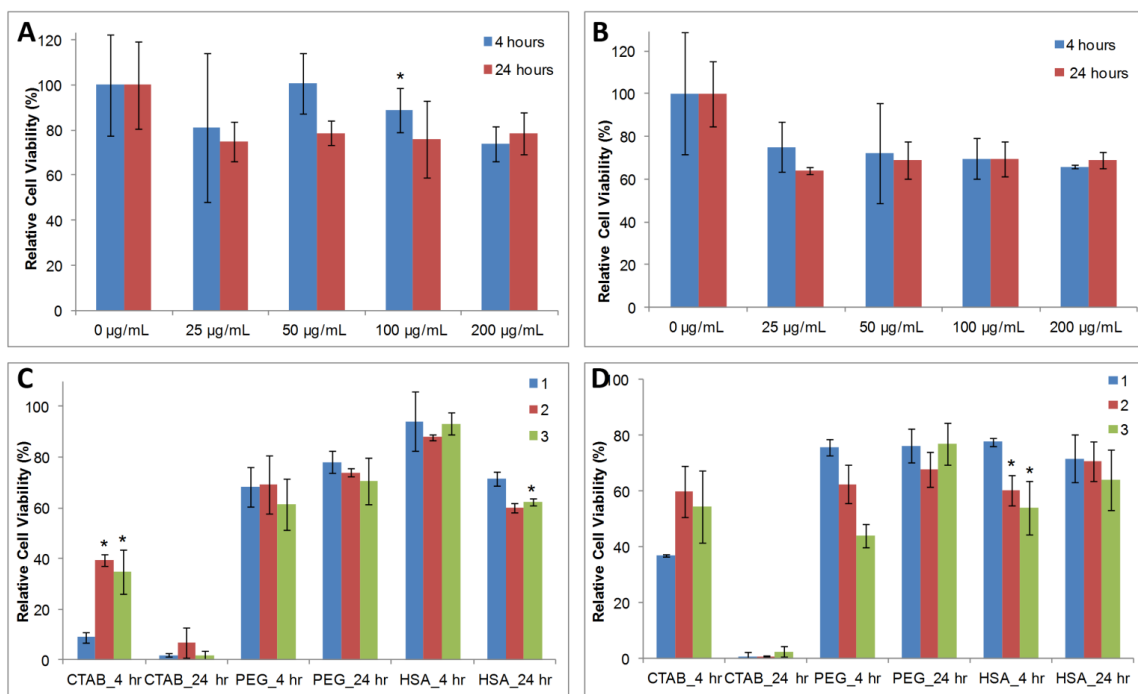


Figure 2.7 Cell viability results via MTT proliferation assay results have been shown here. Panels A and B show results after exposure to PEG nanostars at various concentrations after 4 hours and 24 hours in U87 cells and fibroblasts respectively. Statistically significant difference * = from the previous lower concentration at that time point ($p < 0.05$). Panels C and D show the cell viability results after exposure to CTAB, PEG and HSA at different concentrations in U87 cells and fibroblasts respectively. Legends represent concentrations of CTAB, PEG and HSA observed in 100 $\mu\text{g/mL}$ of 1: nanospheres, 2: nanorods and 3: nanostars. Viability values in all panels have been

normalized to control (without nanoparticles). Error bars represent standard deviation with $n = 3$. Statistically significant difference * = from nanospheres within the same surface coating at that time point ($p < 0.05$).

To determine if AuNPs exhibit cytotoxic effects on U87 and hfb, the cells were exposed to 100 $\mu\text{g/mL}$ of different AuNPs (CTAB, PEG and HSA coated NSp, NR and NS) for 24 hours. Cell viability was measured after 4 and 24 hours of exposure to AuNPs using an MTT cell proliferation assay (**Figure 2.8**). Cellular viabilities were plotted with respect to the untreated control cells (Viabilities plotted without normalization to control is shown in **Figure 2.9**). Cell viability in both cell lines was found to be the lowest when exposed to CTAB NSp. Only 14% of the cells were viable after 24 hours, while in comparison CTAB-coated NRs and NSs performed better. PEGylated NSp performed better in U87 cells than in fibroblasts. However, PEG- and HSA-capped rods and stars had similar cellular viabilities and were not different from the untreated control group. **Figure 2.8C** shows the viability of gold nanostars in both cell lines; we can see that cell viability decreases in a time-dependent manner (4 hrs vs. 24 hrs) in both cell lines with slightly higher values in U87 cells. This initial viability assay demonstrated that there could be differences in the biological response due to particle shape in CTAB coated NPs while PEG and HSA coated NPs did not seem to elicit any shape-related effects.

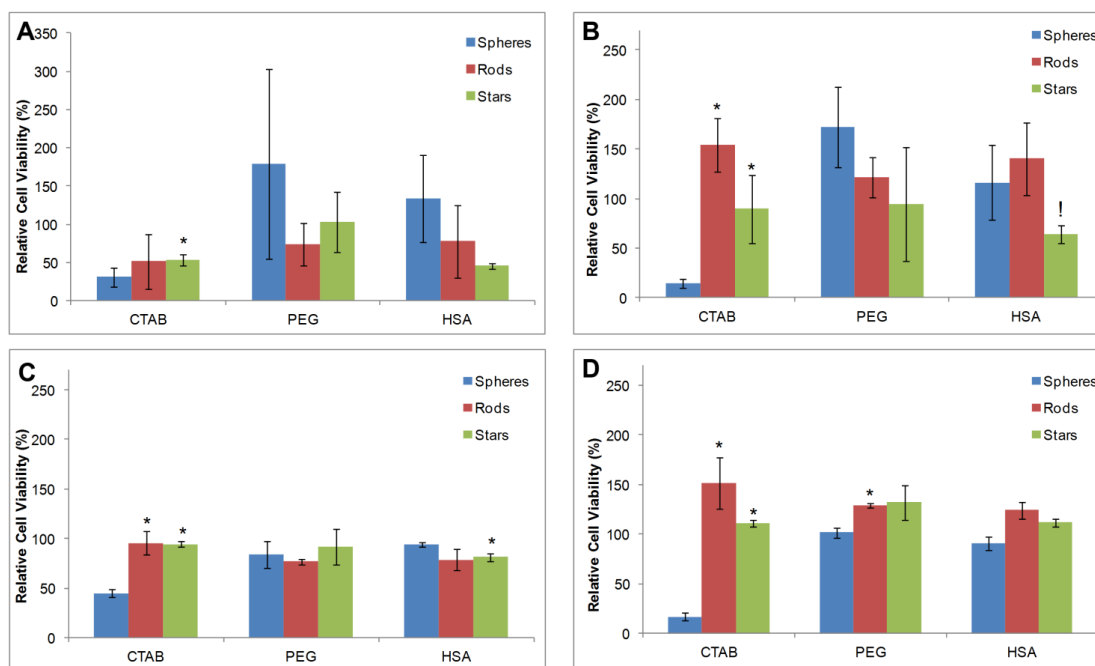


Figure 2.8 Viability data from the MTT cell proliferation assay after exposure to different AuNPs have been shown here. Plots show relative cell viabilities observed in A) U87 cells after 4 hours, B) U87 cells after 24 hours, C) fibroblasts after 4 hours and D) fibroblasts after 24 hours when exposed to different AuNPs. Percentage of viability was determined with respect to control. Error bars represent standard deviation with $n = 3$. Statistically significant difference * = from nanospheres within the same surface coating at that time point ($p < 0.05$), and ! = from nanorods within the same surface coating at that time point ($p < 0.05$).

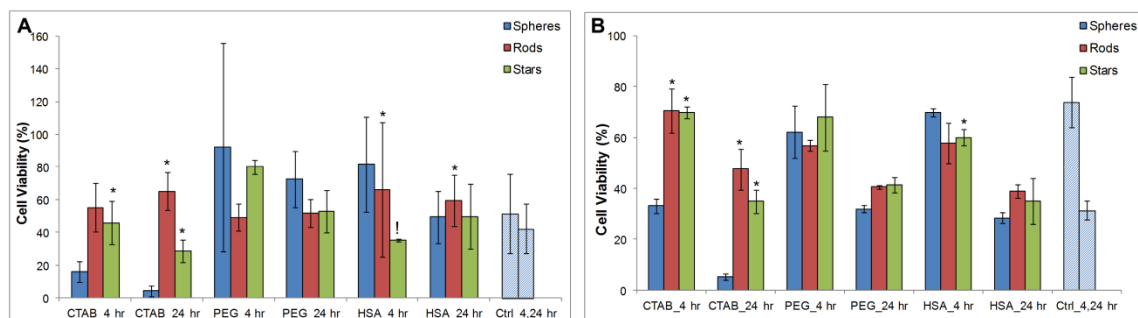


Figure 2.9 MTT assay data without normalization against controls show effective cell viability at 4 and 24 hours for U87 cells (A) and human dermal fibroblasts (B). Also reported are the viabilities at 4 and 24 hours for the control U87 cells and fibroblasts. This figure has been included in support of Figure 2.8, to explain the apparent higher cell

viability at 24 than 4 hours of incubation. In reality, by observing the viability of the control cells at 24 hours, especially for fibroblasts, one can determine that the control cells have low viabilities leading to the difference between sample and controls to be higher, leading to an apparent viability increase over time. In reality, the actual values are slightly lower at 24 hours when compared to 4 hours. Error bars represent standard deviation with $n = 3$. Statistically significant difference * = from nanospheres within the same surface coating at that time point ($p < 0.05$), and ! = from nanorods within the same surface coating at that time point ($p < 0.05$).

To further investigate the cytotoxicity induced by gold nanoparticles on U87 cells and fibroblasts, the LDH assay was carried out to measure the release of the enzyme lactate dehydrogenase (LDH) into the culture media and to provide information on cellular membrane disruption. Measuring LDH release can also provide information on necrosis since necrotic cell death is evaluated by determining damage of the cell membrane.⁽¹⁸⁾ Results from this assay were not normalized with respect to the untreated control cells in order to better highlight the differences in the response after exposure to NP in the two cell lines. **Figure 2.10** shows that, after 4 to 24 hour exposure to gold nanoparticles, the amount of LDH released was found to vary depending on the cell line, with only a mild LDH release observed in U87 cells and higher release levels in fibroblasts. However, the LDH release induced by CTAB NSp was found to be independent of the cell line used, likely because the presence of CTAB on spheres caused massive membrane disruption. Interestingly, in the presence of CTAB- and PEG-coated stars, the fibroblasts released a higher amount of LDH after 24 hours while the increase in incubation time had no effect on U87 cells. These results indicate that the presence of surface coatings on AuNPs like CTAB and PEG, together with the size and shape of the particles influences the viability and membrane integrity of fibroblasts. Overall, the higher membrane disruption observed in fibroblasts indicates that these cells might be undergoing cell death via necrosis.

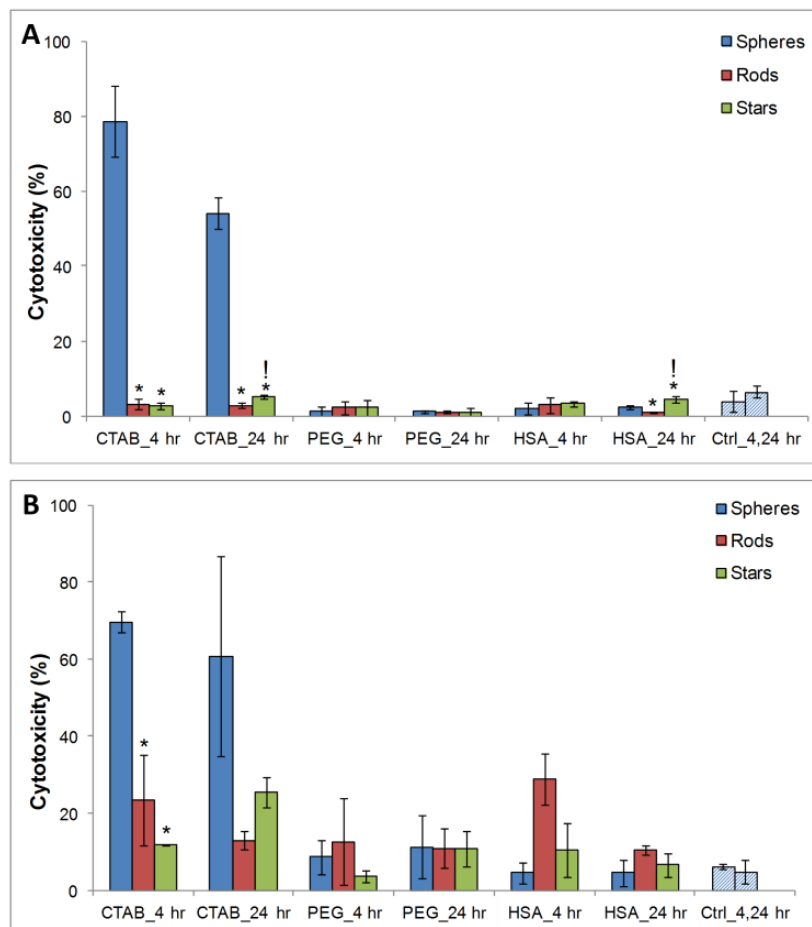


Figure 2.10 Cytotoxicity data from LDH (lactate dehydrogenate) assay have been shown here. Panels A and B show the toxicity observed after exposure to AuNPs for 4 and 24 hours in U87 cells and fibroblasts respectively. Control group represents untreated cells. Error bars represent standard deviation with $n = 3$. Statistically significant difference * = from nanospheres within the same surface coating at that time point ($p < 0.05$), and ! = from nanorods within the same surface coating at that time point ($p < 0.05$).

It has been hypothesized that nanoparticles induce toxicity in cells due to an increase in oxidative stress, which is a consequence of free radical formation. NPs have been known to generate reactive oxygen species (ROS), which then induce oxidative stress causing cellular inflammation initiating cell death either by apoptosis and necrosis.⁽¹⁹⁾ In order to monitor the oxidative stress generated in U87 and hfb cells, we measured the level of ROS generated using an ROS assay. **Figure 2.11**, panels A and B, shows the ROS

production in U87 cells and fibroblasts induced by different AuNPs after 4 and 24 hours. Assay results show that the ROS production is lower in U87 cells when compared to fibroblasts. It also increases in a time-dependent manner. Surprisingly, despite having the lowest cell viabilities, CTAB NSp had low ROS production in both cell lines indicating that the membrane damage seen by LDH assay was not due to free radical formation, but rather due to the interaction of CTAB with the phospholipid bilayer, as we previously observed.⁽²⁰⁾ On the other hand, CTAB AuNS showed high ROS production after 24 hours that was not observed in CTAB NSp and NR indicating that the size of CTAB-coated AuNP might play a role in ROS production. PEG- and HSA-coated spheres and stars also showed an increase in ROS production in both cells.

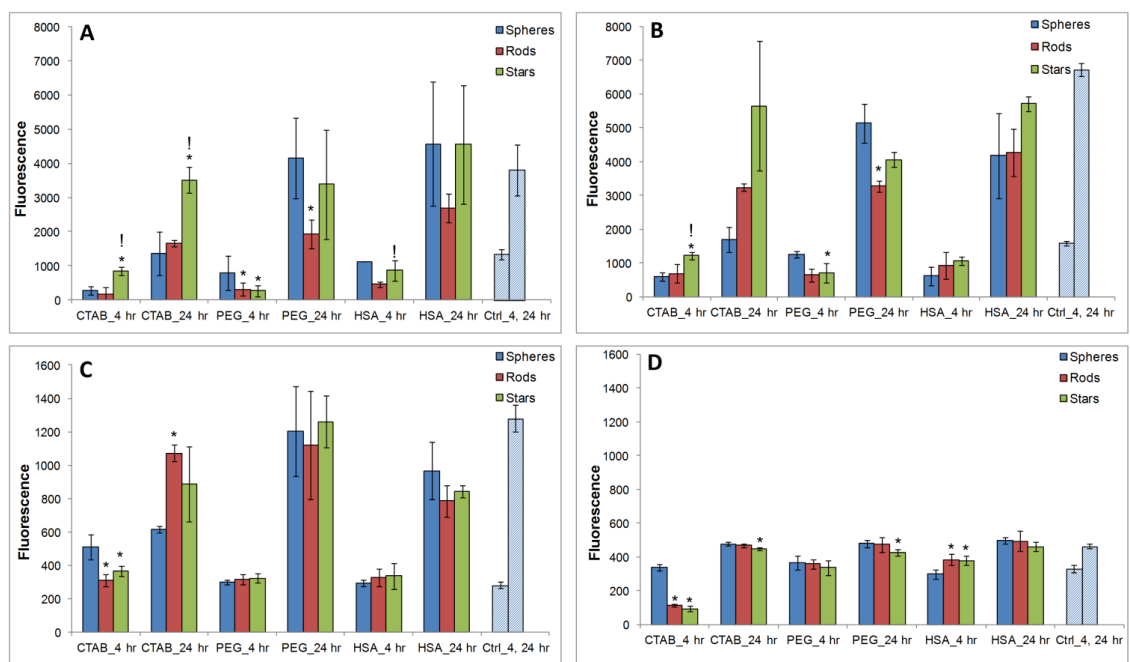


Figure 2.11 ROS production and caspase 3/7 activity observed in cells. Panels A and B show ROS production in U87 cells and fibroblasts respectively. Panels C and D show the caspase 3/7 activity seen in U87 and fibroblasts after exposure to different NP. Control represents untreated cells. Error bars represent standard deviation with n=3. Statistically significant difference * = from nanospheres within the same surface coating at that time

point ($p < 0.05$), and ! = from nanorods within the same surface coating at that time point ($p < 0.05$).

In addition to membrane damage and oxidative stress, NPs have also shown to cause organelle damage and apoptosis.⁽¹⁹⁾ In order to test whether either cell line undergoes apoptosis after exposure to AuNPs, the caspase 3/7 activity was measured using the fluorogenic substrate rhodamine 110 bis- (N-CBZ-L-aspartyl-L-glutamyl-L-valyl-aspartic acid amide), Z-DEVD-R11. **Figure 2.11** (Panels C and D) shows the caspase 3/7 activity of U87 cells and fibroblasts after 4 and 24 hours exposure to AuNPs. U87 cells showed an increase in intracellular caspase 3/7 activity after 24 hours with PEG coated particles having more activity than CTAB and HSA coating. These results indicate that U87 cells most likely undergo apoptosis after exposure to AuNPs. On the other hand, fibroblasts did not show an increase in caspase 3/7 activity after 24 hours indicating that they might be undergoing necrosis, in agreement to what was shown by the LDH assay.

2.4.4 Cellular uptake of AuNPs

To further understand the interaction of gold nanostars with cells we employed transmission electron microscopy (TEM) (**Figure 2.12**), to visualize the nanoparticles after internalization, and ICP-MS (**Figure 2.15**) to quantify the amount of gold taken up by the cells at various time points. TEM helped analyze the mechanism of AuNP uptake and determine nanoparticle localization inside the cells. The analysis was carried out only on U87 cells and fibroblasts exposed to PEG and HSA coated nanostars for 24 hours. The cells that were exposed to CTAB NS had very low cell viabilities after 24 hours and hence weren't processed for microscopy. TEM micrographs showed that the nanostars were easily detectable within the cells and they retained their shape upon cellular uptake,

which is extremely important for SERS tag activity retention after long incubation times *in vitro* or circulation and biodistribution *in vivo*. Both PEG- and HSA-stabilized nanostars were found to be internalized in U87 cells and fibroblasts after 24 hours. No particles were detected inside the nucleus; however, many HSA-capped nanostars were found to be localized in the perinuclear region in fibroblasts. More PEG-coated nanostars than HSA-NS were found inside U87 cells, as confirmed by ICP-MS, while the opposite was observed for fibroblasts. In both cell lines, the majority of the particles were found to be localized in vesicles of different sizes with very few particles observed in the cytosol. This was observed for both NP types and indicates an uptake predominantly by endocytosis. U87 cells showed significant plasma membrane damage, chromatin condensation at the periphery of the nucleus, increased vacuole formation (which indicates autophagy), and apoptotic bodies. All these changes in the cell are indicative of cell death via apoptosis (**Figure 2.13**) and confirmed the results obtained with the assays previously described. On the other hand, fibroblasts showed extensive mitochondrial damage and damage to the cell membrane (**Figure 2.14**) indicative of cell death via necrosis.

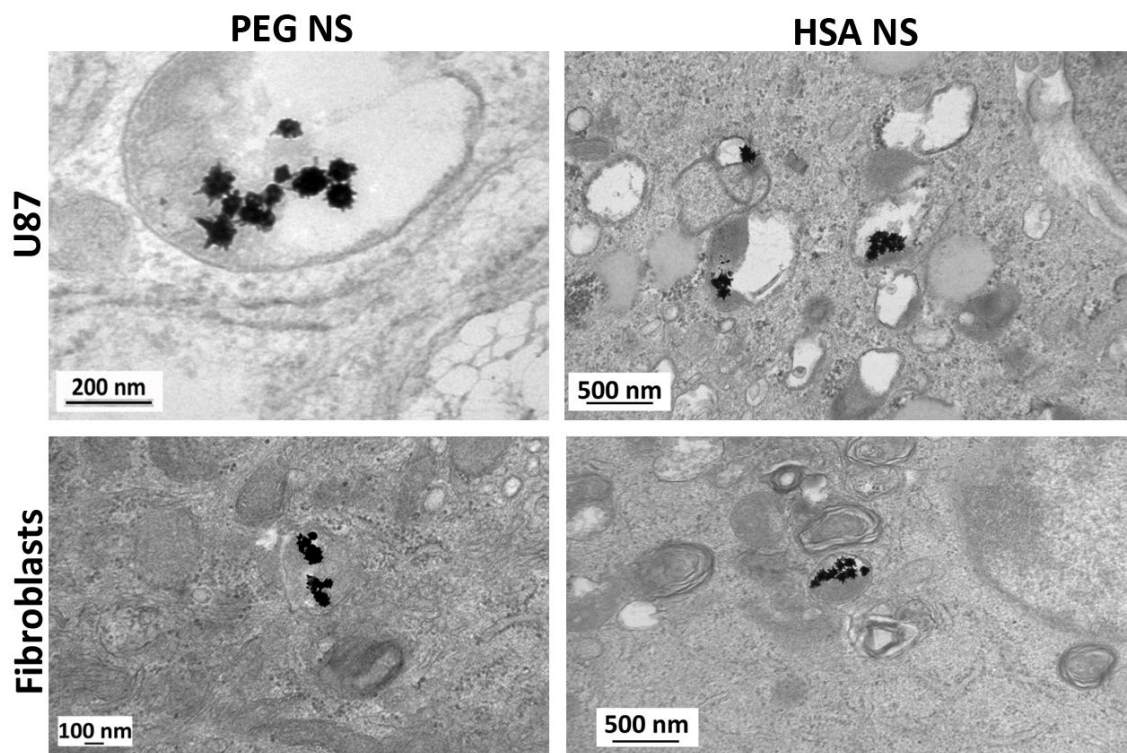


Figure 2.12 Transmission electron micrographs aid in the localization of nanoparticles inside cells. In both U87 cells (top) and fibroblasts (bottom), the NPs were primarily found inside membrane-bound vesicles, suggesting an uptake mechanism mediated by endocytosis.

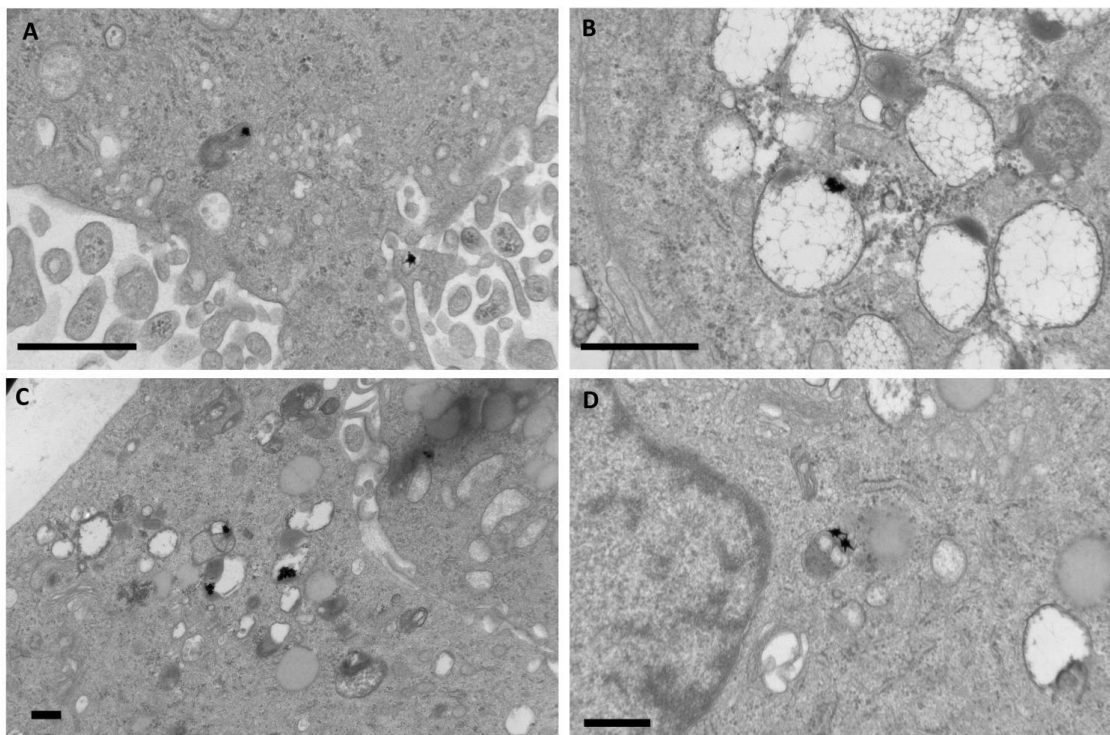


Figure 2.13 Figures show damage observed in U87 cells after exposure to HSA nanostars. Panels show A) formation of apoptotic bodies and damage to cell membrane, B) and C) presence of large number of vacuoles indicating autophagy of cell organelles and, D) condensation of chromatin at the periphery of the nucleus. All these changes in the U87 cells indicate possible death via apoptosis. Scale bars in all panels are 500 nm.

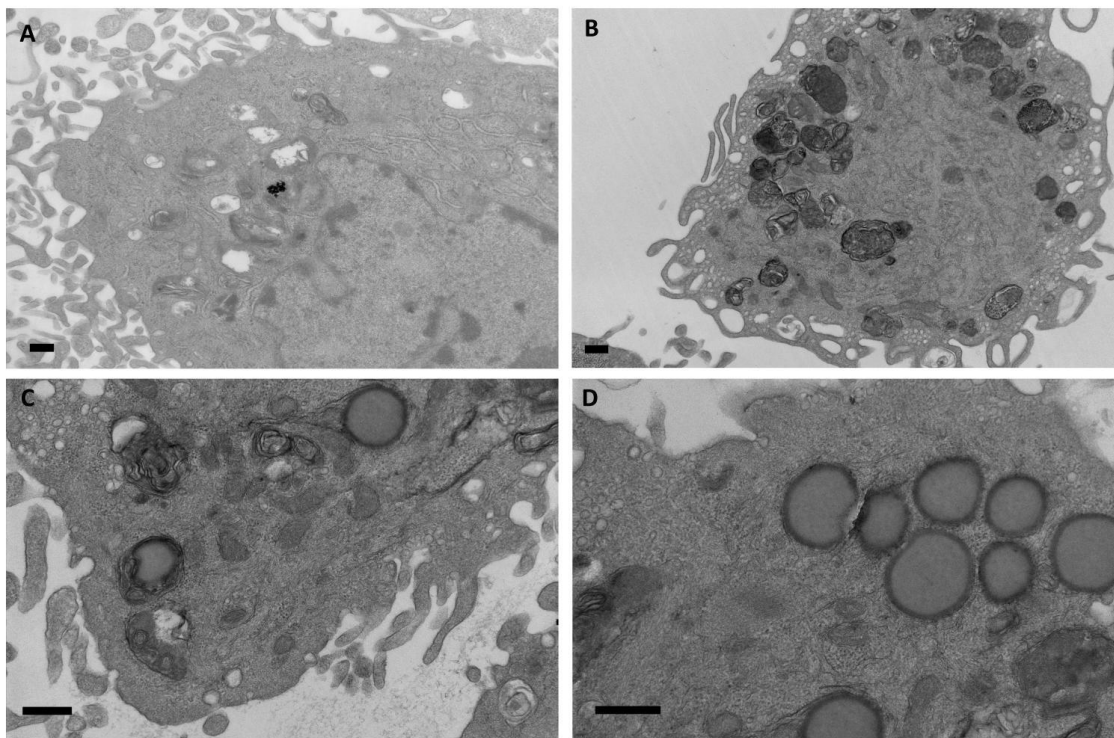


Figure 2.14 Figures show damage observed in fibroblasts after exposure to PEG and HSA nanostars. Panels show A) damage to cell membrane, B), C) and D) show mitochondrial damage and changes to the cell membrane. All these changes in fibroblasts indicate possible death via necrosis. Scale bars in all panels are 500 nm.

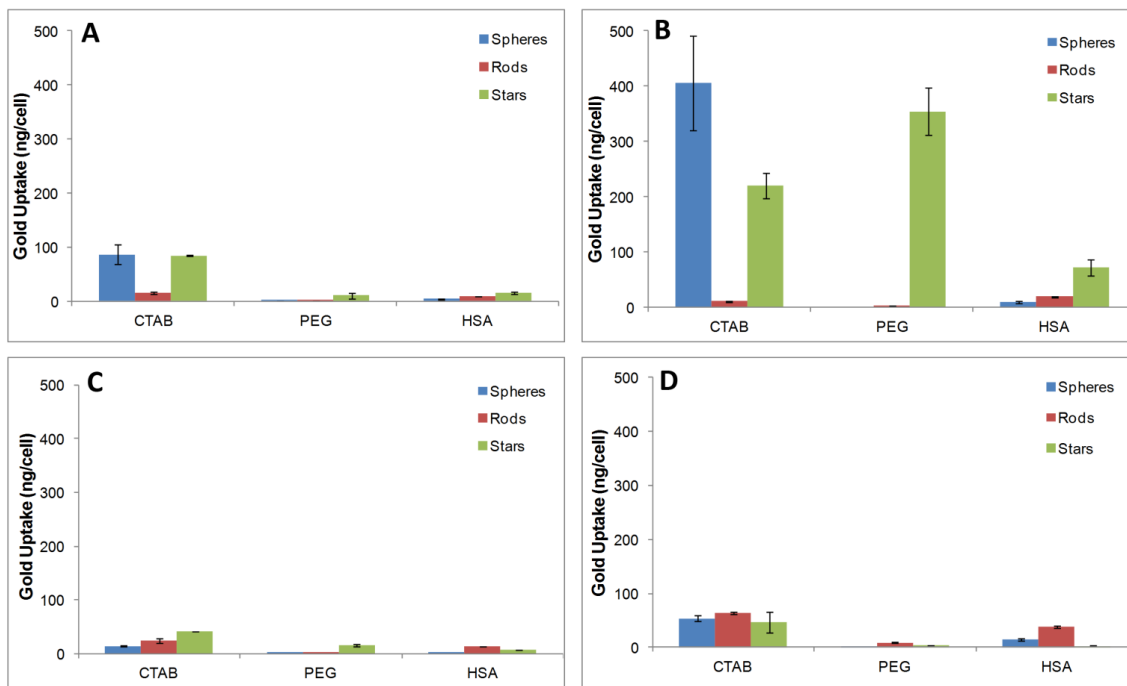


Figure 2.15 AuNP uptake (ng of gold per cell) measured using ICP-MS. Figure panels show uptake after A) 4 hours in U87 cells, B) 24 hours in U87 cells, C) 4 hours in fibroblasts, and D) 24 hours in fibroblasts. Error bars represent standard deviation, with $n=3$.

Results from ICP-MS showed higher gold uptake in U87 cells when compared to fibroblasts: cellular uptake was less than 100 ng of gold per cell for all the NP groups in fibroblasts while much higher uptakes (nearly 500 ng of gold per cell) were observed in U87 cells. High uptake rates were observed in nanostars and among them, the amount of gold taken up varied depending on the surface chemistry. However, the higher uptake did not compromise cell viabilities, as seen in **Figure 2.16**, and no clear correlation could be established between cellular uptake and cytotoxicity values, as previously reported. ⁽⁸⁾ Cellular viabilities were found to be identical to the untreated control group suggesting that the dosage of nanoparticles did not affect viabilities at these loading amounts.

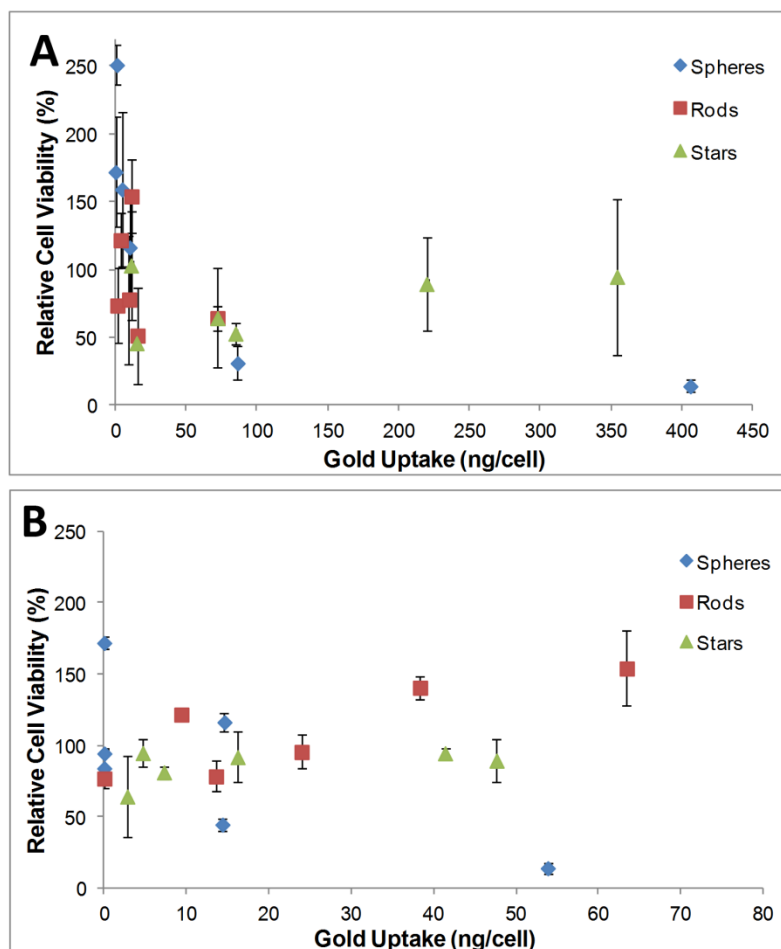


Figure 2.16 Relationship between cell viability and AuNP uptake. Cell viabilities have been measured with respect to the controls. Figure panels show viabilities seen in A) U87 cells, and B) fibroblasts. Error bars represent standard deviation with $n=3$ samples.

2.5 Conclusion

In summary, the surface chemistry of gold nanoparticles has been shown to most drastically affect cell viability for both healthy and diseased cells; in particular, the presence of CTAB on the surface of gold nanoparticles reduced the viability as shown by MTT assays and caused membrane damage as demonstrated by LDH assays in both the human glioblastoma (U87) and fibroblast cell lines. Cytotoxicity evaluations via MTT assay also demonstrated that there could be differences in the biological response

due to particle shape in CTAB coated NPs while PEG and HSA coated NPs did not seem to have any shape related effects, perhaps due to the higher thickness of the capping layer which masks any morphological differences. Results obtained by LDH assays suggest that the cell line U87 might be more resistant to AuNPs-induced toxicity as compared to fibroblasts, and that most likely fibroblasts undergo NP-induced necrosis, as opposed to what was observed in U87 cells. The mechanism by which nanoparticles induce toxicity in cells differs dramatically from its corresponding bulk material. It has been hypothesized that AuNPs induce toxicity due to an increase in ROS production and hence oxidative stress, which causes mitochondrial membrane damage and electron chain dysfunction, which in turn leads to cell death. However, despite having low viabilities in CTAB-NSp exposed cells, the ROS production was lower when compared to CTAB NS and NR. A possible explanation for the cytotoxicity observed in NSp could be due to their higher surface-to-volume ratio and therefore higher release of toxic CTAB upon intracellular aggregation.⁽²¹⁾ The higher viabilities observed in PEG coated AuNPs could be due to the fact that most of the nanoparticles are taken up by the cells in membrane-bound vesicles indicating an uptake mechanism predominantly by endocytosis. This would lead to limited interaction of the NPs with organelles (like mitochondria) and the nucleus and thus reduced toxicity. TEM and ICP-MS data revealed that more PEG-coated NS were taken up by U87 cells, while HSA-coated NS were taken up by fibroblasts. We also observed a difference in the mechanism of cell death based on the cell line used. Caspase 3/7 activity and LDH assays showed that U87 cells were undergoing apoptosis while fibroblasts were undergoing cell death via necrosis when exposed to

nanoparticles. Overall, this study demonstrates that gold nanostars can be effectively taken up by both healthy and diseased cells without inducing significant toxicity when capped by a suitable ligand such as PEG, and can be therefore be considered as a safe nanostructured platform upon which to build efficient contrast agents for imaging applications.

2.6 Acknowledgments

We thank Prof. Prabhas Moghe for the use of his cell culture facility and for gifting us the cells and Supriya Atta for help with NMR.

2.7 References

- (1) Le Ouay, B., and Stellacci, F. (2015) Antibacterial activity of silver nanoparticles: A surface science insight. *Nano Today* 10, 339-354.
- (2) Alvarez-Puebla, R. A., and Liz-Marzan, L. M. (2010) SERS-based diagnosis and biodetection. *Small* 6, 604-610.
- (3) Andreou, C., Kishore, S. A., and Kircher, M. F. (2015) Surface-Enhanced Raman Spectroscopy: A New Modality for Cancer Imaging. *J Nucl Med.* 56, 1295-1299.
- (4) Lane, L. A., Qian, X., and Nie, S. (2015) SERS Nanoparticles in Medicine: From Label-Free Detection to Spectroscopic Tagging. *Chem Rev.* 115, 10489-10529.
- (5) Fabris, L. (2016) SERS Tags: The Next Promising Tool for Personalized Cancer Detection? *Chem Nano Mat* 2, 249-258.
- (6) Indrasekara, A. S. D. S., Meyers, S., Shubeita, S., Feldman, L. C., Gustafsson, T., and Fabris, L. (2014) Gold nanostar substrates for SERS-based chemical sensing in the femtomolar regime. *Nanoscale* 6, 8891-8899.
- (7) Alkilany, A. M., and Murphy, C. J. (2010) Toxicity and cellular uptake of gold nanoparticles: what we have learned so far? *J Nanopart Res.* 12, 2313-2333.
- (8) Naha, P. C., Chhour, P., and Cormode, D. P. (2015) Systematic *in vitro* toxicological screening of gold nanoparticles designed for nanomedicine applications. *Toxicol In Vitro* 29, 1445-1453.
- (9) Frens, G. (1973) Controlled nucleation for regulation of particle-size in monodisperse gold suspensions. *Nature-Phys Sci.* 241, 20-22.
- (10) Nikoobakht, B., and El-Sayed, M. A. (2003) Preparation and Growth Mechanism of Gold Nanorods (NRs) Using Seed-Mediated Growth Method. *Chem.Mater.* 15, 1957-1962.
- (11) Yuan, H., Khoury, C. G., Hwang, H., Wilson, C. M., Grant, G. A., and Vo-Dinh, T. (2012) Gold nanostars: surfactant-free synthesis, 3D modelling, and two-photon photoluminescence imaging. *Nanotechnology* 23, 075102.
- (12) Maier, S. A. (2007) *Plasmonics: Fundamentals and Applications*, 1 ed., Springer US.
- (13) Liu, H., Pierre-Pierre, N., and Huo, Q. (2012) Dynamic light scattering for gold nanorod size characterization and study of nanorod-protein interactions. *Gold Bull.* 45, 187-195.
- (14) Stiufiuc, R., Iacovita, C., Nicoara, R., Stiufiuc, G., Florea, A., Achim, M., and Lucaciu, C. M. (2013) One-Step Synthesis of PEGylated Gold Nanoparticles with Tunable Surface Charge. *J Nanomater.* 2013, 7.
- (15) Brandenberger, C., Muhlfeld, C., Ali, Z., Lenz, A. G., Schmid, O., Parak, W. J., Gehr, P., and Rothen-Rutishauser, B. (2010) Quantitative evaluation of cellular uptake and trafficking of plain and polyethylene glycol-coated gold nanoparticles. *Small* 6, 1669-78.
- (16) Yeh, P.-R., and Tseng, W.-L. (2012) Human serum albumin-coated gold nanoparticles for selective extraction of lysozyme from real-world samples prior to capillary electrophoresis. *J Chromatogr A* 1268, 166-172.
- (17) Manson, J., Kumar, D., Meenan, B. J., and Dixon, D. (2011) Polyethylene glycol functionalized gold nanoparticles: the influence of capping density on stability in various media. *Gold Bull.* 44, 99-105.

- (18) Chan, F. K., Moriwaki, K., and De Rosa, M. J. (2013) Detection of necrosis by release of lactate dehydrogenase activity. *Methods Mol Biol.* 979, 65-70.
- (19) Manke, A., Wang, L., and Rojanasakul, Y. (2013) Mechanisms of nanoparticle-induced oxidative stress and toxicity. *BioMed Res. Int.* 2013, 942916.
- (20) Schachter, D. (2013) in *Biomedical Engineering* pp 71, Rutgers-The State University of New Jersey, New Brunswick, ProQuest Dissertations And Theses.
- (21) Tarantola, M., Pietuch, A., Schneider, D., Rother, J., Sunnick, E., Rosman, C., Pierrat, S., Sonnichsen, C., Wegener, J., and Janshoff, A. (2011) Toxicity of gold-nanoparticles: synergistic effects of shape and surface functionalization on micromotility of epithelial cells. *Nanotoxicology* 5, 254-268.
- (22) Cleland, W. W. (1964) Dithiothreitol, a New Protective Reagent for Sh Groups. *Biochemistry* 3, 480-482.
- (23) Liu, K., Zheng, Y., Lu, X., Thai, T., Lee, N. A., Bach, U., and Gooding, J. J. (2015) Biocompatible Gold Nanorods: One-Step Surface Functionalization, Highly Colloidal Stability, and Low Cytotoxicity. *Langmuir* 31, 4973-4980.
- (24) Liu, X., Atwater, M., Wang, J., and Huo, Q. (2007) Extinction coefficient of gold nanoparticles with different sizes and different capping ligands. *Colloids Surf Biointerfaces.* 58, 3-7.

**CHAPTER 3 SERS-BASED QUANTIFICATION OF BIOMARKER
EXPRESSION AT THE SINGLE CELL LEVEL ENABLED BY GOLD
NANOSTARS AND TRUNCATED APTAMERS**

Note: This chapter is currently under review for the following publication in Bioconjugate Chemistry.

Manjari Bhamidipati, Hyeon-Yeol Cho, Ki-Bum Lee and Laura Fabris. “SERS-based quantification of biomarker expression at the single cell level enabled by gold nanostars and truncated aptamers”.

3.1 Abstract

Surface-enhanced Raman spectroscopy (SERS)-based biosensors have been used increasingly over the past few years for cancer detection and diagnosis. SERS-based imaging offers excellent sensitivity and has advantages over other detection techniques such as fluorescence. In this study, we developed a novel biosensor to detect the cancer biomarker epithelial cell adhesion molecule (EpCAM) and quantify its expression at the single cell level. EpCAM is one of the most commonly expressed markers on a variety of cancer cells; importantly it has been suggested that reduction of its expression levels could be associated to the epithelial to mesenchymal transition (EMT), and thus to the onset of metastasis. Therefore, monitoring variations in expression levels of this membrane biomarker would improve our ability to monitor cancer progression. The described substrate-based biosensor was developed employing gold nanostars functionalized with EpCAM aptamer molecules and was able to quantify sub-nanomolar concentrations of EpCAM protein in solution. Importantly, we demonstrated its use to quantify EpCAM expression on the surface of two cancer cells, MCF-7 and PC-3. We also compared the binding efficiency of two EpCAM DNA aptamers of different lengths and observed a substantial improvement in the sensitivity of detection employing the shorter aptamer sequence, probably due to the reduced number of conformations possible at room temperature with the truncated oligonucleotide. Detailed characterization of the substrates was carried out using both SERS maps and atomic force microscopy. These substrate-based diagnostic devices promise to be relevant for monitoring phenotype evolutions in cancer cells, blood, and other bodily fluids, thus improving our ability to follow in real time disease onset and progression.

3.2 Introduction

Early detection of cancer has shown promise for a reduction in cancer-related mortality and improvement of therapeutic outcomes.¹ A variety of cancer biomarkers such as proteins, nucleic acids, small metabolites, as well as tumor cells offer valuable insight on cancer progression.² Among these biomarkers, the epithelial cell adhesion molecule (EpCAM) is one of the most abundantly used markers for detecting a broad variety of cancers such as colon, gastric, prostate, ovarian, lung, and breast.^{3, 4} Changes in the expression of EpCAM have been associated with the onset of metastasis.⁵ However, the detection of variations in EpCAM expression with high sensitivity and selectivity remains challenging.

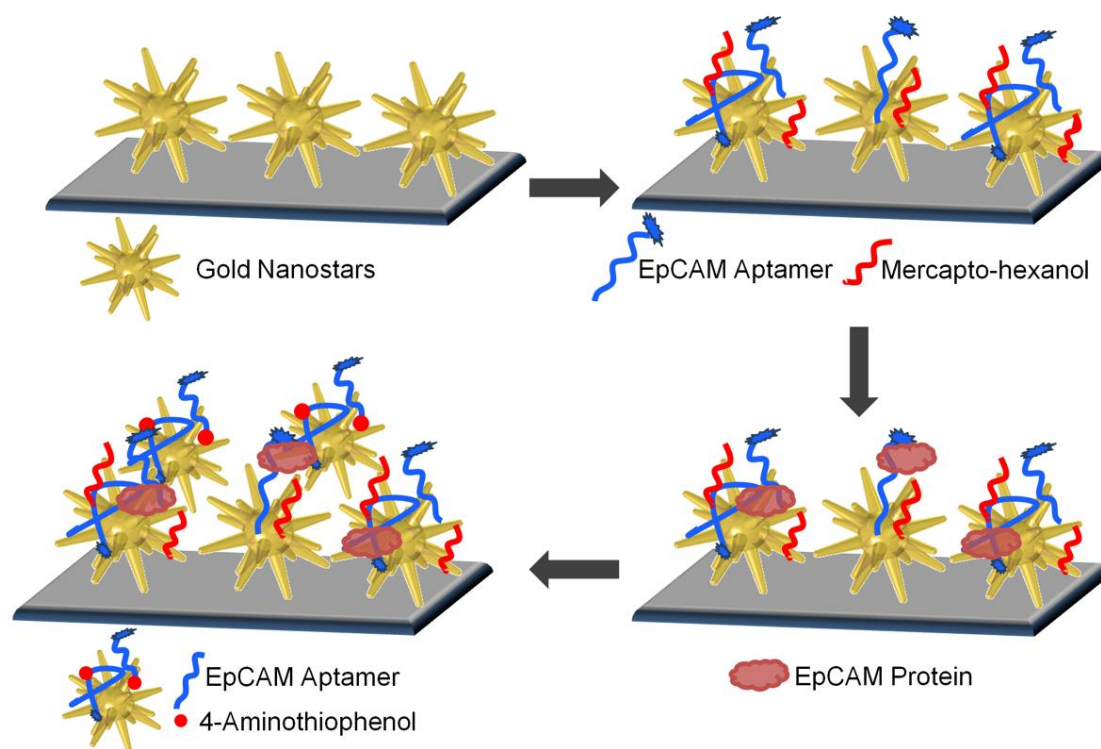
SERS is an ultrasensitive vibrational spectroscopic technique that has been used for biosensing and diagnostics.⁶ SERS-based imaging offers the advantages of narrow Raman peak width with no spectral overlap, minimal photobleaching, effective multiplexing, and has been shown to outperform fluorescence.⁷ SERS-based approaches employing tags have recently demonstrated to be powerful tools for effective identification of tumor margins *in vivo* and improved tumor excision in murine models of glioblastoma and breast cancer.^{8, 9} SERS tags are composed of a plasmonic nanoparticle (NP) like gold, Raman reporter molecules, and targeting moieties such as antibodies, peptides, and aptamers. The presence of the reporter near the plasmonic nanoparticle greatly enhances its Raman signal. The shape of the NP influences its optical properties and hence the brightness of the tag; in particular, nanoparticles presenting edges and corners have been shown to lead to the highest near-field enhancements and thus to the highest sensitivities.⁷ Gold nanostars, particularly, have shown excellent enhancement

factors with ultra-sensitivity that can enable single molecule detection.¹⁰ The highly specific recognition enabled by SERS tags is provided via the use of aptamers or antibodies. Aptamers are a new class of targeting moieties, and are single-stranded DNA or RNA molecules isolated through SELEX (Systematic Evolution of Ligands by Exponential enrichment).^{11, 12} They offer advantages of low immunogenicity, high stability, and rapid tissue penetration, and have demonstrated potential as powerful tools for cancer cell identification due to their ease of synthesis and manipulation and their ability to target a wide range of biomarkers.¹³⁻¹⁵

In this study, we developed a SERS-based biosensor, comprising gold nanostars and EpCAM aptamers that enabled us to detect small changes in the concentration of soluble EpCAM protein and in the expression of EpCAM in individual cancer cells with high sensitivity and selectivity. For this purpose, we initially used a 48 base pair (bp) EpCAM DNA aptamer, SYL3C, that was developed by Song *et al.*¹⁶ for a variety of cancer cells expressing EpCAM on their surface. The biosensor was developed by functionalizing substrates with gold nanostars and EpCAM aptamer molecules. Varying concentrations of EpCAM protein were added and their SERS response was measured by adding SERS tags consisting of a Raman reporter (4-aminothiophenol, 4-ATP) and the EpCAM aptamer in a sandwich fashion. Detailed characterization of the substrates was carried out using SERS maps, atomic force microscopy (AFM), and scanning electron microscopy (SEM). SERS tags were characterized using dynamic light scattering (DLS), zeta potential, and transmission electron microscopy (TEM). In order to improve the sensitivity of the assay, the substrates were also tested with a shorter 17-bp EpCAM aptamer, EpA, developed by Macdonald *et al.*, which was suggested to provide improved

target recognition and binding.¹⁷ The substrates with the shorter aptamer were characterized in a similar manner. Most of the aptamers against cancer biomarkers are developed in cells and are used to detect membrane-embedded biomarkers. Furthermore, due to the substantially more limited application of aptamers in bioassays or cell studies, a significantly lower pool of aptamers is available on the market for the development of suitable assays for early disease detection. Thus, we were interested in determining whether these aptamers could be used to detect both soluble and membrane-embedded proteins. Membrane-embedded protein markers, because of their position across the phospholipid bilayer, necessarily possess an epitope presentation that is different from that of their soluble counterparts, thus the use of aptamers developed via cell-SELEX to detect soluble proteins might not necessarily lead to the sensitive detection of soluble EpCAM (and vice versa). For these reasons, we wanted to first assess the effectiveness of this cell-based EpCAM aptamer for the detection of low concentrations of soluble EpCAM proteins in solution. Upon verification that changes in epitope presentation due to steric hindrance and/or interactions with the surrounding environment do not substantially alter aptamer-target recognition and binding, we employed the assay to detect and capture cancer cells with varying EpCAM expression levels. Because steric hindrance (i.e. protein density and/or clustering on the cell membrane) appears not to affect recognition, we hypothesized that the aptamer-EpCAM binding affinity is not altered among cells with low or high expression levels hence enabling us to quantify the expression levels of this biomarker in individual cells regardless of their EpCAM expression levels. Capturing cells on substrates and quantifying the biomarker expression has potential implications for use in enrichment of circulating tumor cells,

exosome analysis, and personalized cancer treatment. Furthermore, it promises to be effective in the identification of outliers in populations of cells whose phenotype alterations might not be detectable with population-level techniques such as flow cytometry but might be important sentinels for early disease detection.



Scheme 3.1 Schematic representation of the sequence of steps followed to carry out the assay. Glass substrates, gold nanostars, EpCAM aptamer, mercaptohexanol, EpCAM protein, and 4-aminothiophenol not drawn to scale.

3.3 Experimental Methods

3.3.1 Nanoparticle Synthesis

Gold nanostars were synthesized according to a modified version of the surfactant-free nanostar synthesis described by Yuan *et al.*¹⁸ Briefly, 2 mL of HAuCl₄ salt solution (0.025 M) and 200 μ L of 1 N HCl were added to 48 mL of Milli-Q water. A total of 125 μ L of 12 nm citrate-capped spheres ($A=2.81$) was then added to the mixture and mixed thoroughly by stirring. Then, 1 mL of 100 mM ascorbic acid and 2 mL of 3 mM AgNO₃ were simultaneously added to the above mixture. The reaction was carried out for 7 min under gentle stirring and then purified by centrifugation at 4000 g for 10 min.

3.3.2 Preparation of SERS tags

The thiolated EpCAM aptamer SYL3C (48-bp) developed by Song *et al.*¹⁶ [5'-HS-(CH₂)₆-CAC TAC AGA GGT TGC GTC TGT CCC ACG TTG TCA TGG GGG GTT GGC CTG-Rhodamine Red-3', Integrated DNA Technologies Inc.] was dissolved at 1 μ M concentration in binding buffer (1X PBS, pH 7.4 with 4.5 g/L glucose and 5 mM MgCl₂) and treated with 50 mM Tris(2-carboxyethyl) phosphine hydrochloride (TCEP; Sigma-Aldrich) solution for 30 minutes at room temperature to eliminate disulfide bonds. A truncated SYL3C aptamer sequence (17-bp), EpA [5'-HS-(CH₂)₆-ACA GAG GTT GCG TCT GT-6-FAM-3', Integrated DNA Technologies Inc.], developed by Macdonald *et al.*¹⁷, was also tested. For the preparation of SERS tags, the gold nanostars synthesized above were allowed to react for additional 30 minutes with 1 mL of 50 mM solution of 4-aminothiophenol (Sigma-Aldrich). The nanoparticles were washed twice in water and re-suspended at a final concentration of 3 nM in 1X PBS. 500 μ L of the 3 nM nanostars

were then allowed to react with 100 μL of 2 mg/mL sulfo-SMCC (Thermo Fisher) for 30 minutes. The nanoparticles were washed thoroughly and re-suspended in 500 μL of 1X PBS. To this, 1 μM final concentration of EpCAM aptamer was added and allowed to react for 30 minutes. The SERS tags were washed twice and re-suspended in the binding buffer.

3.3.3 Substrate Preparation

Glass microscope slides (Fisher Scientific; Plain microscope slides) were cut into approximately 0.5 cm x 1 cm sized substrates. They were rinsed thoroughly and sonicated for a few minutes in acetone and Milli-Q water. Following this step, they were immersed in a 2% solution of 3-aminopropyltriethoxysilane (APTES) for 20 minutes at room temperature. Afterwards, they were placed in an oven set to 110°C for 1 hour. The substrates were then immersed in a 0.3% solution of bovine serum albumin (BSA) for 1 hour following which they were washed thoroughly with Milli-Q water and left to dry overnight.

3.3.4 Surface Functionalization

The APTES functionalized substrates were incubated with a 3 nM gold nanostar solution for 1 hour under gentle stirring. They were washed three times with Milli-Q water. Subsequently, the thiolated EpCAM aptamer at 1 μM concentration was deposited on the substrates and allowed to bind overnight. The substrates were then washed three times with Milli-Q water and incubated in a 1 mM 50% ethanolic solution of 6-mercaptohexanol (MCH) for 1 hour. They were then washed three times with water and incubated with 40 μL of the desired concentration (10 pM to 3 μM concentration,

prepared in binding buffer) of EpCAM protein (Thermo Fisher) for 1 hour. They were then washed thoroughly and allowed to react with SERS tags for 1 hour. The substrates were washed thoroughly to remove any unbound tags and allowed to dry before analyzing their SERS activity. The same procedure was repeated with BSA and fibrinogen as control proteins.

3.3.5 Characterization of NPs and SERS tags

The UV-Vis spectra were recorded on an SI Photonics Model 440 spectrophotometer. The morphology of nanostars and SERS tags was evaluated using a Philips CM12 transmission electron microscope and the size information was extracted using the Image J software. DLS and zeta potential measurements were performed using a Malvern Zetasizer Nano-ZS instrument. Three sequential measurements were performed for the experiments using water and 1X PBS diluent parameters with flow cell configuration. The zeta potential data were fit using Smoluchowski's theory.

3.3.6 Substrate Characterization

Non-contact mode AFM measurements were carried out with a Park systems NX10 AFM using non-contact cantilever (PPP-NCHR, Park Systems) that had a force constant of 42 N/m (specific range: 10-130) and a resonant frequency of 330 kHz (specific range: 204-497). Scanning electron microscopy (SEM) images were collected using a Zeiss Sigma Field Emission SEM (Model 8100). All SERS measurements were carried out using a Renishaw in Via Raman microscope. The spectra were obtained with a 785 nm diode laser at a laser power of 0.17 mW using a data acquisition time of 10 s, single accumulation under a 50x objective. For each of the substrates, three maps of $5 \times 5 \mu\text{m}^2$

sized areas were chosen at random places of the sample. The areas were raster-scanned with a 1 μm step size. The final SERS spectra shown are averages of the three maps obtained. The intensity of a Si peak at 521 cm^{-1} was used as an internal reference.

3.3.7 Cell Culture

In this work, prostate cancer cells, PC-3, and breast cancer cells, MCF-7 were used as the target cell lines. Cervical cancer cells, HeLa, were used as an EpCAM-negative cell line. PC-3 cells were cultured in RPMI 1640 Media (Sigma-Aldrich) that was supplemented with 10% Fetal Bovine Serum (Gibco, Thermo Fisher Scientific) while MCF-7 cells and HeLa cells were cultured in Dulbecco's modified Eagle medium (Sigma) that was supplemented with 10% (v/v) Fetal Bovine Serum and 1% (v/v) penicillin-streptomycin (Thermo Fisher). Cells were grown at 37°C with 5% CO_2 . After reaching 70-80% confluency, the cells were trypsinized and re-suspended in fresh media. For substrate capture experiments, the appropriate number of cells were counted and re-suspended in 50 μL of 1X PBS and loaded onto the cell-capture substrates. After incubation at 37°C for 1 hour, the substrates were washed gently with 1X PBS. The captured cells were then allowed to react with SERS tags for another 1 hour at 37°C . The substrates were then washed thoroughly to remove unbound tags and fixed with 4% paraformaldehyde in PBS for 10 mins. The captured cells on the substrate were then counted manually and detected by SERS measurements.

3.3.8 Flow Cytometry

After reaching 70-80% confluency, the three cell lines were dissociated with trypsin, washed and re-suspended in 1X PBS. They were then stained with anti-human

EpCAM/TROP-1 PE conjugated antibody (R&D Systems) for 30 minutes at room temperature in dark. Controls for the experiment contained unstained cells and isotype control cells that were stained with mouse IgG2B PE-conjugated antibody (R&D Systems). FACS analysis on the samples was carried out using a Beckman Coulter Gallios Flow Cytometry instrument and the results were analyzed using Kaluza software.

3.4 Results and Discussion

3.4.1 NP and SERS tags synthesis

Gold nanostars were synthesized according to a modified version of the reported surfactant-free nanostar synthesis method¹⁸ and were characterized by a localized surface plasmon resonance (LSPR) band centered at 745 nm. The morphology and size of all the particles were verified using TEM, as seen in **Figure 1**. TEM micrographs (**Figures 3.1 panels A and B**) showed that the nanostars possessed a spherical core with a large number of sharp protruding spikes. The average tip-to-tip distance was measured to be 100.4 ± 24.4 nm.

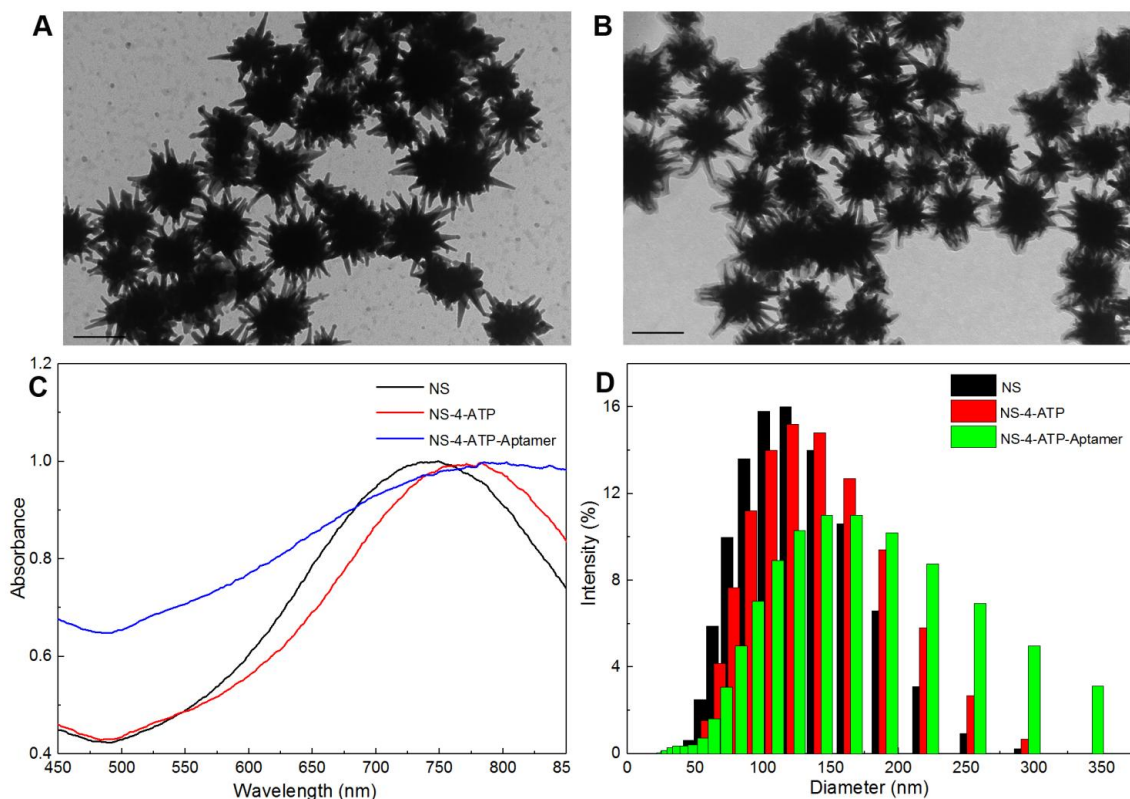


Figure 3.1 Assessment of nanostar properties and functionalization was carried out with multiple techniques. Figures 3.1 (A) and 1 (B) show transmission electron (TEM) micrographs of (A) as synthesized gold nanostars, and (B) nanostars functionalized with 4-aminothiophenol and EpCAM aptamer. Scale bars are 100 nm. Figure 3.1(C) shows the UV-visible spectra of as-synthesized gold nanostars, 4-ATP-coated nanostars, and 4-ATP- and EpCAM aptamer-coated nanostars. Figure 3.1(D) shows the relative dynamic light scattering (DLS) data, which provide size distributions in Milli-Q water at room temperature of as-synthesized nanostars, nanostars functionalized with 4-ATP, and with 4-ATP and EpCAM aptamer.

The nanostars were then functionalized with 4-aminothiophenol (4-ATP) and the thiolated EpCAM aptamer via coupling reactions mediated by sulfo-SMCC (succinimidyl 4-[N-maleimidomethyl] cyclohexane-1-carboxylate). Sulfo-SMCC is a heterobifunctional crosslinker that contains N-hydroxysuccinimide (NHS-ester) and maleimide groups that allow covalent conjugation to amine and sulfhydryl-containing molecules. The NHS-ester reacts with the primary amine of 4-ATP to form an amide bond while the maleimide

reacts with the thiol group on the EpCAM aptamer to form a stable thioether bond. TEM micrographs of the functionalized nanostars show that the sharp morphology of the particle is retained, thus ensuring that they will still be viable as SERS enhancing platforms (**Figure 3.1B**).

After surface functionalization, the nanostars showed an increase in size and a slight red shift in the LSPR position (**Figure 3.1C**). Because the position of the LSPR is dependent on the dielectric function of the attached ligand,¹⁹ a shift indicates successful surface functionalization. In UV-vis spectroscopy experiments, the surfactant-free nanostars showed an LSPR around 745 nm that red-shifted to 773 nm upon addition of 4-ATP. Addition of the thiolated EpCAM aptamer caused a further red-shift to 787 nm. Furthermore, TEM micrographs shown in **Figure 3.1B** revealed an increase in the average size of the nanostars from 100.4 ± 24.4 nm (surfactant free stars) to 123.1 ± 16.3 nm for 4-ATP-EpCAM aptamer coated stars. This increase of 22.7 nm is consistent with the expected size contribution of the added 4-ATP reporter, SMCC, and the 48 bp EpCAM aptamer with its hairpin structure. In addition, dynamic light scattering (DLS) results (**Figure 3.1D**) also showed an increase in the hydrodynamic diameter of nanostars from 106.3 ± 0.4 nm to 119.1 ± 0.6 nm for 4-ATP coated nanostars and 140.6 ± 2.1 nm for nanostars functionalized with both 4-ATP and EpCAM aptamer.

The surface ligand exchange was further confirmed by a shift of ζ potential of the colloidal nanoparticles measured by the Zetasizer. The ζ potential is a measure of the electrophoretic mobility or net charge of nanoparticles. The results of the surface charges of the nanostars have been summarized in **Table 3.1**. We observed a shift in ζ potential

from -37.3 ± 0.4 mV to 51.8 ± 0.1 mV after addition of 4-ATP to surfactant-free stars. The nanostars were then re-suspended in 1X PBS at pH 7.4, at which point they displayed a surface charge of 9.7 ± 0.3 mV that then decreased to -15.3 ± 0.1 mV upon successful binding to the negatively charged thiolated EpCAM aptamer. The results seen were consistent with the expected charge contributions of 4-ATP and negatively charged DNA aptamer.

Table 3.1 Zeta potential values (mV) of gold nanostars observed after functionalization with 4-ATP and EpCAM aptamer. Results are shown as mean \pm standard deviation with $n = 3$ readings for each sample.

NP	Zeta potential (mV)
NS in water	-37.3 ± 0.4
NS-4-ATP in water	51.8 ± 0.1
NS-4-ATP in PBS	9.7 ± 0.3
NS-4-ATP-Aptamer	-15.3 ± 0.1

The addition of aptamer to the SERS tags was also confirmed using SERS. A solution of nanostars with 4-ATP and nanostars with 4-ATP and SYL3C aptamer was drop-casted onto a glass slide. The SERS measurements from each of the samples (average of three $5 \mu\text{m} \times 5 \mu\text{m}$ maps) are shown in **Figure 3.2**. The SERS spectra of 4-ATP on nanostars showed strong peaks at 1076, 1182, 1387, 1430 and 1568 cm^{-1} . These peaks were assigned to νCS , δCH , $\delta\text{CH}+\nu\text{CC}$, $\nu\text{CC}+\delta\text{CH}$, and νCC respectively.²⁰⁻²² Upon addition of the aptamer to the 4-ATP functionalized nanostars, the peaks at 1136, 1382, and 1426 cm^{-1} shifted by less than 5 cm^{-1} and reduced in intensity indicating successful binding of the aptamer. The intense peak at 1076 cm^{-1} , corresponding to the stretching band of C-S bonds in 4-ATP molecules, was still prominent after aptamer addition and was therefore

chosen for concentration studies with soluble EpCAM protein. All the SERS peak assignments for 4-ATP have been summarized in **Table 3.2**.

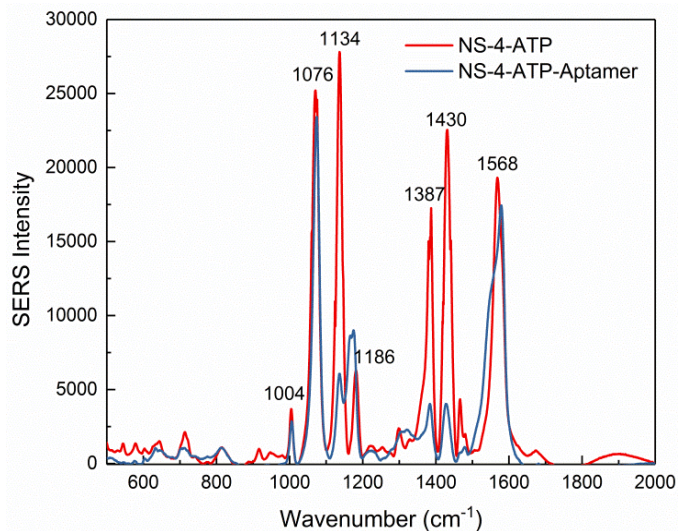


Figure 3.2 SERS spectra of 4-ATP coated nanostars and 4-ATP and EpCAM aptamer coated nanostars. Despite introduction of additional peak after functionalization with the thiolated aptamer, the peak at 1076 cm^{-1} is still dominant.

Table 3.2 SERS peak assignments for 4-aminothiophenol between 500 and 2000 cm^{-1} . The symbols δ , ν , and π correspond to bending, stretching, and wagging modes, respectively.

SERS Peaks	Peak Assignment
1614	δNH
1568	νCC
1495	$\nu\text{CC}+\delta\text{CH}$
1430	$\nu\text{CC}+\delta\text{CH}$
1387	$\delta\text{CH}+\nu\text{CC}$
1298	$\nu\text{CC}+\delta\text{CH}$
1182	δCH
1134	δCH
1076	νCS
1004	$\gamma\text{CC}+\gamma\text{CCC}$
914	πCH
713	$\pi\text{CH}+\pi\text{CS}+\pi\text{CC}$

3.4.2 Substrate Preparation

The overall procedure for the design of the substrate to capture EpCAM protein is shown in **Scheme 3.1**. The first step after silanization of the glass slides is the addition of gold nanostars. We chose a concentration of 3 nM which ensured a uniform nanostar distribution without substantial clustering. The distribution of unmodified nanostars on the surface of the substrate was visualized by scanning electron microscopy (SEM), as seen in **Figure 3.3**. The second step in the substrate preparation was the *in situ* functionalization with the suitable aptamer. We chose a 48 bp SYL3C sequence against EpCAM, which is a tri-hairpin structured sequence with strong binding affinity and selectivity against cancer cells expressing EpCAM (**Figure S3.1**).¹⁶ The aptamer sequence was designed to possess a thiol group to enable binding to the surface of the gold nanostars. In order to optimize aptamer-protein recognition while avoiding non-specific binding, the substrate was backfilled with 6-mercaptohexanol (MCH). The presence of MCH prevents non-specific adsorption of the aptamer to the gold surface and improves the binding efficiency of the aptamer to its target.²³ The substrates were later incubated with varying concentrations of EpCAM protein that was prepared in the binding buffer specific for this aptamer-target pair (1X PBS, pH 7.4 with 4.5 g/L glucose and 5 mM MgCl₂) and allowed to interact. The final step in the substrate preparation was the addition of SERS tags to identify and localize aptamer-protein binding events.

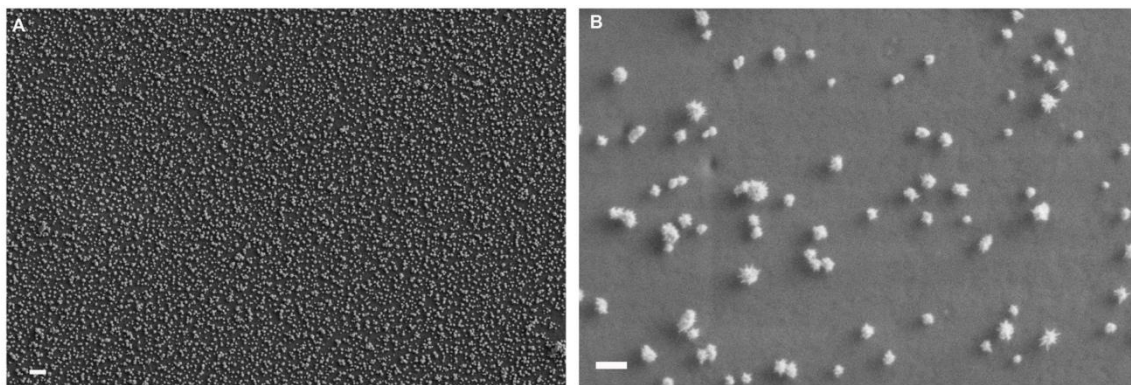


Figure 3.3 Scanning electron micrographs (SEM) of the substrate show uniform distribution of gold nanostars on its surface (A), with retained nanoparticle morphology (B). Slight reshaping is often induced by the electron beam. Scale bars are 1 μm in (A) and 200 nm in (B).

3.4.3 AFM measurements

Atomic force microscopy (AFM) measurements ($5 \times 5 \mu\text{m}^2$ area) were carried out on the substrates to analyze surface features emerging and/or disappearing at each step of the substrate preparation. The images in **Figure 3.4** provide an overview of distribution and binding of each reagent on the developed substrates and show the height profile at each functionalization step. **Figure 3.4A** shows the first step after addition of gold nanostars to a glass slide. At this stage, the substrates show an average height of 126 nm which is consistent with the size of nanostars measured via TEM. Thiolated EpCAM aptamers at 1 μM concentration were then deposited onto the substrate (**Figure 3.4B**), which showed an average height increase of 8 nm. This height could correspond to the presence of several aptamer strands lying flat on the surface of nanostars, possibly due to G-rich, ribbon-like structures that might have formed as a result of the high GC content (60.4%) in the aptamer sequence, as well as of non-specific adsorption of the nucleotide bases to the gold surface.^{23, 24} Therefore, we determined that a spacer such as MCH was necessary to remove non-specific binding and evenly distribute the aptamer across the substrate to

improve target binding and identification. Upon addition of MCH, a redistribution of the aptamer strands was observed, as seen in **Figure 3.4C**. As expected, the addition of MCH eliminates non-specific adsorption of the aptamer on the gold nanoparticle surface²³ resulting in a height change of 34 nm, which corresponds to the length of the aptamer (inclusive of the C6 spacer and the rhodamine red dye) in its extended form. The substrates were then treated with 500 nM EpCAM protein (**Figure 3.4D**), which caused an increase in height to 182 nm. The observed 14 nm increase in height is likely due to the capture of two protein molecules on the surface of nanostars. Finally, SERS tags were added to the substrate (**Figure 3.4E**). The areas where the SERS tags recognized and bonded the protein showed a height of 208 nm while the rest of the substrates did not see a change in height. In the last two steps, we observed that the binding of the protein to the aptamer on the substrates was uneven, implying that the recognition of the target by the aptamer sequence could be different when occurring on a substrate, as opposed to when both the aptamer and the target are in suspension.

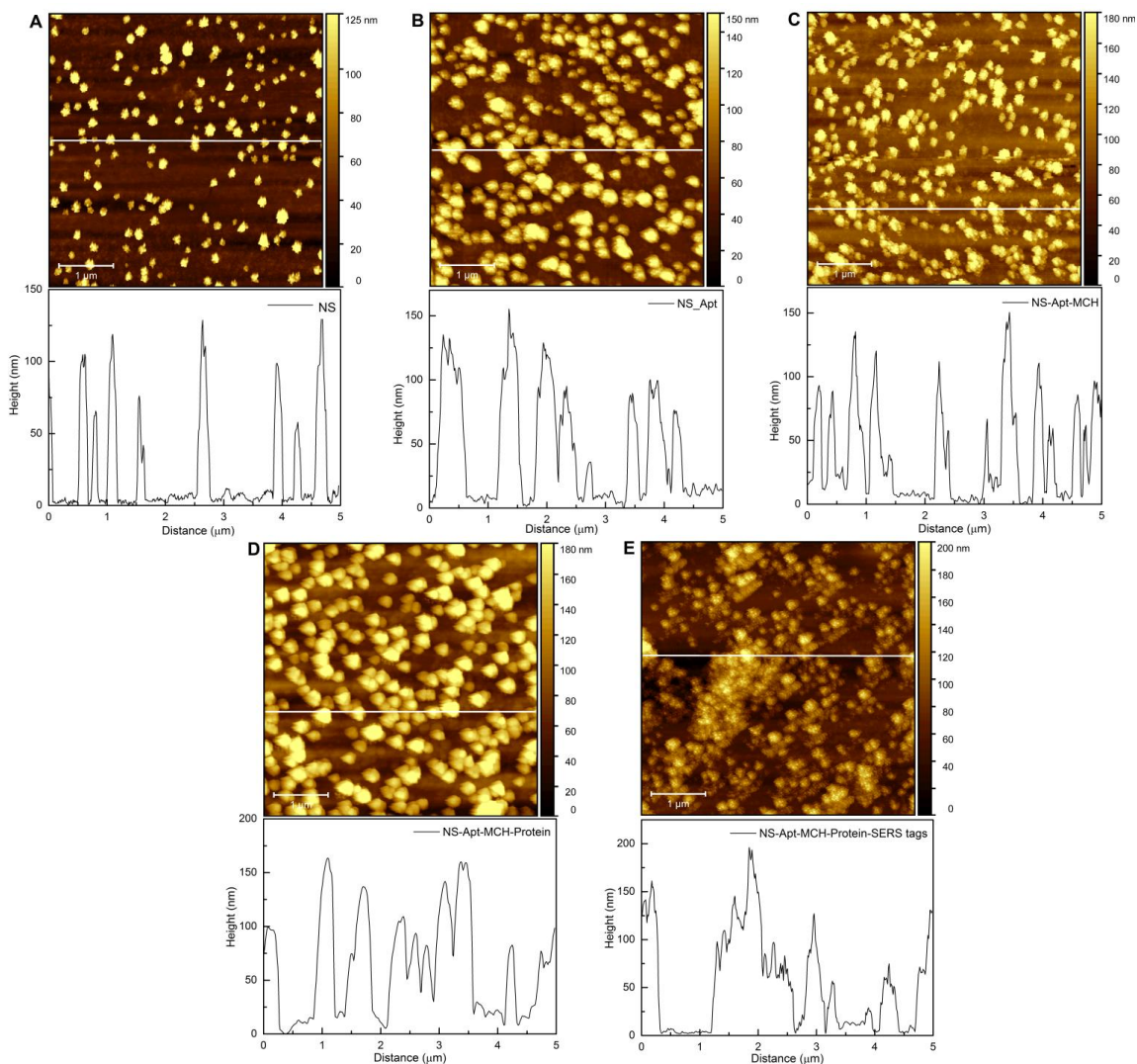


Figure 3.4 Topography and height profiles of the substrate at various functionalization steps collected via atomic force microscopy (AFM). (a) Substrate with nanostars only ($h=126$ nm), (b) substrate with nanostars functionalized with EpCAM aptamer ($h=134$ nm), (c) substrate with EpCAM-functionalized nanostars after addition of 6-mercaptopexanol (MCH) ($h=168$ nm), (d) substrate with EpCAM- and MCH-functionalized nanostars after addition of EpCAM protein ($h=182$ nm), and (e) after addition of SERS tags ($h=208$ nm). A clear increase in the height profile can be observed at each stage. Between steps C and D there is no net height increase, as a consequence of aptamer folding from its extended conformation in the self assembled monolayer after recognition of the target protein.

3.5 SERS measurements

SERS measurements of different concentrations of EpCAM protein recognized and captured by the SYL3C aptamer were carried out on the prepared substrates. From **Figure 3.5**, it is evident that the SERS intensity increased as the concentration of the soluble EpCAM protein increased, as, in turn, more SERS tags were captured by increasing amounts of protein recognized in the sandwich assay. **Figure 3.5B** shows the intensity of the characteristic Raman band of 4-ATP at 1076 cm^{-1} varying with the concentration of EpCAM protein added to the substrates. Each data point represents the average of three $5\text{ }\mu\text{m} \times 5\text{ }\mu\text{m}$ maps collected randomly on each substrate. Further analysis showed a linear correlation ($R^2=0.996$) between SERS intensity and the log of the EpCAM protein concentration in nM between the concentrations of 500 nM and 3 μM with a calibration curve characterized by the equation $y = 19738.91 + 3092.87x$.

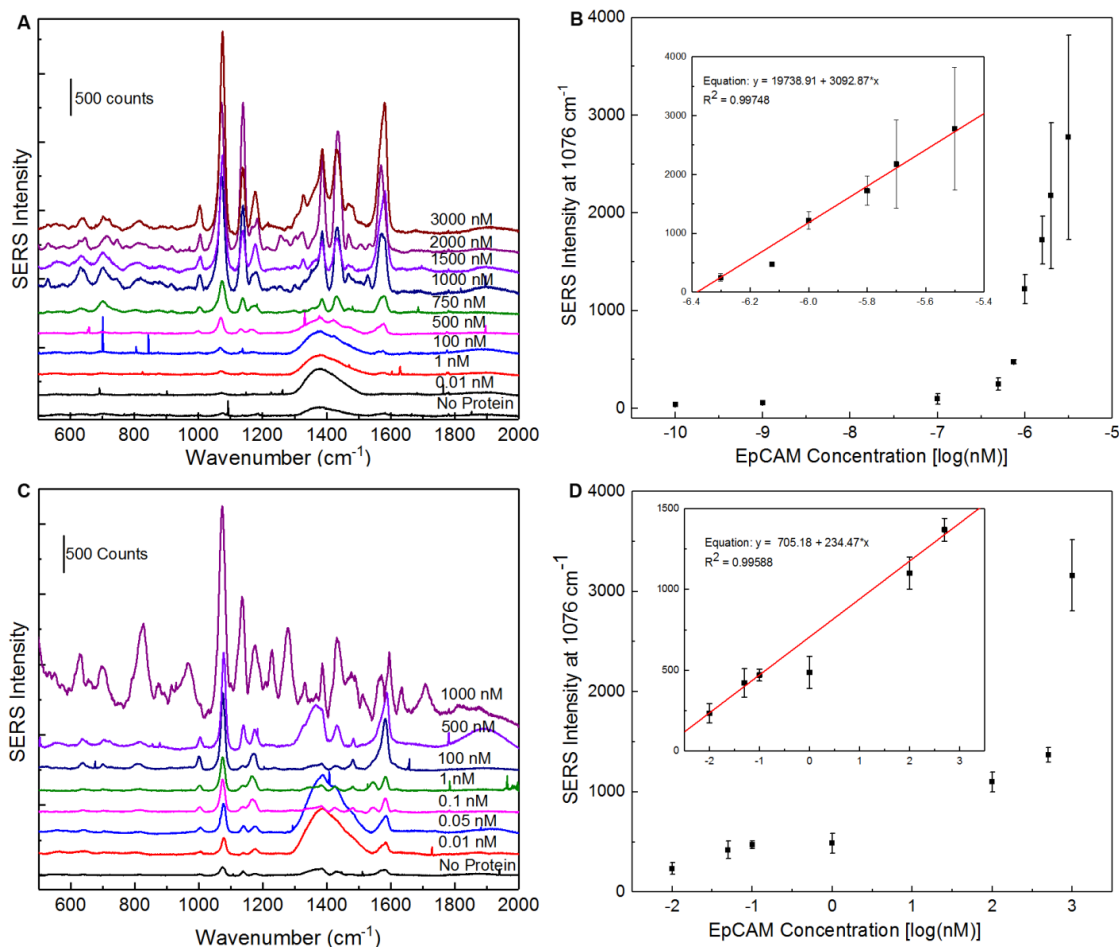


Figure 3.5 SERS spectra collected on the substrates after exposure to increasing concentrations of EpCAM. Figures 5(A) and 5(C) show the SERS spectra for protein capture carried out with the 48-bp and the 17-bp EpCAM aptamers, respectively. Figures 3.5(B) and 3.5(D) shows the intensity variation of the 1076 cm^{-1} peak with respect to the EpCAM protein concentration ($\log(\text{nM})$), for the 48-bp and 17-bp aptamer respectively. Inset figures show the linear dynamic range regime.

In order to test the selectivity of the EpCAM aptamer, we chose two control proteins, bovine serum albumin (BSA) and fibrinogen at a concentration of 500 nM each. The SERS intensity obtained from the substrates of each of the control proteins was then compared to the intensity of EpCAM protein at 500 nM (**Figure 3.6**). Both the control proteins showed a much lower intensity at the characteristic peak of 1076 cm^{-1} when

compared to the EpCAM protein at the same concentration. These results indicate that the substrates developed with the SYL3C EpCAM aptamer have specificity only for EpCAM protein. The limit of detection for the assay was found to be 1 nM. We wondered if the structure of the hairpin loops formed by the aptamer at the incubation temperature (room

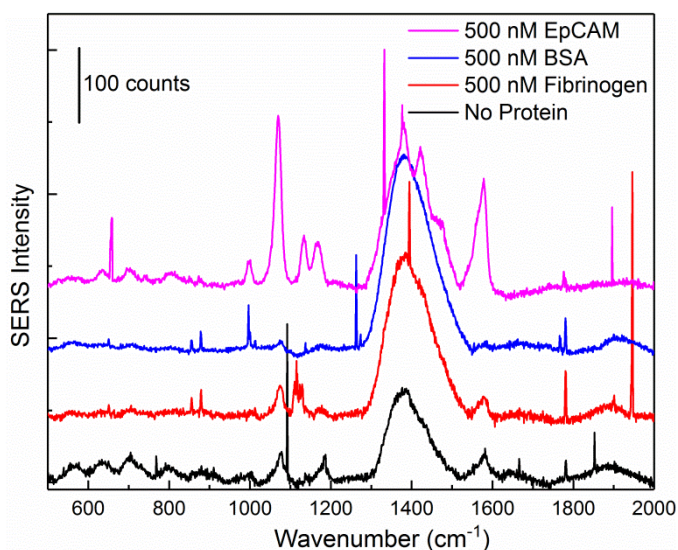


Figure 3.6 Assessment of assay selectivity. SERS spectra collected in the presence of 500 nM EpCAM and two control proteins, BSA and fibrinogen, in addition to the control without protein. The peak at ca. 1400 cm^{-1} is due to the interference of the glass substrate.

temperature) played a role in its sensitivity. Using the OligoAnalyzer 3.1 tool (Integrated DNA Technologies, Inc.), we found that 7 different configurations (**Figure 3.7**) of the three hairpin loops are similarly favored energetically at $25\text{ }^{\circ}\text{C}$, making it likely for them to be rapidly interconverting. Since the recognition of the protein by the aptamer depends on both conformational and electrostatic interactions between oligonucleotide and target, it is likely that the conformational conversions might impact effective target recognition and binding, thus affecting assay sensitivity. In order to reduce the possible configurations at the incubation temperature, and thus improve the sensitivity of the assay, we used a truncated aptamer sequence that was developed from the SYL3C

sequence. The shorter 17 bp EpA aptamer has a single hairpin loop with only 2 possible secondary configurations at 25 °C, which reduces the possibility of conformational changes at room temperature hence increasing sensitivity.

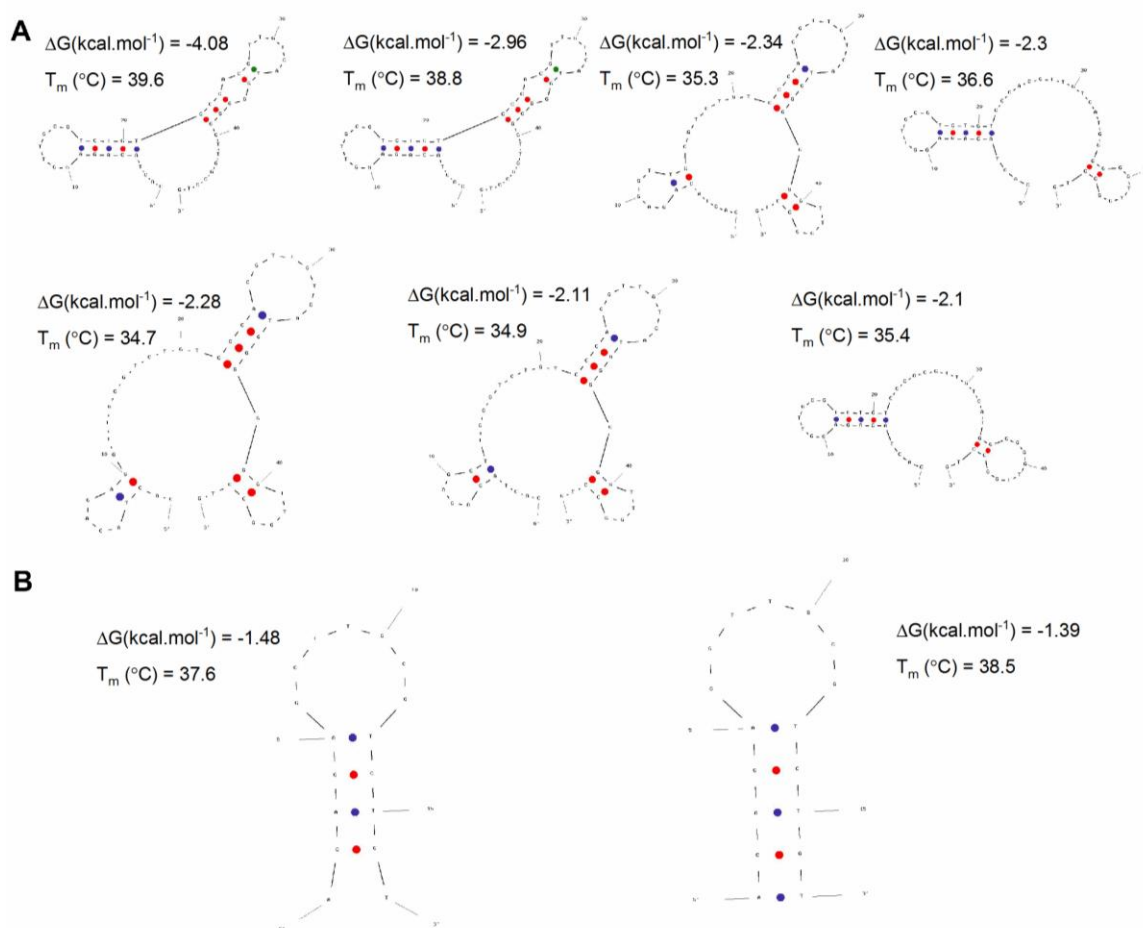


Figure 3.7 Different stem loop conformations at 25 °C for A) the 48-bp and B) the truncated 17-bp EpCAM DNA aptamer. A significantly higher number of almost degenerate conformations can be observed for the longer aptamer, compared to its truncated counterpart. The secondary structures of the aptamer were generated using the OligoAnalyzer 3.1 software from Integrated DNA Technologies, Inc.

The shorter aptamer was found to lead to higher assay sensitivity when compared to the longer SYL3C EpCAM aptamer.¹⁷ We tested the binding affinity of the shorter EpA aptamer sequence using different concentrations of EpCAM protein (1 μM to 10 pM). At

the two highest concentrations, the SERS intensities obtained with the shorter EpA aptamer (**Figure 3.5C**) were found to be three-fold higher at 1 μM and 5.7 times higher at 500 nM protein concentration when compared to the SYL3C aptamer in the same conditions. In addition to higher intensities, the shorter EpA aptamer sequence exposed to 1 μM EpCAM protein showed additional peaks at 1229, 1276, 1633 and 1707 cm^{-1} , which we assigned to the SERS peaks of 6-FAM that is present at the 3' *terminus* of the 17 bp aptamer sequence (**Figure 3.8**). At this protein concentration, it could be possible for the dye to interact differently with the active metallic surface compared to what was observed at lower concentrations of protein. Since SERS is a tensorial technique, the conformation of the reporter molecule and its presentation with respect to the metallic surface are important. Thus, the additional peaks suggest that aptamer folding might depend not only on the concentration and packing of the aptamer on the metallic surface, but also on its interaction with the target protein.

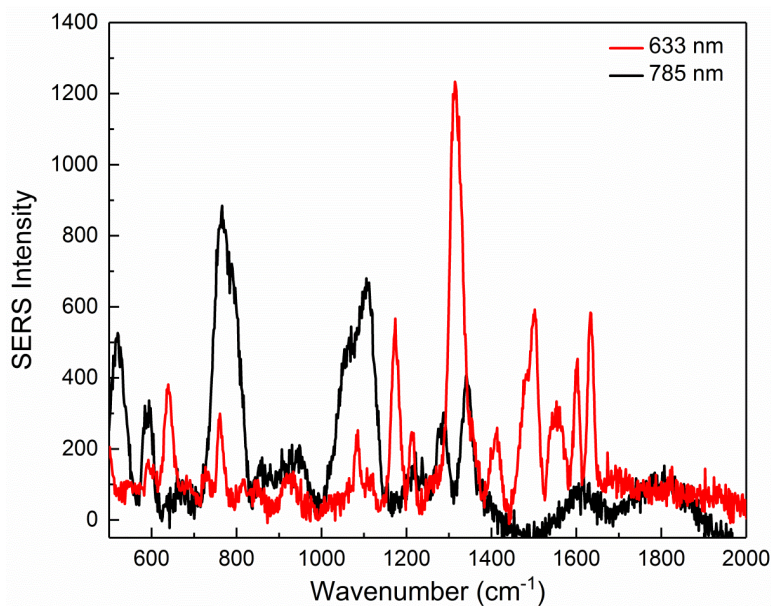


Figure 3.8 SERS spectra of FITC taken using 633 nm and 785 nm laser excitation

Like the SYL3C aptamer, the shorter aptamer sequence also showed a linear correlation ($R^2 = 0.995$) between SERS intensity and the log of the EpCAM protein concentration in nM (**Figure 3.5D**) between the concentrations of 10 pM and 500 nM with a calibration curve that is represented by the equation $y = 705.108 + 234.47x$. The lowest concentration of protein that we could detect with the EpA-conjugated substrates was 10 pM. Because of the improved sensitivity it enabled, the EpA aptamer was chosen for further experiments in cancer cells.

For the cell capture experiments, we chose two EpCAM positive cell lines, a breast cancer cell line, MCF-7 and a prostate cancer cell line, PC-3. These cells were chosen because of the different levels of EpCAM biomarker expressed on their cell surfaces. In addition to these two EpCAM positive cell lines, an EpCAM negative cell line, HeLa, was chosen as a negative control. The surface expression of EpCAM on all three cells was confirmed via flow cytometry. The results from these experiments (**Figure 3.9**) confirmed that MCF-7 cells have higher expression of EpCAM when compared to PC-3 cells, and that HeLa cells does not express the biomarker. However, population-averaged results cannot provide the single-cell insight that is necessary to pinpoint the presence of abnormal cells, for instance cells that are undergoing epithelial to mesenchymal transition, which are often encountered in very low numbers. Thus, leveraging the promising results obtained with the described nanostar-based assay, we ran a set of experiments aimed at quantifying, at the single cell level, the expression of specific cancer cell biomarkers.

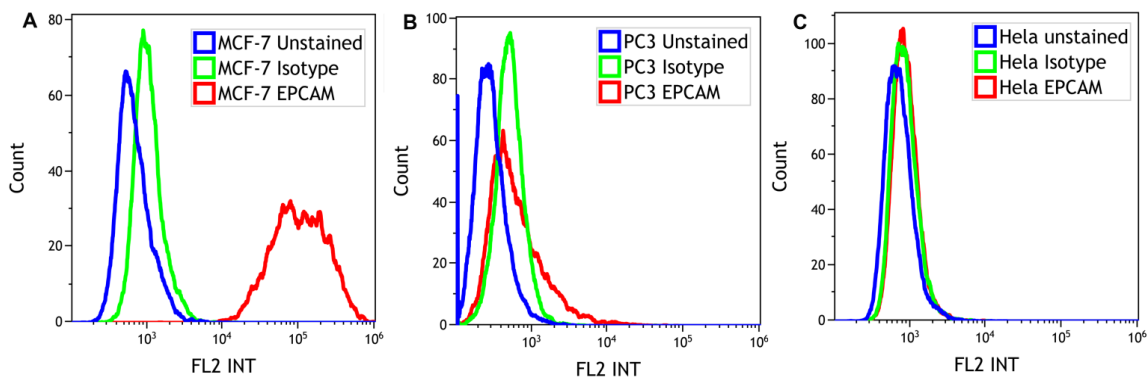


Figure 3.9 Flow cytometry results showing that MCF-7 and PC-3 cells are EpCAM positive cells while HeLa are EpCAM negative cells.

Upon confirmation of expression of EpCAM on cell surfaces, the desired numbers of MCF-7 and PC-3 cells (10 cells to 50,000 cells) were counted and re-suspended in 50 μ L of 1X PBS and loaded onto the substrates. After incubation at 37°C for 1 hour, the substrates were washed and fixed. The capture yields of cells between 10 and 5000 cells were then evaluated by counting the captured cells under a bright field microscope (**Figure 3.10**). For both cell lines, at low cell counts (10 cells), a capture efficiency of 40% was observed. Upon increasing cell numbers, the capture efficiency increased, as expected.^{25, 26} Overall, more MCF-7 cells were captured when compared to PC-3 cells. This could be attributed to the higher EpCAM expression seen on MCF-7 cells. Above a cell count of 5000 cells, the capture efficiency for both cell lines was found to be greater than 60%. On the other hand, a very low capture (0.067%) was seen with the EpCAM negative cell line, HeLa when 1000 cells were added to the substrate.

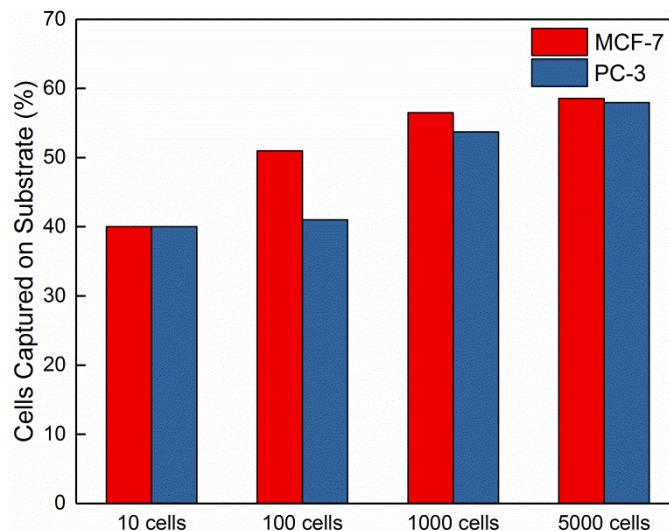


Figure 3.10 Cell capture efficiency (%) of the cancer cells, MCF-7 and PC-3, on the SERS substrates.

The captured cells were then labeled with SERS tags for SERS measurements. Both MCF-7 cells and PC-3 cells showed an enhancement of the characteristic peak of 4-ATP at 1076 cm^{-1} (**Figure 3.11**) which increased linearly with increasing cell numbers between 100 cells and 50,000 cells. The detection limit with these substrates was found to be 10 cells. Higher SERS intensities were observed with MCF-7 cells when compared to PC-3 cells, in agreement with flow cytometry results. In addition, the substrates showed very low SERS enhancement (**Figure 3.12**) at a concentration of 1000 cells with the EpCAM negative cells, HeLa, when compared to the two positive cell lines at the same concentration.

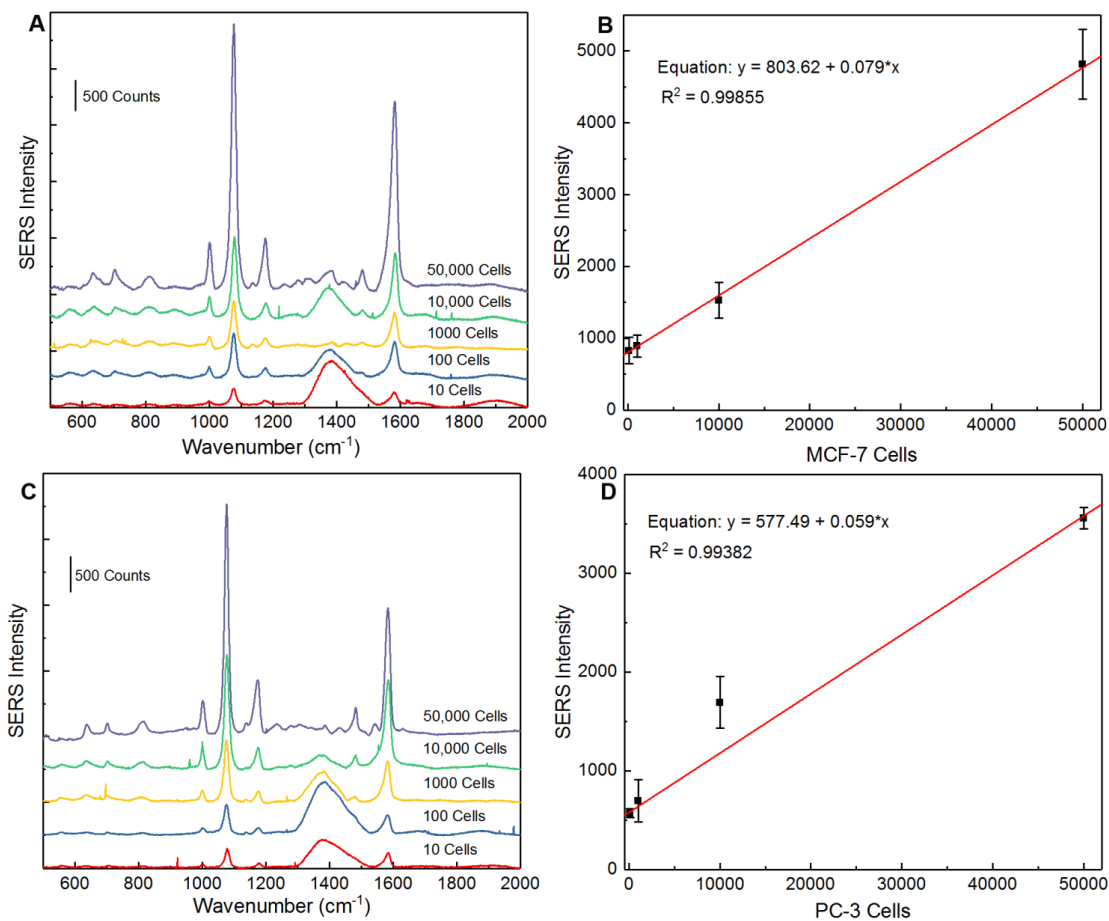


Figure 3.11 Quantification of MCF-7 (A, B) and PC3 (C, D) cells using the described assay. By monitoring the intensity of the 1076 cm^{-1} peak (A), it can be observed how the SERS response linearly increases with increasing number of MCF-7 cells between the wavenumbers 500 and 2000 cm^{-1} (B). Similarly, dependence between the intensity of the 1076 cm^{-1} peak and the number of MCF-7 cells is also linear (C and D).

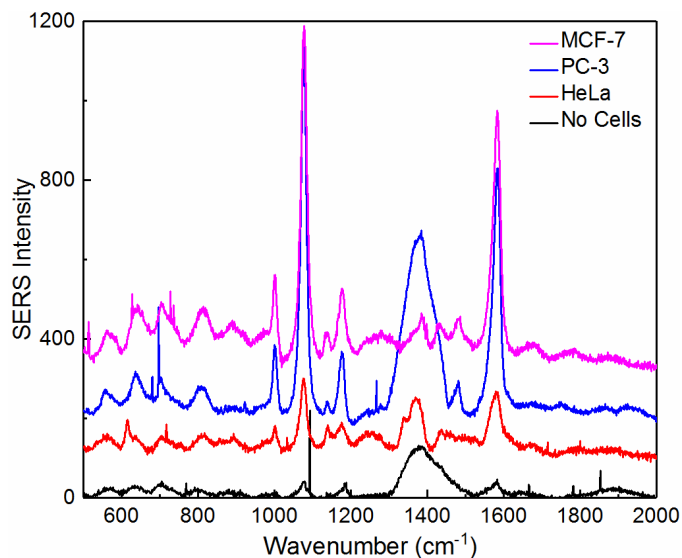


Figure 3.12 Assessment of assay selectivity on cells with different membrane expression of EpCAM (MCF-7 and PC3) or with no expressed EpCAM. A control spectrum without cells is also shown.

In order to estimate the number of EpCAM molecules present on the cancer cells, we calculated the number of EpCAM molecules at different concentrations based the calibration curve reported in **Figure 3.5(D)**. The number of molecules at each concentration was calculated using the following equation:

$$\text{(Concentration (M) x (6.023*10}^{23}) \text{ x Volume of Protein Added (L)) / Surface Area of Substrate (}\mu\text{m}^2\text{)}$$

A linear correlation ($R^2 = 0.99677$) was then observed between the log of the number of protein molecules and the SERS intensity as shown in **Figure 3.13(A)**. The relation was represented by the equation $y = 78.16 + 235.84x$. Using this equation and the SERS intensity of MCF-7 and PC-3 cells observed at 1076 cm^{-1} , we calculated the number of EpCAM molecules expressed by the two cell types at the single cell level. The number

density (per μm^2) of EpCAM molecules present on MCF-7 cells was found to be 4.8-fold higher than that of PC-3 cells (**Figure 3.11(B)**).

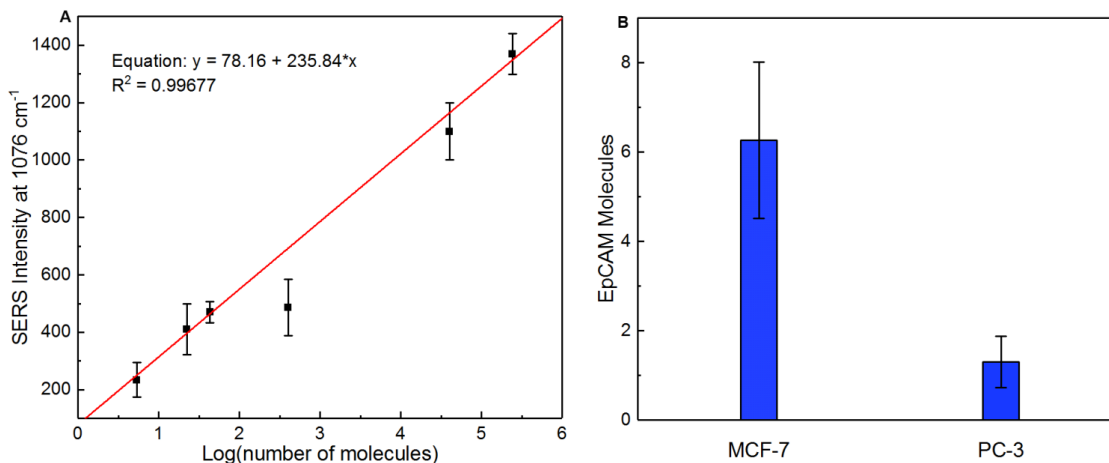


Figure 3.13 Quantification of EpCAM density in individual cells. Figure 3.11(A) shows the linear correlation ($R^2 = 0.99677$) between log of the number of EpCAM molecules found per μm^2 area at different protein concentrations and their SERS response at 1076 cm^{-1} . Using this equation, the number of EpCAM molecules present per μm^2 area on MCF-7 and PC-3 cells was calculated and shown in Figure 3.11(B). Higher expression levels are observed in MCF-7 cells, as expected.

3.6 Conclusion

In conclusion, we developed a SERS-based substrate for the recognition and quantification of EpCAM protein, both soluble and cell membrane-embedded. By leveraging the field-enhancing properties of gold nanostars and the improved recognition and capture enabled by truncated aptamers designed for cell-expressed EpCAM, we detected soluble EpCAM with limits of detection of 10 pM, thus further proving that aptamers designed using cell-SELEX approaches are effective also for the recognition of soluble proteins. By employing the same substrate, we demonstrated that identification and quantification of biomarker expression can be achieved at the single cell level,

enabling one to discern among cells with varying phenotype expression levels. This capability allows to foresee how our approach could be relevant for early cancer detection or for monitoring the onset of metastasis, for which the isolation of individual cells with altered phenotype from populations of cells with uniform biomarker expression is challenging, if not impossible, with techniques such as flow cytometry. Although we have here reported a study targeting EpCAM, it is easy to envision how any biomarker of interest could be targeted, both individually and in multiplex, by simply functionalizing the substrate and the SERS tags with the appropriate aptamers. Importantly, this diagnostic approach does not require protein labeling and, owing to the enhancement capabilities of the nanostar-based substrate, could be implemented with portable Raman spectrometers, making its implementation in the clinic or at bed-side more likely to become a reality.

3.7 References

1. M. Ferrari, *Nat Rev Cancer*, 2005, **5**, 161-171.
2. C. L. Sawyers, *Nature*, 2008, **452**, 548-552.
3. P. Went, M. Vasei, L. Bubendorf, L. Terracciano, L. Tornillo, U. Riede, J. Kononen, R. Simon, G. Sauter and P. A. Baeuerle, *Br J Cancer*, 2006, **94**, 128-135.
4. G. Spizzo, P. Went, S. Dirnhofer, P. Obrist, H. Moch, P. A. Baeuerle, E. Mueller-Holzner, C. Marth, G. Gastl and A. G. Zeimet, *Gynecol Oncol*, 2006, **103**, 483-488.
5. T. M. Gorges, I. Tinhofer, M. Drosch, L. Röse, T. M. Zollner, T. Krahn and O. von Ahsen, *BMC Cancer*, 2012, **12**, 178.
6. K. C. Bantz, A. F. Meyer, N. J. Wittenberg, H. Im, O. Kurtulus, S. H. Lee, N. C. Lindquist, S. H. Oh and C. L. Haynes, *Physical chemistry chemical physics : PCCP*, 2011, **13**, 11551-11567.
7. Y. Wang, B. Yan and L. Chen, *Chemical Reviews*, 2013, **113**, 1391-1428.
8. R. Huang, S. Harmsen, J. M. Samii, H. Karabeber, K. L. Pitter, E. C. Holland and M. F. Kircher, *Theranostics*, 2016, **6**, 1075-1084.
9. H. Y. Cho, M. K. Hossain, J. H. Lee, J. Han, H. J. Lee, K. J. Kim, J. H. Kim, K. B. Lee and J. W. Choi, *Biosensors & bioelectronics*, 2018, **102**, 372-382.
10. L. Rodríguez-Lorenzo, R. A. Álvarez-Puebla, F. J. G. de Abajo and L. M. Liz-Marzán, *The Journal of Physical Chemistry C*, 2010, **114**, 7336-7340.
11. C. Tuerk and L. Gold, *Science*, 1990, **249**, 505-510.
12. A. D. Ellington and J. W. Szostak, *Nature*, 1992, **355**, 850-852.
13. J. L. Vinkenborg, N. Karnowski and M. Famulok, *Nat Chem Biol*, 2011, **7**, 519-527.
14. L. Yang, X. Zhang, M. Ye, J. Jiang, R. Yang, T. Fu, Y. Chen, K. Wang, C. Liu and W. Tan, *Adv Drug Deliv Rev*, 2011, **63**, 1361-1370.
15. L. Cerchia and V. de Franciscis, *Trends in biotechnology*, 2010, **28**, 517-525.
16. Y. Song, Z. Zhu, Y. An, W. Zhang, H. Zhang, D. Liu, C. Yu, W. Duan and C. J. Yang, *Analytical Chemistry*, 2013, **85**, 4141-4149.
17. J. Macdonald, J. Henri, L. Goodman, D. Xiang, W. Duan and S. Shigdar, *ACS Chemical Neuroscience*, 2017, **8**, 777-784.
18. H. Yuan, C. G. Khoury, H. Hwang, C. M. Wilson, G. A. Grant and T. Vo-Dinh, *Nanotechnology*, 2012, **23**, 075102.
19. S. A. Maier, *Plasmonics: fundamentals and applications*, Springer Science & Business Media, 2007.
20. X. Hu, T. Wang, L. Wang and S. Dong, *The Journal of Physical Chemistry C*, 2007, **111**, 6962-6969.
21. L. M. Quynh, N. H. Nam, K. Kong, N. T. Nhung, I. Notingher, M. Henini and N. H. Luong, *Journal of Electronic Materials*, 2016, **45**, 2563-2568.
22. M. Osawa, N. Matsuda, K. Yoshii and I. Uchida, *The Journal of Physical Chemistry*, 1994, **98**, 12702-12707.
23. A. B. Steel, R. L. Levicky, T. M. Herne and M. J. Tarlov, *Biophysical journal*, 2000, **79**, 975-981.
24. J. T. Davis and G. P. Spada, *Chemical Society reviews*, 2007, **36**, 296-313.
25. P. Zhang, R. Zhang, M. Gao and X. Zhang, *ACS applied materials & interfaces*, 2014, **6**, 370-376.

26. S. Wang, H. Wang, J. Jiao, K. J. Chen, G. E. Owens, K. Kamei, J. Sun, D. J. Sherman, C. P. Behrenbruch, H. Wu and H. R. Tseng, *Angew Chem Int Ed Engl*, 2009, **48**, 8970-8973.

**CHAPTER 4 SERS-BASED QUANTIFICATION OF PSMA IN TISSUE
MICROARRAYS ALLOWS EFFECTIVE STRATIFICATION OF PATIENTS
WITH PROSTATE CANCER**

Note: This chapter is currently in submission for the following publication in ACS Omega.

Manjari Bhamidipati, Geuntaek Lee, Isaac Kim, and Laura Fabris. “SERS-based Quantification of PSMA in Tissue Microarrays Allows Effective Stratification of Patients with Prostate Cancer.”

4.1 Abstract

Prostate specific membrane antigen (PSMA), a type II membrane protein, is an attractive biomarker that has been validated clinically for the diagnosis of prostate cancer. In this study, we developed SERS nanoprobe to detect PSMA and quantify its expression at the single cell level. The SERS nanoprobe was developed by employing gold nanostars functionalized with PSMA aptamer. We were able to quantify sub-nanomolar concentrations of PSMA protein in solution and to use the resulting calibration curve to estimate the expression of PSMA on the surface of the prostate cancer cell, LNCaP at the single cell level. Importantly, we employed these SERS tags to stratify prostate cancer patients by assessing PSMA expression in tissues contained in a prostate tissue microarray. The stratification results clearly correlated PSMA expression to recommended therapy groups, thus rendering the described method an effective tool to aid in designing personalized therapeutic protocols. By benchmarking detection sensitivity against immunofluorescence staining and comparing stratification results obtained with the two methods allowed us to validate our novel approach against standard practices. Based on these results, we confirm the validity of PSMA as effective biomarker for prostate cancer patient evaluation and propose SERS-based diagnostic techniques as integrative methods for the assessment of disease stage and the identification of effective therapeutic protocols.

4.2 Introduction

Prostate cancer (PCa) is one of the leading causes of death among male cancer patients.¹ While often being characterized by slow progression, in some patients it is very aggressive and moves fast from the prostate to the lymph nodes and other distant secondary sites, such as bone. PCa is also characterized by very heterogeneous tissue, which makes accurate diagnoses extremely complex. Current diagnostic practices for prostate cancer assessment include clinical staging, prostate specific antigen (PSA) quantification, and Gleason grading of biopsied tissues. While these concurrent approaches have been validated and approved, they are still controversial. For instance, PSA levels can increase even in the absence of cancer, as a consequence of other diseases of the prostate, and can be high even after therapy (e.g. androgen deprivation therapy, ADT) as the result of what is known as biochemical recurrence. Therefore, PSA testing can lead to overtreatment. Additionally, Gleason grading, while providing improved matching to clinical outcomes after being revisited in 2014, can still lead to erroneous diagnoses because of the heterogeneity of the tissues and inter-observer irreproducibility.²

The 2014 revised Gleason grading system assigns a Gleason score to biopsied tissues collected from different sites of the prostate, depending on histological tumor morphology variants, with higher scores assigned to more undifferentiated tissues, i.e. tissues that progressively look less and less like healthy tissues.³ To make up for the heterogeneity of PCa tissues, the method assigns two scores (e.g. 3 and 4) where the first score is indicative of the structure of the majority tissue (in this case 3) while the second describes the minority, surrounding tissue (in this case 4). For this hypothetical sample,

the score would then be $3+4=7$. The grading system then compounds the collected scores into Grade Groups I to V, where I is the group for which therapy deferral (or watchful waiting) is recommended, while groups III and higher are more advanced and recommended surgery and/or therapy (radiation, hormonal, or chemo) (see **Table 1**). The main issue with the Gleason grading system is that it often fails to discriminate among low-risk and high-risk tissues, making it necessary to identify new approaches for patient stratification.⁴ One of the recent new approaches for improving diagnosis and patient stratification involve the discovery and use of new biomarkers other than PSA. Among these, the prostate specific membrane antigen (PSMA), a type II transmembrane protein that is specific to all forms of prostate tissue, has been identified as a therapeutically relevant biomarker and validated clinically.⁵⁻⁶ Increased PSMA expression has been associated with higher recurrence of the tumor⁷, which makes it an attractive target. While recent literature has shown that PSMA levels accurately correlate with PCa aggressiveness and baseline PSA serum levels, we hypothesized that immunohistochemistry-based assessment can only marginally provide the spatial resolution and sensitivity necessary to take into account the high tissue variability and the PSMA expression level in healthy tissues, calling for the need of a more sensitive and spatially resolved technique. In addition, while antibodies have been used and approved for target recognition in the medical community for quite some time, we believe that substituting them with aptamers for effective target recognition and binding would provide more accurate quantification of PSMA in tissues and, therefore, more precise stratification of the patients based on their Gleason Grade groups.

Table 4.1 Explanation of the Gleason scoring system. Score 1 and Score 2 are assigned based on histopathology. Higher values for Score 1 than Score 2 indicate higher disease severity.

Grade Group	Score 1	Score 2	Total Score
I	≤ 3	≤ 3	≤ 6
II	3	4	7
III	4	3	7
IV	4	4	8
V	4	5	9-10
	5	4	
	5	5	

Based on our previous results, we hypothesized that surface enhanced Raman scattering (SERS) could provide the necessary sensitivity and spatial resolution to enable accurate, tissue-specific correlation of PSMA expression in biopsied specimen of prostate cancer in tissue microarrays (TMAs). SERS-based techniques employing gold nanoparticles of different sizes and shapes with tunable optical properties have been used extensively for diagnostic applications.⁸ They offer excellent biocompatibility and low toxicity, and show several advantages over fluorescence, such as the lack of photobleaching. SERS nanoprobes, comprising a plasmonic nanoparticle, a Raman reporter molecule, and targeting molecules (e.g. an aptamer or an antibody), have been shown to effectively target and selectively identify cancerous cells, with the shape of the nanoparticle greatly influencing its optical properties and hence the brightness of the nanoprobe.⁸ Gold nanostars, in particular, have been shown to possess excellent field enhancement properties, which have enabled single molecule detection.⁹ Furthermore, the use of aptamers as targeting moieties bound to the nanoparticles, has enabled us to quantify the

expression of biomarkers in individual PCa cells, making a strong case for the use of these molecules over antibodies.

In this study, we developed SERS nanoprobe functionalized with PSMA aptamer molecules that allowed us to quantify PSMA expression in prostate cancer cells at the single cell level and PCa TMAs comprising of biopsied specimens from 34 patients at different stages of the disease. For this purpose, we used a 39 nucleotide PSMA RNA aptamer that was developed by Dassie *et al.*¹⁰ Detailed characterization of the SERS probes was carried out using transmission electron microscopy (TEM), dynamic light scattering (DLS), zeta potential, and UV-Vis spectroscopy. To prove the effectiveness of our SERS probes toward the detection of PSMA, we first built a concentration curve for the SERS-based assay, with which we were able to estimate the expression of PSMA in individual prostate cancer cells, LNCaP, using aptamers as targeting moieties and PC3 cells as non-overexpressing cell controls. We also compared the effectiveness of the aptamers vs. antibodies by targeting PSMA in LNCaP cells using fluorescently labeled aptamers and antibodies, demonstrating a substantially higher recognition with the former. These SERS tags were then used to estimate the expression of PSMA in a prostate TMAs, using as a benchmarking technique immunofluorescence staining, in which specimen with Gleason scores between 6 and 9 were present. Our results show that SERS outperforms fluorescence-based immunohistochemistry for quantification of PSMA and enables the stratification of patients in three clearly distinct recommended therapy groups, namely the watchful waiting group, the non-metastatic active therapy group, and the metastasized and/or castration resistant group, based on compounded PSMA expression data. This retrospective study allowed not only to confirm PSMA as an

effective biomarker for the evaluation of disease stage, but also led to an improved stratification of patients into groups of recommended therapeutic regimen. In the future, the implementation of the approach in longitudinal studies promises to become a valuable method for monitoring disease progression and response to therapy.

4.3 Materials and Methods

4.3.1 Nanoparticle Synthesis

Gold nanostars were synthesized according to the surfactant-free nanostar synthesis developed by Yuan *et al.*¹¹ For this, 2 mL of H₂AuCl₄ salt solution (0.025 M) and 200 μ L of 1 N HCl were added to 48 mL of Milli-Q water. 12 nm citrate-capped spheres (125 μ L at A=2.81) were then added to the mixture and mixed thoroughly by stirring. Then, 1 mL of 100 mM ascorbic acid and 2 mL of 3 mM AgNO₃ were simultaneously added to the above mixture. The reaction was carried out for 7 min under gentle stirring and then purified by centrifugation at 4000 g for 10 min.

4.3.2 Preparation of SERS tags

The thiolated PSMA RNA aptamer A10-3.2 (39 nucleotides) developed by Dassie *et al.*¹⁰ [5'-HS-(CH₂)₆-CAC GGG AGG ACG AUG CGG AUC AGC CAU GUU UAC GUC ACU CCU-3', Integrated DNA Technologies Inc.] was dissolved in RNase free DEPC treated water (Thermo Fisher). For the fluorescent experiments, the PSMA aptamer was purchased with Alexa Fluor 488 at the 3' end. For the preparation of SERS tags, the gold nanostars synthesized above were purified and re-suspended at a concentration of 3 nM. They were then allowed to react with 4-aminothiophenol (Sigma-Aldrich) for 30 min at a

final concentration of 1 μM . Following this, the thiolated PSMA aptamer was then added to the nanoparticles at a final concentration of 0.5 μM . The prepared SERS tags were allowed to react for an additional 30 min after which they were washed thoroughly and re-suspended in MilliQ water.

4.3.3 Characterization of NPs and SERS tags

The UV-Vis spectra were recorded on an SI Photonics Model 440 spectrophotometer. The morphology of synthesized nanostars and SERS tags was evaluated using a Philips CM12 transmission electron microscope. The size information of the NPs was extracted using Image J software. DLS and zeta potential measurements were performed using a Malvern Zetasizer Nano-ZS instrument. Three sequential measurements were performed for the experiments in water with flow cell configuration. The zetapotential data were fit using Smoluchowski's theory.

The amount of RNA aptamer loaded onto the particles was quantified using Quant-iT™ OliGreen® ssDNA assay kit (Thermo Fisher).

4.3.4 SERS Measurements

All SERS measurements were carried out using a Renishaw in Via Raman microscope. The spectra were obtained with a 633 nm HeNe laser at a laser power of 0.101 mW using a data acquisition time of 1 s, single accumulation under a 20x objective. For each of the protein and cell samples, three maps of 5 x 5 μm^2 sized areas were chosen at random places of the sample. The areas were raster-scanned with a 1 μm step size. The final SERS spectra shown are averages of the three maps obtained. The intensity of a Si peak at 520 cm^{-1} was used as an internal reference. For SERS maps in prostate tissue

microarrays, five maps of $100 \times 100 \mu\text{m}^2$ area of samples were raster-scanned under the same acquisition conditions as above with $10 \mu\text{m}$ step size. The maps were then averaged and the background was subtracted for each of the spectra.

4.3.5 Substrate Preparation for Protein Functionalization

The substrates for protein experiments were prepared in a similar way as described previously. Briefly, plain glass microscope slides were cut into approximately $0.5 \text{ cm} \times 1 \text{ cm}$ sized substrates. They were rinsed thoroughly and immersed in a 2% solution of 3-aminopropyltriethoxysilane (APTES) for 20 minutes. Afterwards, they were placed in an oven set to 110°C for 1 hour. The substrates were then immersed in a 0.3% solution of bovine serum albumin (BSA) for 1 hour. The resultant APTES functionalized substrates were incubated with a 3 nM solution of nanostars for 1 hour under gentle stirring. Subsequently, the thiolated PSMA aptamer at $1 \mu\text{M}$ concentration was deposited on the substrates and allowed to bind overnight. The substrates were then rinsed and incubated in a 1 mM 50% ethanolic solution of 6-mercaptohexanol (MCH) for 1 hour. After this, 50 μL of the desired concentration (32 pM to 320 nM concentration) of PSMA protein (Sino Biological USA Inc.) was deposited on the substrates for 1 h. They were then washed thoroughly and allowed to react with the SERS tags containing PSMA aptamer described above for an additional hour, following which they were analyzed for their SERS activity.

4.3.6 Cell Culture

In this work, PSMA expressing prostate cancer cells, LNCaP, and PSMA-negative cell line, PC-3 were used. Both cell lines were cultured in RPMI 1640 media (Sigma-Aldrich)

that was supplemented with 10% Fetal Bovine Serum (Gibco, Thermo Fisher). Cells were grown at 37°C with 5% CO₂. Expression of PSMA on both cell lines was confirmed by staining the cells with 1:50 diluted PSMA antibody conjugated with Alexa Fluor 488 (Thermo Fisher) and the labeled PSMA aptamer at 2 μM concentration. Cell nuclei were stained with DAPI (Thermo Fisher) as per the manufacturer's instructions. After confirmation of the expression of PSMA on LNCaP cells, the cells were trypsinized and seeded at a density of 20,000 cells/well in a 96-well tissue culture plate. They were allowed to attach for 24 h following which the media was replaced, and SERS tags at a broad concentration range (1 nM to 5 nM) were added to the wells. Cell viability was measured using an MTT proliferation assay kit (Thermo Fisher) according to the manufacturer's protocol after exposure to different concentrations of SERS tags for 24 h. For SERS measurements, the appropriate number of LNCaP and PC-3 cells were counted and plated in 96-well plate. They were allowed to attach overnight. The media was then replaced with fresh media containing SERS tags at 3 nM concentration. They were allowed to react with the tags for 1 hour at 37°C. The cells were then washed thoroughly to remove any unbound tags and fixed with 4% paraformaldehyde in PBS for 10 mins. SERS measurements were then carried out on the cells.

4.3.7 Semi-Quantitative RT-PCR

Total RNA was isolated with TRIzol LS reagent (Thermo Fisher), and 1-2 g of total RNA was used for synthesizing cDNA using a high-capacity cDNA Reverse Transcription Kit (Thermo Fisher). The cDNA was then used for quantitative PCR in a StepOnePlus™ (Applied Biosystems) with SYBR Green ROX qPCR Mastermix (Qiagen) and semi-quantitative PCR. The PCR primers for PSMA and β-actin that were used are shown as

follows:PSMA(Forward:GAAACCGACTCGGCTGTGG,Reverse:TAAACCACCCGAA GAGGAAGC); β -actin(Forward:AGAGCTACGAGCTGCCTGAC,Reverse: AGCACTGTGTTGGCGTACAG).

4.3.8 Western Blot Analysis

Prostate cancer cells (LNCaP and PC3) were collected and lysed with lysis buffer (20 mM Tris-HCl (pH 7.5), 150 mM NaCl, 1 mM Na₂EDTA, 1 mM EGTA, 1% Triton, 2.5 mM sodium pyrophosphate, 1 mM beta-glycerophosphate, 1 mM Na₃VO₄, 1 μ g/ml leupeptin) along with 1 mM phenylmethylsulfonyl fluoride (PMSF). The cell lysates were centrifuged and the supernatant was used as protein. After separation of 50 μ g protein via SDS-PAGE, the samples were incubated with a primary monoclonal PSMA antibody (Abcam) and β -actin antibody (Sigma-Aldrich). Following incubation with the appropriate secondary antibody, the immunoblot was analyzed using a SuperSignal West Femto Maximum Sensitivity Substrate (Thermo Fisher).

4.3.9 Tissue Microarray Staining

Paraffin embedded specimens of 1 mm diameter from 34 prostate cancer patients were mounted on a glass slide as a tissue microarray. All tissue sections had prostatic adenocarcinoma with Grade Groups 1-5. The pathological status of the tissue samples were: Grade Group 1 (Gleason score 6) (N=4), Grade Group 2 (Gleason score 3+4=7) (N=11), Grade Group 3 (Gleason score 4+3=7) (N=3), Grade Group 4 (Gleason score 3+5=8; 5+3=8) (N=8) and Grade Group 5 (Gleason score 4+5=9; 5+4=9) (N=8). Removal of paraffin and subsequent re-hydration of the tissue sections was carried out by washing the tissue microarray with xylene, ethanol, ethanol/water mixtures and in

distilled water. Antigen retrieval on the tissue sections was carried out by immersing the slide in a pH 6 citrate buffer (10x Citrate Antigen Retrieval Buffer, Sigma-Aldrich) and heating to 95°C for 20 min. The slide was then cooled to room temperature for 20 min and washed with distilled water. For immunofluorescence staining, the tissue specimens were stained with a primary monoclonal PSMA antibody (Thermo Fisher) followed by a secondary antibody conjugated with TRITC (Thermo Fisher) and imaged. Cell nuclei were stained with DAPI. For SERS measurements, the tissue microarray was incubated with SERS tags at 37°C for 1 h and then imaged.

4.4 Results and Discussion

4.4.1 Preparation of SERS Tags

Gold nanostars were synthesized according to a previously reported surfactant-free protocol,¹¹ and were characterized by a localized surface plasmon resonance (LSPR) band centered at 773 nm. They were then functionalized with the Raman reporter, 4-aminothiophenol (4-ATP) and the thiolated PSMA aptamer. Functionalization of the reporter and the aptamer to the nanoparticles was enabled by the thiol-Au bond formation. The morphology and size of the nanoparticles before and after functionalization was verified by TEM, as seen in **Figure 4.1**. TEM micrographs (**Fig 4.1A, Fig 4.1B**) revealed that the nanostars possess a large number of sharp protruding tips which were retained upon functionalization with the reporter and the aptamer, thereby ensuring that they will still be viable for SERS enhancement. The size of the nanoparticles was found to increase by 12 nm from 98.5 ± 15.1 nm to 110.5 ± 9.1 nm. This increase in size for the nanostars is consistent with the expected size contribution of

the added reporter, 4-ATP, and the PSMA aptamer. In addition to this, a slight red shift from 773 nm to 783 nm in the LSPR position of the nanostars after functionalization was also observed (**Fig 4.1C**). This red shift is expected since the position of the LSPR depends on the dielectric function of the surrounding environment.¹² Dynamic light scattering (DLS) results (**Fig 4.1D**) also showed an increase in the hydrodynamic diameter of nanostars from 120.6 ± 1.8 nm to 129.6 ± 3.5 nm for nanostars functionalized with both 4-ATP and PSMA aptamer.

The functionalization of the nanostars was further confirmed by a shift of ζ potential of the colloidal nanoparticles measured by the Zetasizer. The ζ potential is a measure of the electrophoretic mobility or net charge of nanoparticles. The results of the surface charges of the nanostars have been summarized in **Fig 4.1E**. We observed a shift in ζ potential from -38.9 ± 1.4 mV to -33.3 ± 0.8 mV after addition of 4-ATP to surfactant-free stars. This slight decrease in the negative charge is expected with the addition of the reporter, 4-ATP. Upon addition of the negatively charged RNA aptamer, the nanoparticles displayed an increase in the negative charge to -38.4 ± 0.9 mV. These results further confirmed the successful addition of 4-ATP and PSMA aptamer on the nanoparticles.

To quantify the amount of RNA aptamer functionalized on the tags, and thus ensure that the reproducibility and accuracy of the results, nanostars at different concentrations (1.5 nM and 3 nM) were loaded with different ratios of the reporter molecules, 4-ATP and the thiolated PSMA aptamer. The amount of free RNA leftover in the supernatant was then quantified using a Quant-iT™ OliGreen® ssDNA reagent, which is a sensitive fluorescent stain that binds to oligonucleotides in solution. Based on the results of this

assay (**Table 4.2**), we observed a capture efficiency of 50.02 ± 0.53 % when a concentration of 3 nM nanostars was functionalized with 1 μ M concentration of 4-ATP and 0.5 μ M of PSMA aptamer. These concentrations were found to lead to the highest Raman peak intensity for 4-ATP and were thus chosen for further experiments.

Table 4.2 Table shows the capture efficiency of PSMA RNA aptamer on the nanoparticles detected using the Quant-iT™ OliGreen® ssDNA kit. Two different concentrations of gold nanostars (1.5 nM and 3 nM) were functionalized with varying ratios of the Raman reporter, 4ATP and PSMA aptamer. Results are shown as mean \pm standard deviation with n = 3 readings for each sample.

Particles	Amount of RNA on NP (μ g)	RNA Added (μ g)	Capture Efficiency (%)
1.5 nM NS_0.5 μ M 4ATP_ 0.5 μ M Apt	2.27 ± 0.06	2.34 ± 0.02	48.48 ± 1.29
1.5 nM NS_1 μ M 4ATP_0.5 μ M Apt	1.77 ± 0.08	2.34 ± 0.02	37.79 ± 1.88
1.5 nM NS_2 μ M 4ATP_ 0.5 μ M Apt	1.68 ± 0.09	2.34 ± 0.02	35.94 ± 2.06
3 nM NS_0.5 μ M 4ATP_0.5 μ M Apt	1.99 ± 0.03	4.68 ± 0.04	42.56 ± 0.74
3 nM NS_1 μ M 4ATP_0.5 μ M Apt	2.34 ± 0.02	4.68 ± 0.04	50.02 ± 0.53
3 nM NS_2 μ M 4ATP_0.5 μ M Apt	2.46 ± 0.01	4.68 ± 0.04	52.56 ± 0.23

Binding of PSMA aptamer molecules to the nanoparticles was confirmed using SERS measurements. A solution of the nanostars functionalized with the Raman reporter, 4-ATP, was drop-casted on a glass slide. SERS measurements (three maps of the size 5 μ m x 5 μ m) were averaged and analyzed. The maps revealed strong Raman peaks of 4-ATP

at 994, 1076, 1134, 1387, 1438, 1568 and 1605 cm^{-1} . These peaks were assigned to $\gamma\text{CC}+\gamma\text{CCC}$, νCS , δCH , $\delta\text{CH}+\nu\text{CC}$, $\nu\text{CC}+\delta\text{CH}$, νCC and δNH respectively.¹³⁻¹⁵ The symbols δ , ν , and π correspond to bending, stretching, and wagging modes, respectively. Upon further functionalization of the nanoparticles with the thiolated PSMA aptamer, the peak at 994 cm^{-1} reduced in intensity and shifted by less than 5 cm^{-1} while peaks at 1134, 1387, 1438 and 1575 cm^{-1} increased in intensity. These results indicated successful functionalization with the aptamer. Since the peak at 1438 cm^{-1} , corresponding to the stretching of the C-C bond and bending of the C-H bond in 4-ATP molecules was prominent after addition of the aptamer, it was chosen for concentration studies with soluble PSMA protein.

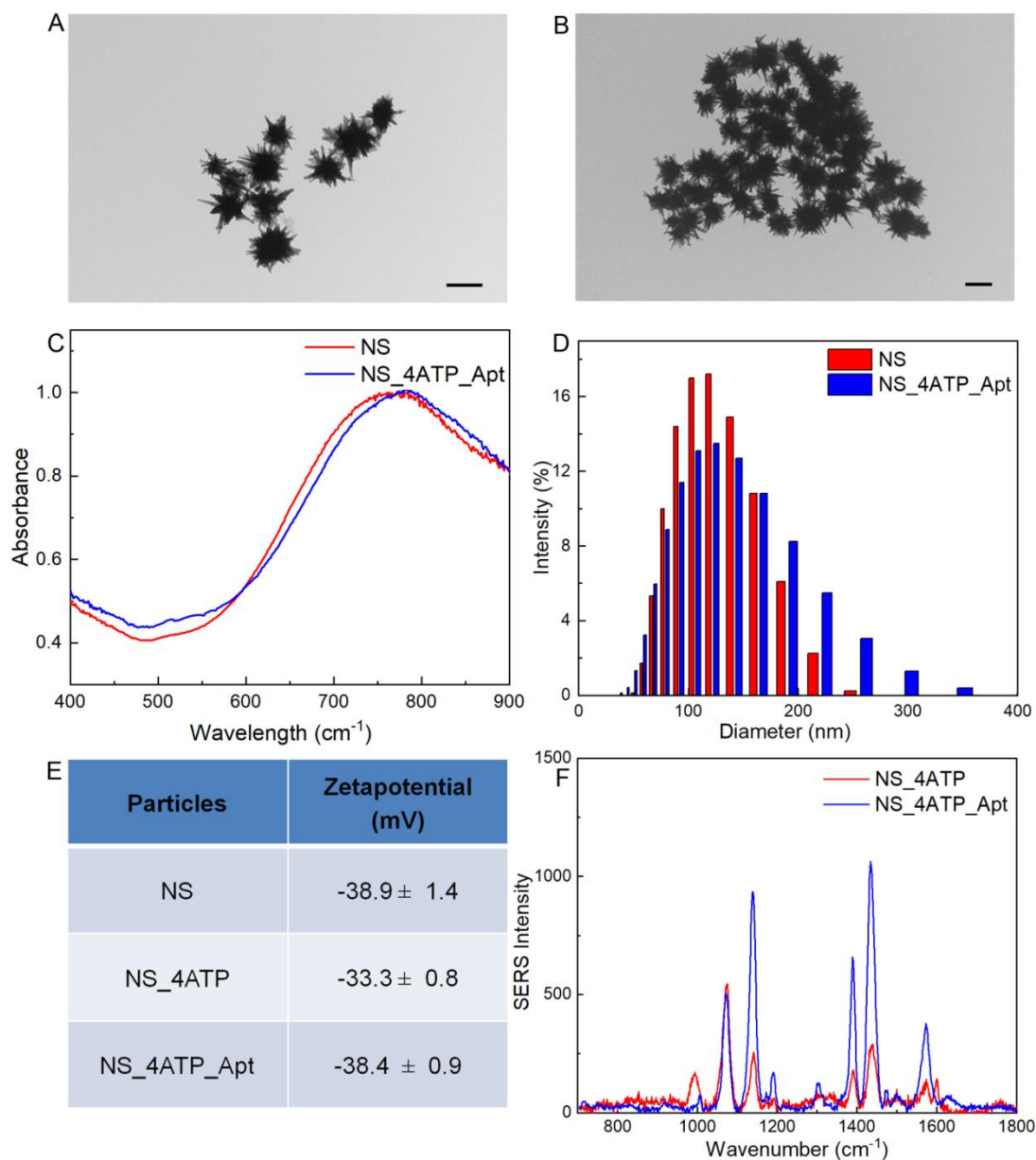


Figure 4.1 Characterization of the synthesized SERS tags was carried out via multiple techniques. Figures 4.1(A) and (B) show the transmission electron (TEM) micrographs of (A) as synthesized nanostars, and (B) nanostars functionalized with 4-ATP and PSMA aptamer. Figure 4.1(C) shows the UV-Vis spectra of nanostars before and after functionalization. Figure 4.1(D) shows the dynamic light scattering (DLS) data, that shows the size distribution of the nanoparticles. Figure 4.1(E) shows the zeta potential (mV) values of the functionalized nanostars with 4-ATP and PSMA aptamer. Results are shown as mean \pm standard deviation with $n = 3$ readings for each sample. Figure 4.1(F) shows the SERS spectra of 4-ATP coated nanostars and nanostars coated with 4-ATP and PSMA aptamer.

4.4.2 Correlating SERS Intensity with Protein Concentration

To correlate SERS intensity and PSMA concentration, we captured soluble PSMA at varying concentrations on functionalized glass substrates and measured the resulting SERS response. The first step in the preparation of the protein substrates was silanization of the glass followed by the addition of gold nanostars at a concentration of 3 nM. This concentration was chosen since it was previously determined to result in a uniform distribution on the substrate with minimal clustering of particles. We then deposited the 39 nucleotide thiolated PSMA aptamer, A10-3.2, developed by Dassie *et al.*¹⁰ at a concentration of 1 μ M. The thiol group on the aptamer enabled binding of the aptamer to the gold nanostars. In order to reduce non-specific binding of the PSMA aptamer on the surface of the gold nanoparticles, the substrate was backfilled with 6-mercaptohexanol (MCH).¹⁶ Different concentrations of PSMA protein (100 pM to 100 nM) prepared in MilliQ water were then deposited on the substrate. Finally, SERS tags were added to identify and localize the aptamer-PSMA protein binding. SERS-based quantification of the captured PSMA was then carried out, as reported in **Figure 4.2**, in which each data point was obtained by averaging three 5 μ m x 5 μ m maps that were collected at random on each protein substrate. It can be observed that the intensity of the Raman band of 4-ATP at 1438 cm^{-1} varies linearly with the concentration of PSMA added, with a linear correlation ($R^2 = 0.99838$) between the SERS intensity at 1438 cm^{-1} and the log of protein concentration, between the concentrations of 0.1 nM and 100 nM. Interestingly, additional peaks were observed when the soluble PSMA protein was deposited on the substrates, which, upon further analysis, were assigned to both PSMA aptamer and PSMA protein (**Figure 4.3**).

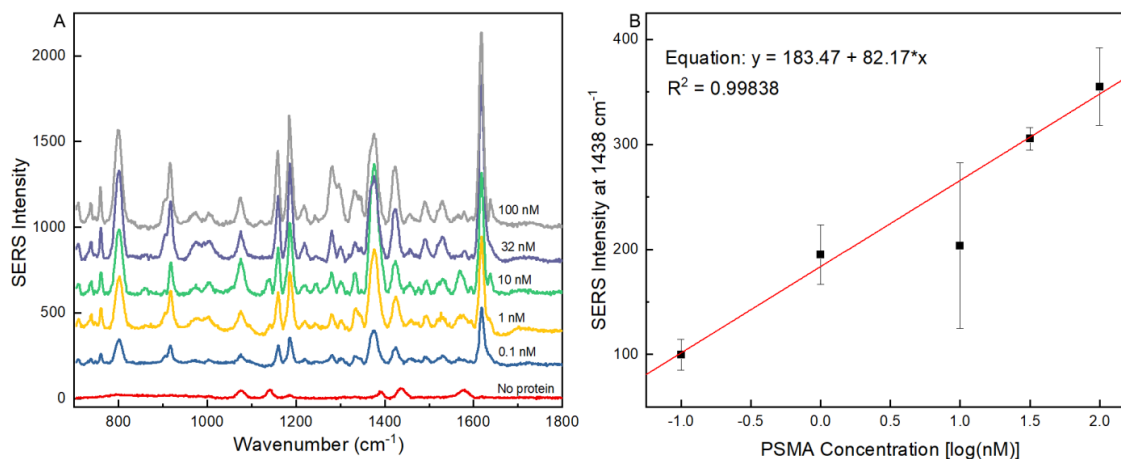


Figure 4.2 SERS signal dependence on concentration of soluble PSMA protein. Figure 4.2(A) shows the SERS peaks observed between 700 and 1800 cm⁻¹ for protein concentrations between 100 pM and 100 nM. A sample lacking the protein was used as a control. Figure 4.2(B) shows the intensity variation of the peak 1438 cm⁻¹ with respect to log of the PSMA protein concentration in nM.

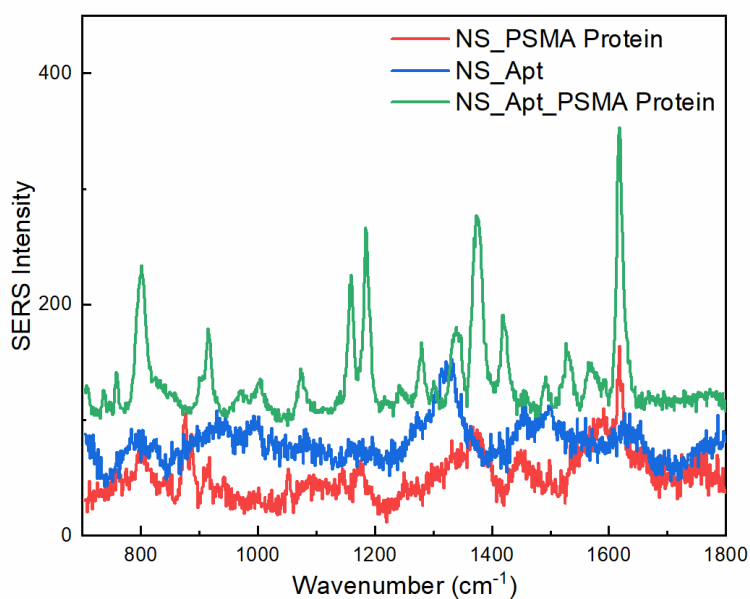


Figure 4.3 Figure shows SERS peaks that result from the addition of PSMA aptamer and soluble PSMA protein.

4.4.3 Expression of PSMA in Prostate Cancer Cells

Prior to SERS experiments on the prostate cancer cells LNCaP and PC3, the expression of PSMA in these cells was confirmed using RT-PCR and western blot analysis. For RT-

PCR, both cells were lysed and the RNA was extracted. A commercially available cDNA reverse transcription kit was then used to convert the RNA to cDNA. The resultant cDNA was employed for quantitative PCR analysis, which showed a high expression of PSMA in LNCaP cells and no expression in PC3 cells, as seen in **Figure 4.4A**. The results were further confirmed with western blot analysis. For this, the cells were lysed and their protein was extracted via SDS-PAGE. The protein extracts were then incubated with a primary PSMA antibody and the appropriate secondary antibody. Similar to what we observed with PCR, the results shown in **Figure 4.4B** revealed moderate to high expression of PSMA in LNCaP cells and no PSMA expression in PC3 cells. For both experiments, β -actin was used as a loading control.

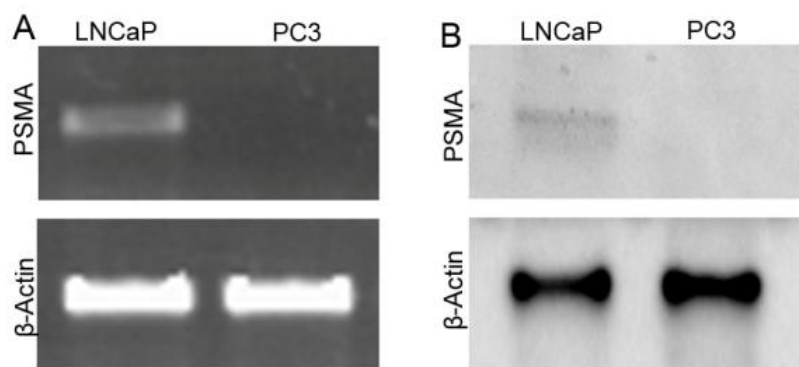


Figure 4.4 Figure shows the confirmation of the expression of PSMA in LNCaP cells. Figure 4.4(A) shows the RT-PCR results observed in the prostate cancer cells, LNCaP and PC3 while Figure 4.4(B) shows the Western Blot analysis of LNCaP and PC3 cells. Both experiments confirm the expression of PSMA in LNCaP cells while PC3 cells show no expression of PSMA. β -actin was used as a loading control in both experiments.

In order to test the binding of the PSMA aptamer with LNCaP cells, a thiolated PSMA aptamer conjugated with a fluorophore, Alexa Fluor 488 was used. Both LNCaP and PC3 cells were labeled with the aptamer and imaged. As a comparison, the cells were also

stained with a primary PSMA antibody conjugated to Alexa Fluor 488. Results seen in **Figure 4.5** show that both PSMA aptamer and antibody were able to bind to LNCaP cells, with the aptamer showing higher affinity for the LNCaP cells when compared to the antibody. As expected, no fluorescence was observed when PC3 cells were stained with either PSMA aptamer or PSMA antibody (**Figure 4.6**).

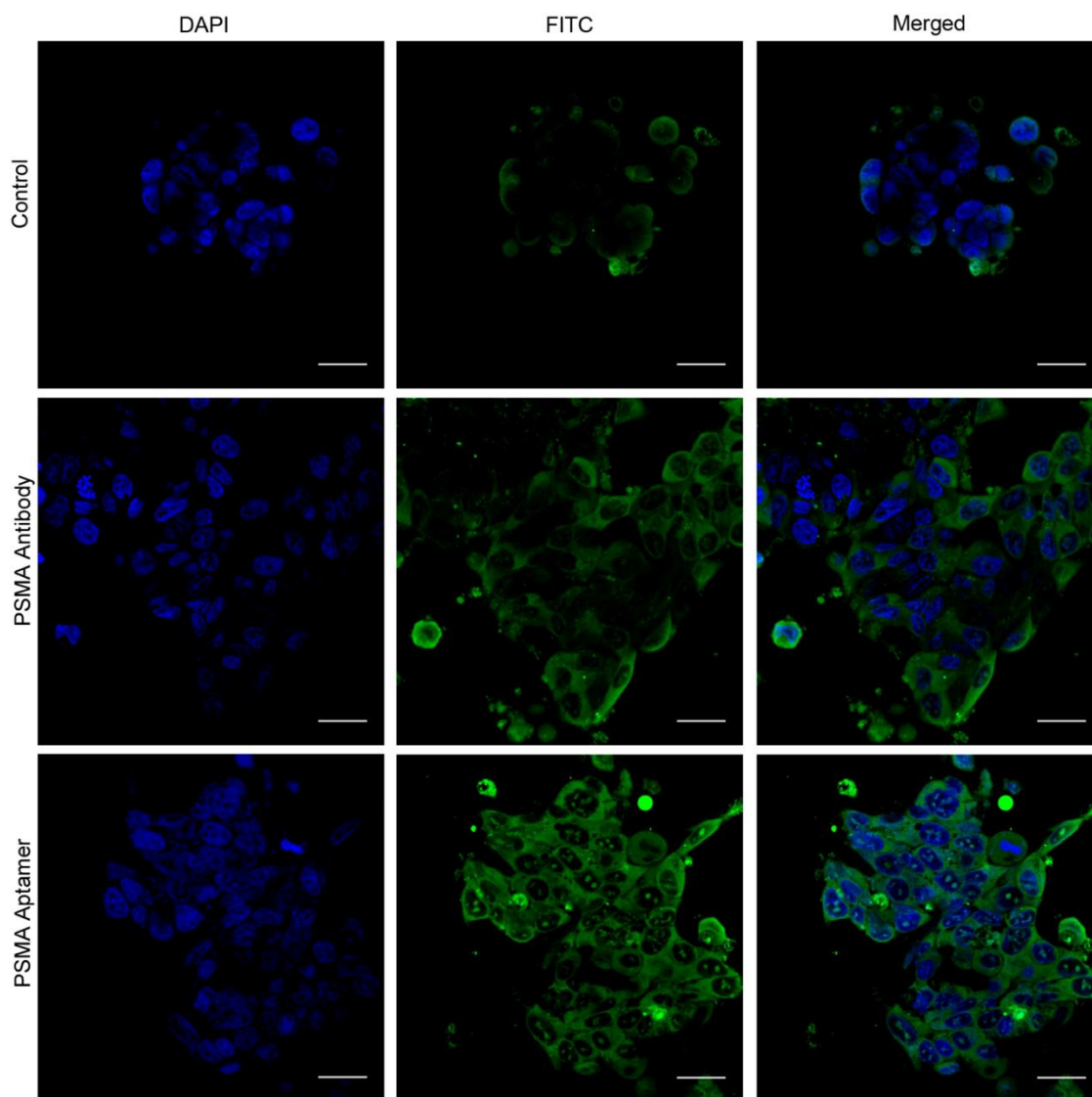


Figure 4.5 Fluorescent staining of LNCaP cells with PSMA antibody and PSMA aptamer that were conjugated to the fluorophore Alexa Fluor 488. Cell nuclei were stained with DAPI. Control represents cells that weren't stained with both PSMA aptamer and antibody. Scale bars represent 30 μm .

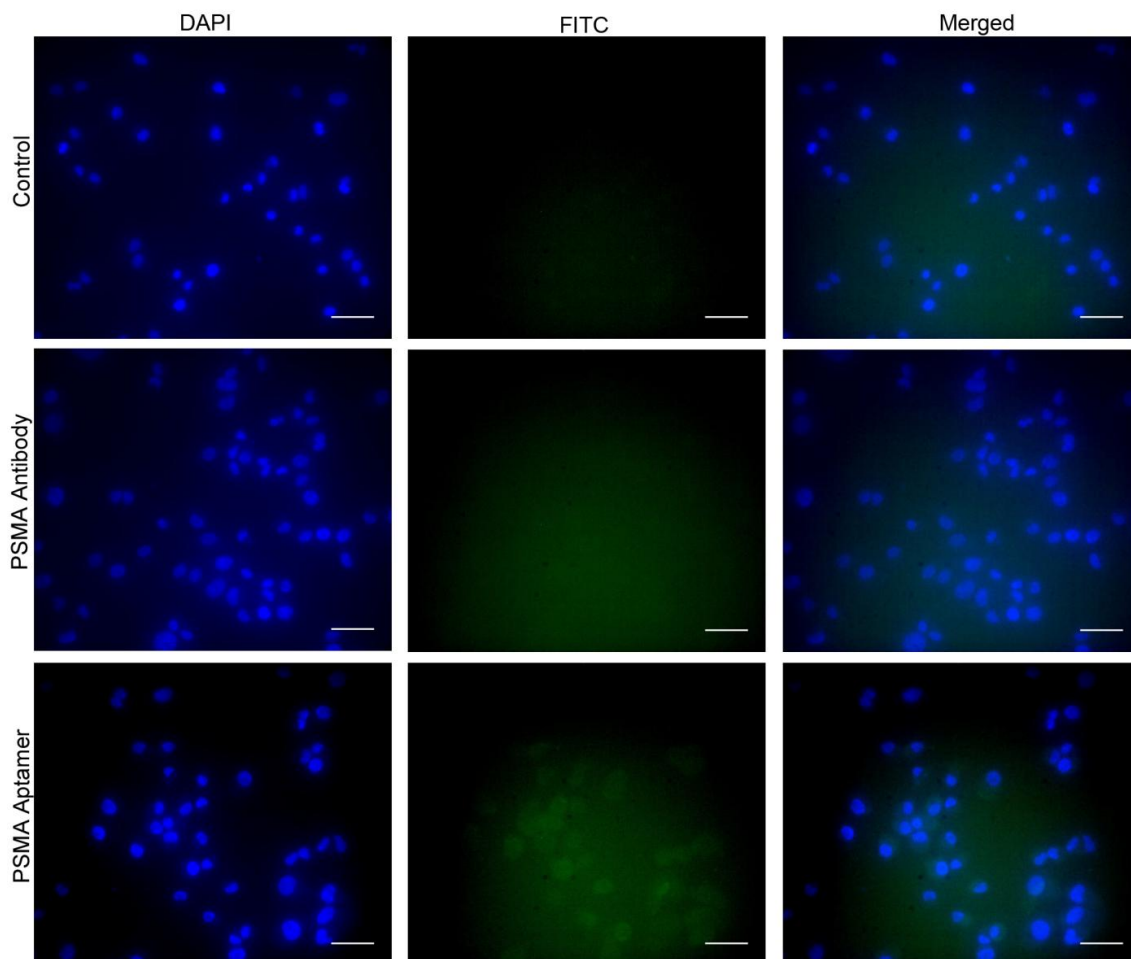


Figure 4.6 Figure shows the fluorescent staining of PC3 cells with PSMA antibody and PSMA aptamer that were conjugated to the fluorophore, Alexa Fluor 488. Cell nuclei were stained with DAPI. Control represents cells that weren't stained with both PSMA aptamer and antibody. Scale bars represent 50 μm .

A cell viability assessment was then carried out to determine the safest concentration of tags that could be loaded in the cell culture while providing a sufficiently intense SERS response. LNCaP cells were incubated with a range of nanoparticle concentrations from 1 nM to 5 nM for 24 hours. The cell viability was then assessed via an MTT proliferation assay. The results were normalized with respect to the untreated control. **Figure 4.7** reveals that the cells remained viable and comparable to the control at all concentrations

of nanoparticles. Since no statistical differences were observed between the groups, SERS tags at a concentration of 3 nM were used for PSMA quantification.

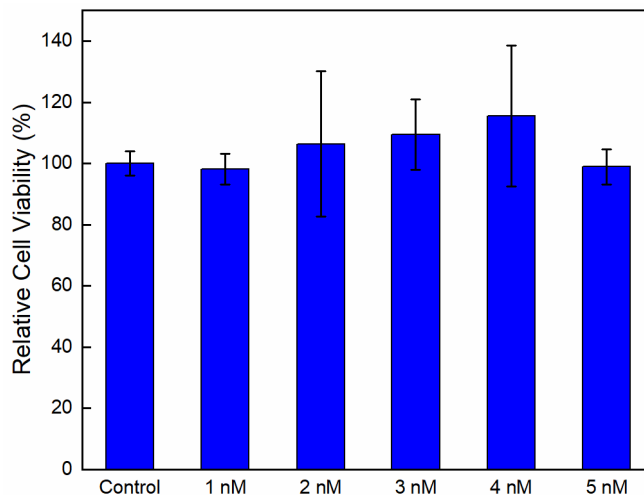


Figure 4.7 Cell viability results via MTT proliferation assay show the relative cell viability observed in LNCaP cells after exposure to different concentrations of gold nanostars functionalized with 4-ATP and PSMA aptamer for 24 hours. Viability results have been normalized to the control (without nanoparticles). Error bars represent standard deviation with $n = 3$.

4.4.4 SERS Analysis of Cells

PSMA expression in LNCaP and PC3 cells was measured at the single cell level using SERS. Both prostate cancer cells were counted and plated in a tissue culture plate and allowed to attach overnight. They were then incubated with a 3 nM concentration of SERS tags, i.e. gold nanostars functionalized with the Raman reporter, 4-ATP, and PSMA aptamer. The cells were washed thoroughly and fixed before SERS measurements. Three maps of $5 \mu\text{m} \times 5 \mu\text{m}$ sized area were acquired for each cell and averaged. **Figure 4.8(A)** shows the SERS spectra obtained from LNCaP cells incubated with the SERS tags. Data acquired from 5 individual cells showed slight variation in SERS intensity, which could be due to expected differences in marker expression within

the same cell population or to differences nanoparticle uptake. The average SERS spectra from LNCaP cells seen in **Figure 4.8(B)** were considered to be representative of the entire cell population, with an expected range of variability as that observed among the various cells. On the other hand, PC3 cells, known to not overexpress PSMA were found to possess Raman peaks with very low intensity.

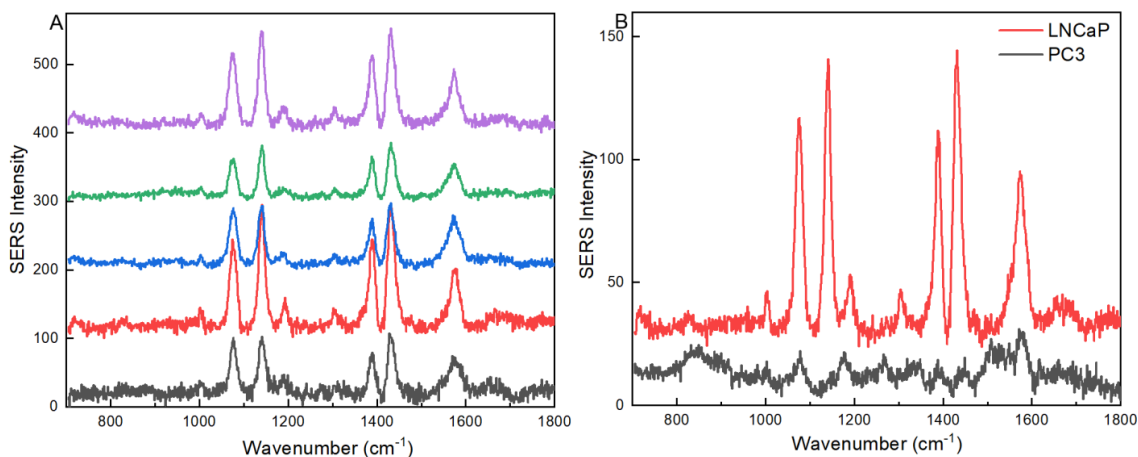


Figure 4.8 SERS spectra seen in LNCaP cells incubated with nanostars functionalized with 4-ATP and PSMA aptamer. Figure 4.6(A) shows the variation in SERS intensity seen at the single cell level in five different LNCaP cells. Further assessment of assay selectivity was carried out by incubating PC3 cells that have no surface expression of PSMA. Results from this are shown in Figure 4.6(B).

4.4.5 Analysis of PSMA expression in Prostate TMA

Prostate tissue microarrays containing biopsied specimens from patients with different clinical staging were analyzed by first grouping them according to the new grading system outlined by the International Society of Urological Pathology (ISUP) in 2014.¹⁷ The tissue samples were divided into Grade Groups 1-5: Grade Group I (Gleason score 6), Grade Group II (Gleason score 3+4=7), Grade Group III (Gleason score 4+3=7), Grade Group IV (Gleason score 3+5=8; 5+3=8) and Grade Group V (Gleason score

4+5=9; 5+4=9). No samples with Gleason score 10 were present in the TMA. The tissues were then further classified in three groups based on the recommended therapy: 1) Watchful waiting (no therapy), 2) non-metastatic active therapy, and 3) metastasized and/or castration resistant therapy (including palliative care).

To compare SERS imaging against immunofluorescence staining for PSMA quantification in TMAs, the prostate TMA samples were first de-paraffinized and hydrated. For IF experiments, the tissue sections were stained with a primary PSMA antibody and an appropriate secondary antibody conjugated with TRITC. The cell nuclei were stained with DAPI and the TMA was imaged. Analysis from IF seen in **Figure 4.9** showed an increase in the fluorescence intensity between Group 1 and Group 2, while no distinct difference in compounded PSMA expression was observed between Group 2 and Group 3.

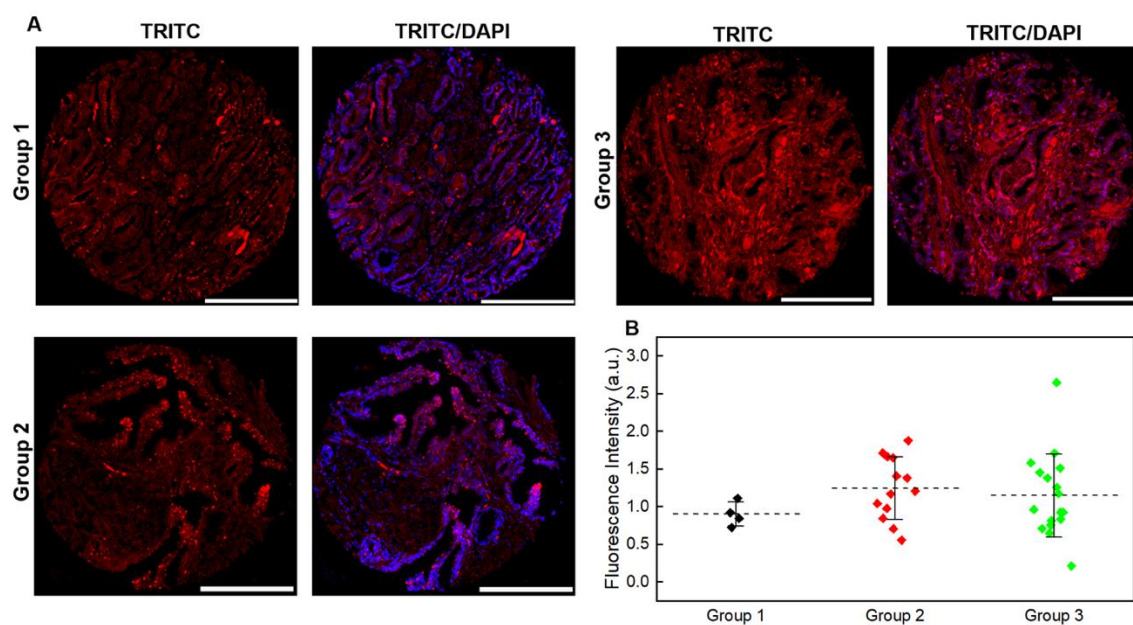


Figure 4.9 Representative immunofluorescence staining results of a prostate tissue microarray stained with a primary PSMA antibody and a secondary antibody conjugated

with TRITC. Cell nuclei have been stained with DAPI. Fluorescence intensity (background subtracted) obtained from immunofluorescence staining of the prostate TMA. The prostate tissue sections have a pathological status ranging from Grade Groups 1-5 and show increasing PSMA expression in going from Group 1 to Group 2, while no clear differentiation was possible between Group 2 and Group 3. Scale bars represent 200 μm .

For SERS experiments, after incubating each tissue section with SERS tags, an average of five maps were obtained over an area of 10 μm x 10 μm for each tissue section in the TMA. The averaged SERS signal intensities were then compounded Group 1, Group 2, and Group 3, as defined above, and reported in **Figure 4.10A**. Similar to what was observed in IF staining, the SERS intensity increased as the stage of prostate cancer increased. To better understand the differences in detection of PSMA with the two methods, the fluorescence intensity from the IF staining was quantified over the entire area of the tissue and subtracted from the background. The intensity was then averaged with samples in the TMA within the same therapy Group. Similarly, for SERS measurements, the intensity of the 1438 cm^{-1} peak was averaged for all samples according to the same classification strategy. A side by side comparison between the intensities revealed a similar pattern, in which substantial increase in PSMA expression levels occurs between the lowest (Group 1) and the highest (Group 3) groups. However, the analysis of the intermediate Group 2 and how it correlates to Group 1 and Group 3 provides further insight. Two important differences can be gathered from the SERS results: a) The SERS-based quantification of PSMA allows to differentiate Group 1 from Group 2 based on the larger spread of the data points in Group 2, consistent with the increased tissue heterogeneity that is typical of high Gleason score cancerous tissues; b) A clear differentiation in average PSMA expression levels, in addition to further spread data points, describes Group 3, in line with tissues with more advanced and/or metastatic

character. The clear differentiation in expression levels between Groups 1 and 2 and Group 3 can be also appreciated looking directly at the SERS data in **Figure 4.10B**.

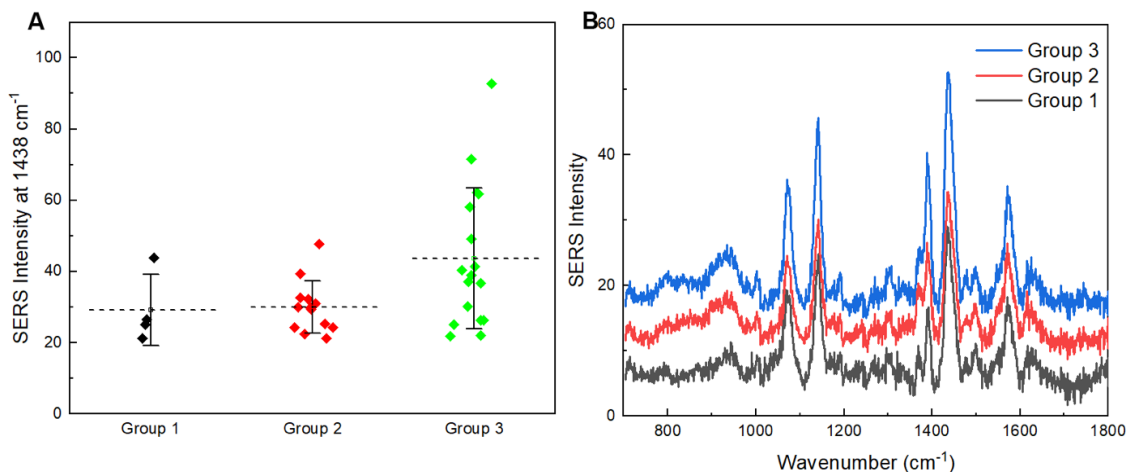


Figure 4.10 SERS spectra of the prostate tissue microarrays that were incubated with SERS tags. a) SERS intensity of the 1438 cm^{-1} peak of the spectra obtained from the prostate TMA at different disease stages compounded in groups 1, 2, and 3 depending on recommended therapy. SERS data points become substantially more spread with increasing disease severity, consistent with tissue heterogeneity. B) Averaged SERS spectra for the three groups show clear increase in the intensity of the 1438 cm^{-1} peak between groups 2 and 3, consistent with higher PSMA expression in advanced stage disease.

4.5 Conclusion

In conclusion, we further demonstrated the validity of PSMA as effective biomarker for stratification of prostate cancer patients, with improved discretization and tissue heterogeneity assessment than possible with fluorescence-based immunohistochemistry. The opportunity of quantifying biomarker expression in tissue microarrays and employing the obtained values as undisputable metrics for therapeutic management promises to aid in the difficult process of staging a patient and providing personalized treatment. By leveraging the field enhancing properties of gold nanostars along with the improved targeting properties of the PSMA aptamer and the sensitivity of SERS, we were

able to quantify PSMA expression both at the single cell level and tissue microarrays. Albeit not included in clinical trials, and only representing a retrospective study of a limited number of prostate cancer patients, our results promise to bring SERS at the forefront among the clinically-relevant techniques enabling detailed quantification of biomarker expression. Further implementation of this approach will enable the assessment of other prostate cancer biomarkers and hallmark biomarkers for additional cancer types.

4.6 References

1. <https://www.cancer.org/cancer/prostate-cancer/about/key-statistics.html>.
2. <https://www.cancer.net/cancer-types/prostate-cancer/stages-and-grades>.
3. Shah, R. B.; Zhou, M., Recent advances in prostate cancer pathology: Gleason grading and beyond. *Pathol Int* 2016, 66 (5), 260-72.
4. Bravaccini, S.; Puccetti, M.; Bocchini, M.; Ravaioli, S.; Celli, M.; Scarpi, E.; De Giorgi, U.; Tumedei, M. M.; Rauli, G.; Cardinale, L.; Paganelli, G., PSMA expression: a potential ally for the pathologist in prostate cancer diagnosis. *Sci Rep* 2018, 8 (1), 4254.
5. Ross, J. S.; Sheehan, C. E.; Fisher, H. A.; Kaufman, R. P., Jr.; Kaur, P.; Gray, K.; Webb, I.; Gray, G. S.; Mosher, R.; Kallakury, B. V., Correlation of primary tumor prostate-specific membrane antigen expression with disease recurrence in prostate cancer. *Clin Cancer Res* 2003, 9 (17), 6357-62.
6. Santoni, M.; Scarpelli, M.; Mazzucchelli, R.; Lopez-Beltran, A.; Cheng, L.; Cascinu, S.; Montironi, R., Targeting prostate-specific membrane antigen for personalized therapies in prostate cancer: morphologic and molecular backgrounds and future promises. *J Biol Regul Homeost Agents* 2014, 28 (4), 555-63.
7. Minner, S.; Wittmer, C.; Graefen, M.; Salomon, G.; Steuber, T.; Haese, A.; Huland, H.; Bokemeyer, C.; Yekebas, E.; Dierlamm, J.; Balabanov, S.; Kilic, E.; Wilczak, W.; Simon, R.; Sauter, G.; Schlomm, T., High level PSMA expression is associated with early PSA recurrence in surgically treated prostate cancer. *Prostate* 2011, 71 (3), 281-8.
8. Wang, Y.; Yan, B.; Chen, L., SERS Tags: Novel Optical Nanoprobes for Bioanalysis. *Chemical Reviews* 2013, 113 (3), 1391-1428.
9. Rodríguez-Lorenzo, L.; Álvarez-Puebla, R. A.; de Abajo, F. J. G.; Liz-Marzán, L. M., Surface Enhanced Raman Scattering Using Star-Shaped Gold Colloidal Nanoparticles. *The Journal of Physical Chemistry C* 2010, 114 (16), 7336-7340.
10. Dassie, J. P.; Liu, X. Y.; Thomas, G. S.; Whitaker, R. M.; Thiel, K. W.; Stockdale, K. R.; Meyerholz, D. K.; McCaffrey, A. P.; McNamara, J. O., 2nd; Giangrande, P. H., Systemic administration of optimized aptamer-siRNA chimeras promotes regression of PSMA-expressing tumors. *Nat Biotechnol* 2009, 27 (9), 839-49.
11. Yuan, H.; Khoury, C. G.; Hwang, H.; Wilson, C. M.; Grant, G. A.; Vo-Dinh, T., Gold nanostars: surfactant-free synthesis, 3D modelling, and two-photon photoluminescence imaging. *Nanotechnology* 2012, 23 (7), 075102.
12. Maier, S. A., *Plasmonics: fundamentals and applications*. Springer Science & Business Media: 2007.
13. Hu, X.; Wang, T.; Wang, L.; Dong, S., Surface-Enhanced Raman Scattering of 4-Aminothiophenol Self-Assembled Monolayers in Sandwich Structure with Nanoparticle Shape Dependence: Off-Surface Plasmon Resonance Condition. *The Journal of Physical Chemistry C* 2007, 111 (19), 6962-6969.
14. Quynh, L. M.; Nam, N. H.; Kong, K.; Nhung, N. T.; Notingher, I.; Henini, M.; Luong, N. H., Surface-Enhanced Raman Spectroscopy Study of 4-ATPon Gold Nanoparticles for Basal Cell Carcinoma Fingerprint Detection. *Journal of Electronic Materials* 2016, 45 (5), 2563-2568.
15. Osawa, M.; Matsuda, N.; Yoshii, K.; Uchida, I., Charge transfer resonance Raman process in surface-enhanced Raman scattering from p-aminothiophenol adsorbed on

silver: Herzberg-Teller contribution. *The Journal of Physical Chemistry* 1994, 98 (48), 12702-12707.

16. Steel, A. B.; Levicky, R. L.; Herne, T. M.; Tarlov, M. J., Immobilization of nucleic acids at solid surfaces: effect of oligonucleotide length on layer assembly. *Biophysical journal* 2000, 79 (2), 975-81.

17. Epstein, J. I.; Egevad, L.; Amin, M. B.; Delahunt, B.; Srigley, J. R.; Humphrey, P. A.; Grading, C., The 2014 International Society of Urological Pathology (ISUP) Consensus Conference on Gleason Grading of Prostatic Carcinoma: Definition of Grading Patterns and Proposal for a New Grading System. *Am J Surg Pathol* 2016, 40 (2), 244-52.

CHAPTER 5 CONCLUSION AND FUTURE DIRECTION

5.1 Conclusion

The work in this dissertation focused on the development of a sensitive SERS based sensing platform that would allow detection and quantification of cancer biomarkers. SERS tags consisting of gold nanostars functionalized with aptamers were used to detect and quantify the cancer biomarker EpCAM at the single cell level in cancer cells with different phenotype expressions. Furthermore, the SERS tags were able to discriminate between early and late stage prostate cancer based on the expression of a prostate-specific PSMA biomarker. This work was the first to explore SERS tags for cancer staging in tissue microarray samples. These findings have major health implications as they would be beneficial in monitoring phenotype evolutions in cancer cells, tissues, or bodily fluids thus enabling us to follow in real time disease onset and progression. In addition to these demonstrations, we also carried out a systematic study in which the size, shape, and surface chemistry of gold nanoparticles were taken into account to provide a multiparametric evaluation of their toxicity. Knowledge of the underlying toxicity mechanisms with gold nanoparticles can be applied to design more effective strategies to safely employ them in the medical field.

5.2 Future Directions

Chapter 2 looked in detail at the toxicity induced by gold nanoparticles of different morphologies and surface chemistries *in vitro*. While this study provided a basic understanding of toxicity mechanisms and NP uptake at the cellular level, it may not

accurately predict the toxicity response in an *in vivo* setting. In addition, we also observed the nanoparticles caused damage to cellular organelles like mitochondria because of the generation of free radicals and oxidative stress. This could cause mutagenesis and up- and down-regulation of genes and proteins. Studies have shown that prolonged exposure of cells to nanoparticles can lead to changes in their gene expression.¹ Future work could look at the effects of nanoparticle exposure on gene regulation. In addition, we need to carry out long term investigations of the effects of nanoparticle exposure *in vivo*. The biodistribution and pharmacokinetics of the gold nanoparticles in the body needs to be properly understood.

In chapter 3, we developed a SERS-based substrate for the recognition and quantification of EpCAM, which is an epithelial biomarker overexpressed in several tumors.²⁻³ Changes in the expression of EpCAM have been associated with the onset of metastasis.⁴ However, studies have shown that tumor cells undergo epithelial to mesenchymal transition (EMT) in order to separate from the parent tumor and different subsets of cells heterogeneously evolve their phenotypes at various stages of cancer progression.⁵ Future work could therefore focus on identifying key epithelial and mesenchymal biomarkers involved in cancer progression and simultaneously detect them on cells. It could also explore using the developed substrates to isolate tumor cells and other macromolecules from bodily fluids such as blood. Finally, portable Raman spectrometers could be employed for molecular detection on these substrates, thus rendering it a true point-of-care diagnostic.

Chapter 4 explored the use of SERS tags to distinguish between different stages of prostate cancer in a prostate tissue microarray based on the expression of PSMA on these tissues. While we observed an up-regulation of PSMA expression in aggressive forms of the tumor, there is a need to identify other predictive biomarkers that can more finely distinguish between different tumor stages. Future work could explore the role of biomarkers such as androgen receptor splice variant 7 (AR-V7) protein. Studies have shown that measuring the expression of this biomarker can help detect patients with progressive metastatic castration resistant prostate cancer that are unresponsive to antiandrogen therapy.⁶

Overall our work provides a framework for developing a molecular imaging platform that could be implemented in the future for monitoring cancer progression with high sensitivity and selectivity.

5.3 References

1. Falagan-Lotsch, P.; Grzincic, E. M.; Murphy, C. J., One low-dose exposure of gold nanoparticles induces long-term changes in human cells. *Proc Natl Acad Sci U S A* **2016**, *113* (47), 13318-13323.
2. Went, P.; Vasei, M.; Bubendorf, L.; Terracciano, L.; Tornillo, L.; Riede, U.; Kononen, J.; Simon, R.; Sauter, G.; Baeuerle, P. A., Frequent high-level expression of the immunotherapeutic target Ep-CAM in colon, stomach, prostate and lung cancers. *Br J Cancer* **2006**, *94* (1), 128-35.
3. Spizzo, G.; Went, P.; Dirnhofner, S.; Obrist, P.; Moch, H.; Baeuerle, P. A.; Mueller-Holzner, E.; Marth, C.; Gastl, G.; Zeimet, A. G., Overexpression of epithelial cell adhesion molecule (Ep-CAM) is an independent prognostic marker for reduced survival of patients with epithelial ovarian cancer. *Gynecol Oncol* **2006**, *103* (2), 483-8.
4. Gorges, T. M.; Tinhofner, I.; Drosch, M.; Röse, L.; Zollner, T. M.; Krahn, T.; von Ahsen, O., Circulating tumour cells escape from EpCAM-based detection due to epithelial-to-mesenchymal transition. *BMC Cancer* **2012**, *12* (1), 178.
5. Alix-Panabieres, C.; Pantel, K., Challenges in circulating tumour cell research. *Nat Rev Cancer* **2014**, *14* (9), 623-631.
6. Scher, H. I.; Lu, D.; Schreiber, N. A.; et al., Association of ar-v7 on circulating tumor cells as a treatment-specific biomarker with outcomes and survival in castration-resistant prostate cancer. *JAMA Oncology* **2016**, *2* (11), 1441-1449.